

2024-08-01

Development of 3D human cardiovascular and cancer tissue model within a self-driven microfluidic platform for preclinical drug screening

Aibhlin Alexis Esparza
University of Texas at El Paso

Follow this and additional works at: https://scholarworks.utep.edu/open_etd



Part of the [Biomedical Commons](#)

Recommended Citation

Esparza, Aibhlin Alexis, "Development of 3D human cardiovascular and cancer tissue model within a self-driven microfluidic platform for preclinical drug screening" (2024). *Open Access Theses & Dissertations*. 4176.

https://scholarworks.utep.edu/open_etd/4176

This is brought to you for free and open access by ScholarWorks@UTEP. It has been accepted for inclusion in Open Access Theses & Dissertations by an authorized administrator of ScholarWorks@UTEP. For more information, please contact lweber@utep.edu.

DEVELOPMENT OF 3D HUMAN CARDIOVASCULAR AND CANCER TISSUE MODEL
WITHIN A SELF-DRIVEN MICROFLUIDIC PLATFORM FOR PRECLINICAL DRUG
SCREENING

AIBHLIN ALEXIS ESPARZA

Doctoral Program in Biomedical Engineering

APPROVED:

Sylvia Natividad-Diaz, Ph.D., Chair

Binata Joddar, Ph.D.

Wilson Poon, Ph.D.

Taslim Al-Hilal, Ph.D.

Stephen L. Crites, Jr., Ph.D.
Dean of the Graduate School

Copyright 2024 Aibhlin A. Esparza

Dedication

This is dedicated to my parents, Celia Lopez and David Esparza, for their love and support for
my whole life.

To my sister, Aaliyah Esparza, reach for the stars and don't be afraid to fail every now and then.

To my brother, Brandon Esparza, for being my inspiration for everything I do.

This is for all of you.

In Memory of Brandon David Esparza, 2001 - 2023

DEVELOPMENT OF 3D HUMAN CARDIOVASCULAR AND CANCER TISSUE MODEL
WITHIN A SELF-DRIVEN MICROFLUIDIC PLATFORM FOR PRECLINICAL DRUG
SCREENING

by

AIBHLIN ALEXIS ESPARZA, B.S. Mechanical Engineering

DISSERTATION

Presented to the Faculty of the Graduate School of

The University of Texas at El Paso

in Partial Fulfillment

of the Requirements

for the Degree of

DOCTOR OF PHILOSOPHY

DEPARTMENT OF METALLURGICAL, MATERIALS, AND BIOMEDICAL
ENGINEERING

THE UNIVERSITY OF TEXAS AT EL PASO

August, 2024

Acknowledgements

First and foremost, I would like to thank my family for their endless support, love, and dedication to my development, well-being, and my education. All my accomplishments are not only mine, but ours. To my parents, Celia Lopez and David Esparza, there are no words to describe how much you've inspired me in all aspects of life. You've shown me that there is always beauty in the struggle. To my sister, Aaliyah Esparza, thank you for motivating me to finish school and always being there for me. To my brother, Brandon Esparza, you were and continue to be my inspiration for everything I do.

Next, I would like to thank my mentor, dissertation advisor, and committee chair, Dr. Sylvia Natividad-Diaz. You have been a role model to me throughout my time in the BME program, inside and outside of the lab. Thank you for always offering support, guidance, advice, and opportunities for me to grow as an individual, a woman in STEM, and as a researcher. Thank you to my committee members, Dr. Binata Joddar, Dr. Wilson Poon, and Dr. Taslim Al-Hilal.

I would like to thank the members of Dr. Natividad-Diaz's lab, the 3D Printed Microphysiological Systems Laboratory, who had the pleasure of working with: Brittany Stark Ph.D., Michelle Gamboa, Jose Perez, Nicole (Nicky) Jimenez, Paula Delgado, Pedro Hernandez, Luisa Carlon, Janine Hagar-Montoya, Naomi Velasquez, and Edgar Borrego Ph.D. Thank you for always listening to me, checking in on me, and helping me regardless of the question or project. You've all made our lab feel like a second home and family. Thank you to especially Nicky, Paula, and Jose who helped me run experiments, gather data, and analyze data for different experiments. Thank you to our lab post-doctoral researcher, Edgar, for training me on stem cell culture, differentiation, and many other technical skills; without your help, I would not have been able to finish this project.

Thank you to Dr. Joddar for allowing me to use her lab space and resources to complete several projects. Thank you for always offering guidance and opportunities for me to continue growing. Thank you to the members of the Inspired Materials & Stem Cell Based Tissue Engineering Laboratory (IMSTEL) including but not limited to Naveen Nagiah Ph.D., Carla Loyola, Raven El-Khoury Ph.D., Andie Padilla and Ivana Hernandez.

Thank you to Dr. Poon for always sharing your resources or knowledge on the different projects we've worked on. Thank you to Mario Corral Mata who worked on the microgravity and radiation NASA project with me.

Thank you to the individuals at the Border Biomedical Research Center (BBRC) and Cell Core. Thank you to Dr. Valera, Dr. Aguilera, and Gladys Almodovar for allowing me to use equipment and space for the culture and differentiation of hiPSC-CMs.

Thank you to Dr. Roberts and his student Peter Sanchez for training me on the Nanoscribe 3D printer and allowing me to use their resources for this project. Thank you to Dr. Boland, the BME program director, for always keeping me on track for coursework. Thank you to Dr. Quinones, the department chair for the Metallurgical, Materials, and Biomedical Engineering (MMBME) program.

Last, but not least, thank you to all the funding sources. Gates Millennium Scholarship and Stars Scholarship for funding my tuition and coursework. Thank you to the multiple funding sources for my graduate research assistantships including NIH SCORE SC2 1SC2GM144164-01 (SND), The University of Texas System Rising STARS E210291476 grant (SND), CPRIT-TREC RP210153 (SND), and NASA 2023 MUREP Partnership Learning Annual Notification (MPLAN).

Abstract

According to the American Heart Association and World Health Organization, cardiovascular diseases (CVDs) are the leading cause of death worldwide. Monolayer cell culture (2D) and animal models are conventional methods to study CVDs, however, they limit researcher's ability to simulate the human cardiovascular cellular microenvironments and accurate predication of pharmaceutical drug responses. Human induced pluripotent stem cell derived cardiomyocytes (hiPSC-CMs), biomaterials, and microfluidic technologies can be combined to create a controlled, reproducible 3D platform to study physiologically-relevant cellular responses to biochemical and physical changes in the microenvironment. My dissertation work demonstrates the development of novel self-driven microfluidic devices designed with capillary action fluid flow principles that can be fabricated with 3D Stereolithography (SLA) printing and polymer casting methods. The integration of 3D cardiovascular tissue models within these microfluidic devices allowed for the evaluation of cell organization, function, and responses to biochemical and physical changes within the system. This work is significant because the 3D cardiovascular tissue models demonstrated differences in cellular morphology and structural reorganization in devices with or without microposts up to 5 days in culture relative to standard culture methods. Multiple cell types were cultured in 3D within the microfluidic devices, including human umbilical vein endothelial cells (HUVECs), human AC16 cardiomyocytes, hiPSC-CMs, SKBR3 breast cancer cells, and patient derived xenograft (PDX) breast cancer cells, demonstrating the versatility of the microfluidic devices. Furthermore, the microfluidic device was integrated into two specific technology applications (TA), including a cardiovascular-breast cancer tissue model (TA-1) and cardiovascular model in simulated microgravity (TA-2). The TA-1 results indicate hiPSC-CMs are susceptible to reduced viability when treated with Herceptin, a HER2+ breast cancer chemotherapy drug. The TA-2 results demonstrated hiPSC-CMs cultured in microgravity maintained their phenotype relative to control studies in standard culture conditions. This work provides significant advancements in the design, fabrication, and study of capillary-driven microfluidic devices and their use as a platform for CVD research in multiple areas of biotechnology research.

Table of Contents

| | |
|---|-------|
| Dedication | iii |
| Acknowledgements | v |
| Abstract | vii |
| List of Tables | xiii |
| List of Figures | xiv |
| List of Diagrams | xvii |
| List of Abbreviations | xviii |
| Chapter 1 | 1 |
| Introduction | 1 |
| 1.1 Background | 1 |
| 1.2 Project Goal, Hypothesis, and Innovation | 7 |
| 1.3 Specific Aims | 7 |
| 1.3.1: Specific Aim 1 | 7 |
| 1.3.2: Specific Aim 2 | 8 |
| 1.3.3: Specific Aim 3 | 8 |
| 1.4 Dissertation Outline | 8 |
| Chapter 2 | 10 |
| Literature Review | 10 |
| Chapter 3 | 17 |
| Aim 1 - Design and fabricate a closed self-driven microfluidic device for 3D tissue culture | 17 |
| 3.1 Aim Overview | 17 |
| 3.2 Abstract | 17 |
| 3.3 Introduction | 18 |
| 3.4 Materials and Methods | 20 |
| 3.4.1 Capillary driven-flow microfluidic device design | 20 |
| 3.4.2 Three-dimensional (3D) printing techniques | 21 |
| I. 3D (SLA) Stereolithography printing | 21 |
| II. 3D printing with Nanoscribe Quantum X Printer | 22 |

| | |
|---|----|
| 3.4.3 Contact angle tests | 23 |
| 3.4.4 Fluid flow finite element analysis (FEA)..... | 24 |
| 3.4.5 Device fabrication optimization..... | 25 |
| I. PDMS mold fabrication..... | 26 |
| II. Ostemer322 polymer casting..... | 26 |
| 3.4.6 Fluid flow validation experiments | 28 |
| I. Dynabead fluid flow studies..... | 29 |
| II. Fluorescence microspheres fluid flow studies | 29 |
| III. Additional fluid flow experiments | 30 |
| 3.4.7 Statistical Analysis..... | 30 |
| 3.5 Results..... | 30 |
| 3.5.1 Contact angle | 30 |
| 3.5.2 Fluid flow Finite Element Analysis (FEA)..... | 32 |
| 3.5.3 Optimization of Formlabs 3D Printing | 35 |
| I. Micropost size and spacing..... | 37 |
| II. Visibility of 3D printed devices | 38 |
| III. Material change to Ostemer322..... | 41 |
| IV. Improvement of mold creation and utilization for polymer casting of Ostemer322 | 42 |
| 3.5.4 Nanoscribe device fabrication..... | 45 |
| I. Mold creation and polymer casting of Ostemer322 for Nanoscribe devices .. | 47 |
| 3.5.5 Capillary fluid flow validation experiments | 50 |
| I. Fluid flow experiments for 3D printed devices and Ostemer devices..... | 50 |
| II. Additional fluid flow studies..... | 54 |
| 3.6 Discussion and Conclusions | 57 |
| Chapter 4..... | 58 |
| Aim 2 – Optimization and development of 3D cardiovascular and cancer tissue models within the microfluidic device to study cell organization and function..... | 58 |
| 4.1 Aim Overview..... | 58 |
| 4.2 Abstract | 58 |
| 4.3 Introduction..... | 59 |
| 4.4 Materials and Methods..... | 61 |
| 4.4.1 Device fabrication..... | 61 |

| | |
|--|----|
| I. 3D SLA printing of microfluidic devices | 61 |
| II. Polymer casting with Ostemer322 | 62 |
| 4.4.2 3D cardiovascular tissue model development..... | 62 |
| I. HUVEC culture and dissociation | 62 |
| II. AC16 culture and dissociation | 62 |
| III. Gelatin-alginate hydrogel formation and loading into 3D printed microfluidic devices..... | 63 |
| IV. Fibrin hydrogel formation loading into microfluidic device and Transwell inserts | 63 |
| 4.4.3 Doxorubicin studies with 3D coculture of HUVECs and AC16 cells within capillary circuit microfluidic device | 65 |
| 4.4.4 3D cancer tissue model development | 66 |
| I. PDX culture and dissociation | 66 |
| II. SKBR3 culture and dissociation | 66 |
| III. Collagen hydrogel formation and loading into Nanoscribe devices | 66 |
| 4.4.5 Characterization with fluorescence microscopy | 67 |
| 4.4.6 Computational image analysis | 68 |
| I. Computational fluorescence image analysis – cell orientation | 68 |
| II. Computational fluorescence image analysis – network formation | 69 |
| 4.4.7 Automated Image Analysis Python Script (AIAPS) Validation..... | 69 |
| 4.4.8 Statistical Analysis..... | 70 |
| 4.5 Results and Discussion | 70 |
| 4.5.1 Fluorescence microscopy of single chamber 3D printed devices..... | 70 |
| 4.5.2 Cardiovascular and Vascular Tissue Models within capillary-circuit microfluidic device | 72 |
| I. Fluorescence microscopy | 72 |
| II. Cell orientation..... | 75 |
| III. Average network length..... | 78 |
| 4.5.3 Doxorubicin studies with 3D coculture of HUVECs and AC16 cells within capillary circuit microfluidic device | 80 |
| I. Fluorescence microscopy | 80 |
| II. Network formation analysis | 81 |
| II. Doxorubicin studies with 3D coculture of HUVECs and AC16s | 81 |
| 4.5.4 3D cancer tissue model | 82 |

| | |
|--|-----|
| 4.5.5 AIAPS Script Validation..... | 83 |
| 4.6 Discussion and Conclusions | 85 |
| Chapter 5..... | 87 |
| Aim 3 – Study the effects of biochemical and physical changes in the cardiovascular and breast cancer microphysiological systems. | 87 |
| 5.1 Aim Overview..... | 87 |
| 5.2 Abstract..... | 87 |
| 5.3 Introduction..... | 88 |
| 5.4 Materials and Methods..... | 91 |
| 5.4.1 Human induced pluripotent stem cell (hiPSC) culture and maintenance | 91 |
| 5.4.2 hiPSC-cardiomyocyte (CM) differentiation protocol | 91 |
| 5.4.3 Flow cytometry (FC) analysis..... | 92 |
| 5.4.4 Immunofluorescence staining | 93 |
| 5.4.5 Image analysis using AIAPS | 94 |
| 5.4.6 Beat rate time lapse videos and calculation | 94 |
| 5.4.7 Technology Application 1 (TA-1) - 3D cardiovascular and breast cancer tissue model | 95 |
| I. hiPSC-CM culture and dissociation | 95 |
| II. SKBR3 cell culture and dissociation..... | 95 |
| III. Development of 3D cardiovascular and breast cancer tissue models | 95 |
| IV. Herceptin exposure studies | 96 |
| 5.4.8 Technology Application 2 (TA-2) - 3D cardiovascular tissue model for microgravity..... | 96 |
| I. Microgravity Finite Element Analysis (FEA) simulation | 97 |
| II. Bioreactor rotating vessel preparation..... | 98 |
| III. hiPSC-CM culture and dissociation..... | 99 |
| IV. Development of 3D cardiovascular tissue models in simulated microgravity..... | 99 |
| 5.4.9 Statistical Analysis..... | 100 |
| 5.5 Results and Discussion | 100 |
| 5.5.1 hiPSCs characterization | 100 |
| 5.5.2 hiPSC-CM differentiation and characterization..... | 100 |
| 5.5.3 Beat rate analysis | 102 |

| | |
|---|-----|
| 5.5.4 TA-1 3D cardiovascular and breast cancer tissue model..... | 103 |
| I. hiPSC-CM HER2 characterization..... | 103 |
| II. Herceptin studies..... | 104 |
| 5.5.5 TA-2 3D cardiovascular tissue model for simulated microgravity..... | 107 |
| I. Rotational fluid flow simulation..... | 107 |
| II. Control and simulated microgravity studies..... | 108 |
| 5.6 Discussion and Conclusions | 110 |
| Chapter 6..... | 112 |
| Conclusions and future directions..... | 112 |
| 6.1 Conclusions..... | 112 |
| 6.2 Future directions | 113 |
| References..... | 115 |
| Vita | 122 |

List of Tables

| | |
|--|-----|
| Table 3.1: Assigned inlet velocities for each device design for FEA fluid flow studies..... | 25 |
| Table 3.2: Volumes of Trypan Blue and PBS added to microfluidic devices for fluid flow studies. | 28 |
| Table 3.3: Comparison of contact angle values. | 32 |
| Table 3.4: Design parameters for each microfluidic device concept..... | 36 |
| Table 3.5: Fluid velocities of 3D printed and Ostemer devices..... | 50 |
| Table 4.1: Primary and secondary antibodies for immunostaining. | 67 |
| Table 5.1: List of fluorescent antibodies used for flow cytometry analysis. | 93 |
| Table 5.2: Primary and secondary antibodies for immunostaining. | 94 |
| Table 5.3: Flow cytometry replicates for cTnT+ expression..... | 101 |
| Table 5.4: Average displacement and hiPSC-CM beats per minute..... | 102 |
| Table 5.5: Average displacement and hiPSC-CM beats per minute..... | 110 |

List of Figures

| | |
|---|----|
| Figure 3.1: Contact angle experimental setup for Ostemer322. | 31 |
| Figure 3.2: Experimental setup for Nanoscribe contact angle test and contact angle analysis using ImageJ/Fiji. | 31 |
| Figure 3.3: Representative contact angle images for clear resin (Formlabs 3D printer), IP-Q resin (Nanoscribe 3D Printer), and Ostemer322..... | 32 |
| Figure 3.4: Microfluidic device design evolution. Multiple 3D models are presented from the early stages of this study into the final devices used for future experiments (outlined in red). ... | 33 |
| Figure 3.5: FEA analysis of devices 2-7..... | 34 |
| Figure 3.6: Post-processed 3D printed device to assess printing accuracy. a) shows the first microchannel, b) shows the microchannel leading into the chamber and some microposts, and c) shows microposts in the chamber. | 38 |
| Figure 3.7: Images acquired using a benchtop light microscope of various 3D printed devices. | 39 |
| Figure 3.8: Images acquired using fluorescence microscope (Leica Thunder Imager) of various 3D printed devices. | 40 |
| Figure 3.9: Two 3D printed devices printed within the same month with the same resin cartridge. | 41 |
| Figure 3.10: 3D printed molds for circuit device without posts (DWoP) and the resultant Ostemer device. | 42 |
| Figure 3.11: Outlines the process of 3D printing a device, creating a PDMS mold, and Ostemer322 casting to create final Ostemer device..... | 43 |
| Figure 3.12: Compares 3D printed devices and fabricated Ostemer322 devices under light and fluorescence microscopes. | 44 |
| Figure 3.13: Autofluorescence comparison between Ostemer devices fabricated on different days. | 45 |
| Figure 3.14: Nanoscribe device CAD model and stereomicroscope images of first Nanoscribe print. | 46 |
| Figure 3.15: Attempt to print multiple devices on one single wafer using Nanoscribe 3D printer. | 47 |
| Figure 3.16: Overall size dimension comparison between Ostemer devices with posts and the Nanoscribe device. | 48 |
| Figure 3.17: PDMS mold and Ostemer322 Nanoscribe device process. Scanning electron microscopy (SEM) images of 3D printed Nanoscribe device and Ostemer322 casted Nanoscribe device. | 49 |
| Figure 3.18: Time lapse picture of Trypan Blue and PBS through different device designs of 3D printed or Ostemer devices. | 51 |
| Figure 3.19: shows a time lapse of Trypan Blue and PBS through the device without posts (DWoP). | 52 |
| Figure 3.20: shows a time lapse of Trypan Blue and PBS through the device with posts (DWP). | 52 |
| Figure 3.21: shows a time lapse of Trypan Blue and PBS through the Nanoscribe device..... | 53 |
| Figure 3.22: Time lapse of Dynabeads flowing through a no posts Ostemer device. Original video captured using a stereomicroscope. | 54 |
| Figure 3.23: Time lapse of red fluorescent beads flowing through a device without posts Ostemer device. Original video captured using a 3D Leica fluorescence microscope. | 55 |

| | |
|---|----|
| Figure 3.24: Time lapse of red fluorescent beads flowing through a device with posts Osteomer device. Original video captured using a 3D Leica fluorescence microscope. | 55 |
| Figure 3.25: Time lapse of red fluorescent beads flowing through a Nanoscribe device. Original video captured using a 3D Leica fluorescence microscope. | 56 |
| Figure 3.26: Time lapse of mixing of colored fluids to demonstrate continuous movement of liquid. | 56 |
| Figure 4.1: referred orientation is measured with OrientationJ plugin in ImageJ. The orientation is measured from z-stack fluorescence images (a) with reference to the 0° on the right side of the image (as indicated in (b)) and measured counterclockwise. Following the orientation analysis, the orientation histogram is formed (c). | 68 |
| Figure 4.2: Schematic of 3D printed microfluidic devices with no microposts (a), grid formation microposts (b), and staggered formation microposts (c). | 70 |
| Figure 4.3: Fluorescence images acquired on day 5 from HUVEC and AC16 samples of 3D printed devices with no microposts (a-b), grid microposts (c-d), and staggered microposts (e-f). | 71 |
| Figure 4.4: Representative 3D z-stack fluorescence images for days 1, 3, and 5 for HUVEC samples in Transwell inserts, device without posts (DWoP), and device with posts (DWP). White arrows indicate capillary-like lumen formation in each microenvironment condition. | 73 |
| Figure 4.5: Representative 3D z-stack fluorescence images for days 1, 3, and 5 for AC16 samples in Transwell inserts, device without posts (DWoP), and device with posts (DWP). White arrows indicate capillary-like lumen formation in each microenvironment condition. | 74 |
| Figure 4.6: Cell percentage alignment at 0° and 90° distribution from VTM (HUVEC) and CTM (AC16) samples on day 1, 3, and 5 in Transwell, DWoP, and DWPG. (n = 5) *p < 0.05, **p < 0.002, ***p < 0.0002, ****p < 0.0001. | 75 |
| Figure 4.7: Representative cell orientation distribution graphs (OrientationJ ImageJ plugin) from VTM and CTM samples on day 1, 3, and 5 in Transwell inserts. (n=5) | 76 |
| Figure 4.8: Representative cell orientation distribution graphs (OrientationJ ImageJ plugin) from VTM and CTM samples on day 1, 3, and 5 in DWoP. (n=5) | 77 |
| Figure 4.9: Representative cell orientation distribution graphs (OrientationJ ImageJ plugin) from VTM and CTM samples on day 1, 3, and 5 in DWP. (n=5) | 78 |
| Figure 4.10: Quantification of cellular network formation within VTM (HUVECs) and CTM (AC16). Analysis of total network length in fluorescence images. (a) shows day 1, 3, and 5 data with HUVECs and (b) shows day 1, 3, and 5 data with AC16s. (n = 5) *p < 0.05, **p < 0.001. | 79 |
| Figure 4.11: Coculture of HUVECs and AC16s within capillary-circuit microfluidic device. Images acquired for day 3 and 5 in Transwell insert (12 mm) and DWP. | 80 |
| Figure 4.12: Network formation image analysis for day 3 and 5 coculture studies in Transwell inserts and DWP. | 81 |
| Figure 4.13: Phase contrast images of HUVEC and AC16 coculture study for 5 days followed by DOX exposure for 2 days. | 82 |
| Figure 4.14: shows PDX and SKBR3 3D culture schematic in Nanoscribe devices and representative fluorescence images. | 83 |
| Figure 4.15: AIAPS Validation. (a) original images of green fluorescent microspheres were used to compare the new algorithm (AIAPS) to ImageJ analysis software. Images were analyzed using ImageJ and the AIAPS. (b) ImageJ analysis for diameter was different compared to the new algorithm AIAPS. *p < 0.05, **p < 0.001, ***p < 0.002, ****p < 0.001, n=3, and N=5 images. Low density (LD), medium density (MD), and high density (HD) microbeads were prepared using the | |

| | |
|---|-----|
| fluorescent microspheres and diluting in PBS for final microbead concentrations of 3 beads/ μ L, 50 beads/ μ L and 100 beads/ μ L, respectively. | 84 |
| Figure 5.1: Flow cytometry analysis of hiPSCs (GM25267). | 100 |
| Figure 5.2: CM differentiation protocol and flow cytometry analysis of post-differentiation day 16 hiPSC-CMs for cTnT expression. | 101 |
| Figure 5.3: Fluorescence images of 2D monolayer culture hiPSC-CMs. | 102 |
| Figure 5.4: Flow cytometry analysis of post-differentiation day 16 hiPSC-CMs for cTnT and HER2 expression. | 103 |
| Figure 5.5: Fluorescence images of 2D monolayer culture hiPSC-CMs with HER2, F-actin and DAPI. | 104 |
| Figure 5.6: Fluorescence images of hiPSC-CMs only in Transwell inserts and devices. | 105 |
| Figure 5.7: Fluorescence images of hiPSC-CM cocultured with SKBR3 in Transwell inserts and devices. | 105 |
| Figure 5.8: Fluorescence images of SKBR3s cocultured with hiPSC-CMs in Transwell inserts and devices. | 106 |
| Figure 5.9: Quantification of cell diameter for a) hiPSC-CM 3D culture in Transwell insert and devices and b) hiPSC-CM coculture with SKBR3 in Transwell insert and devices. | 107 |
| Figure 5.10: Nanoscribe device loading into bioreactor vessel (a), final assembly of bioreactor vessel (b), bioreactor vessel placement onto rotary base for simulated microgravity experiments (c), and rotational fluid flow simulation of simulated microgravity experiments (d). | 108 |
| Figure 5.11: Representative fluorescence images of control Nanoscribe hiPSC-CM samples subjected to standard incubation and simulated microgravity Nanoscribe hiPSC-CM samples (a) and image analysis of cell diameter (b) using AIAPS Script. | 109 |

List of Diagrams

| | |
|---|----|
| Diagram 1.1: Food and Drug Administration’s (FDA) typical drug development and approval process outlining the three major sections: Preclinical Research, Clinical Trials, and Review/Approval Process. This diagram was made using Canva. ^{4,7} | 2 |
| Diagram 1.2: Drug discovery and development process, highlighting the purpose of each phase and the failure rate at each phase. This diagram was made using Canva. ⁸ | 3 |
| Diagram 1.3: Discussion of different disease models with varying complexity, beginning with 2D cell culture to organ models on microphysiological systems. Some images in this diagram were obtained from Biorender and Canva was used to make the final diagram. ¹⁵ | 4 |
| Diagram 1.4: Bar graph figure comparing the number of drug approvals per disease and disorder category, including cardiovascular diseases and cancer. This diagram was made using Canva. ³ .. | 5 |
| Diagram 5.1: Technology applications 1 and 2 of the microphysiological system. | 91 |

List of Abbreviations

2D (Two-dimensional)
3D (Three-dimensional)
AC16 human cardiomyocytes (AC16s)
ACTN2 (Actinin Alpha2)
AIAPS (Automated Image Analysis Python Script)
ATP2A2 (Sarcoplasmic/endoplasmic reticulum calcium ATPase2)
BSA (Bovine serum albumin)
CaCl₂ (Calcium chloride)
CFs (Cardio fibroblasts)
CMs (Cardiomyocytes)
CTM (Cardiac tissue model)
cTnT (Cardiac troponin T)
CVDs (Cardiovascular diseases)
DMEM (Dulbecco's Modified Eagle Medium)
DOX (Doxorubicin)
DWO_P (Devices without posts)
DWPG (Devices with posts grid)
ECM (Extra-cellular matrix)
EGM-2 (Endothelial Growth Medium-2)
FC (Flow cytometry)
FEA (Finite element analysis)
HER2 (Human epidermal growth factor receptor 2)
hESCs (Human embryonic stem cells)
hiPSC-derived CMs (Human induced pluripotent stem cell derived-cardiomyocytes)
hiPSCs (Human induced pluripotent stem cells)
HUVECs (Human umbilical endothelial vein cells)
IF (Immunofluorescence)
IMSTEL (Inspired Materials & Stem-Cell Based Tissue Engineering Laboratory)
IPA (Isopropyl alcohol)
ISS (International Space Station)
MP (Moderately toxic patients, with left-ventricular ejection fraction decline)
NP (Nontoxic patients)
PBS (Phosphate buffered solution)
PDMS (Polydimethylsiloxane)
PDX (Patient derived xenograft cells)
PEGDA (Poly(ethylene glycol) diacrylate)
PFA (Paraformaldehyde)
PGMEA (Propylene glycol monomethyl ether acetate)
PPE (Personal protective equipment)
RPMI (Roswell Park Memorial Institute Medium)
RT (Room temperature)
RT (Room temperature)
RT-qPCR (Reverse transcription-quantitative polymerase chain reaction)
SD (Standard deviation)

SEM (Scanning electron microscopy)
SKBR3 (Human breast cancer line that overexpresses HER2 gene)
SLA (Stereolithography)
SP (Severely toxic patients, with left-ventricular ejection fraction decline)
SWRI (Southwest Research Institute)
TA (Technical Application)
TGF-B (Transforming growth factor beta)
TNNI1 (Cardiac troponin I1)
TNNT2 (Cardiac troponin)
US FDA (United States Food and Drug Administration)
UTEP (University of Texas at El Paso)
UV (Ultra violet)
VTM (Vascular tissue model)

Chapter 1

Introduction

1.1 BACKGROUND

Cardiovascular diseases (CVDs) are a group of disorders that affect blood vessels and the heart and are the leading cause of death worldwide, comprising 31% of total global deaths.¹ Interventions include lifestyle changes and therapeutic therapies have been used to treat and prevent the high CVD mortality rate.² However, cardiovascular drugs that have been developed resulted in increased side effects for patients with CVDs, slowing down drug discovery and development for therapeutic drugs to prevent CVDs. For these reasons, it is important to develop better ways to study cellular mechanisms, complex cellular processes, vasculature and heart physiology, disease development, and study the effects of drugs to improve clinical translation.

Drug discovery is a multi-step, complex, and expensive process that may take years to facilitate and costs about \$2.6 billion.³ In the United States, the Federal Drug Administration regulates and approves new drugs before they become available to the public. The FDA drug approval process consists of five steps, which are discovery and development, preclinical research, clinical research, FDA drug review and licensing, and FDA post-market drug safety monitoring **(Diagram 1.1)**.⁴

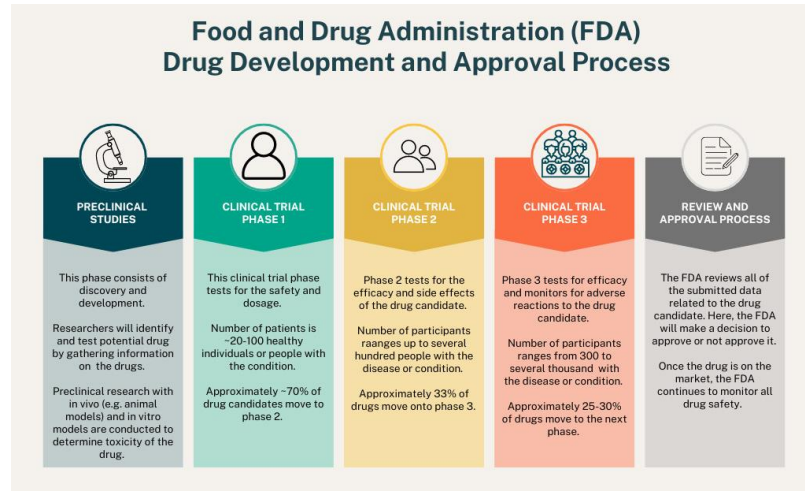


Diagram 1.1: Food and Drug Administration’s (FDA) typical drug development and approval process outlining the three major sections: Preclinical Research, Clinical Trials, and Review/Approval Process. This diagram was made using Canva.^{4,7}

The first step is discovery and development, where scientists discover new potential drugs, create a pool of drug candidates for development, the drugs’ potential benefits, and its effectiveness compared to similar drugs.⁵ The second step is composed of preclinical research with in vivo and *in vitro* models to answer basic questions about the drug’s safety, such as to determine potential harm and detailed information on dosing and toxicity levels.⁶ The third step is clinical research, where trials will be conducted in human subjects to further test the effectiveness of the drug and its harmful effects.⁷ Clinical trials follow four phases, where phase 1 is used to study the safety and dosage of the drug candidate, phase 2 investigates the efficacy and side effects, phase 3 measures efficacy and monitors adverse reactions to the drug candidate, and phase 4 determines overall safety and efficacy (**Diagram 1.1**).^{4,7}

According to the FDA, of drug candidates who advance to phase 1 clinical trials, only 70% proceed to phase 2 and by the end of phase 3, approximately 25-30% of drugs move onto phase 4 for safety and efficacy evaluation, demonstrating the narrow pipeline of potential drug candidates toward approved compounds (**Diagram 1.2**).^{7,8}

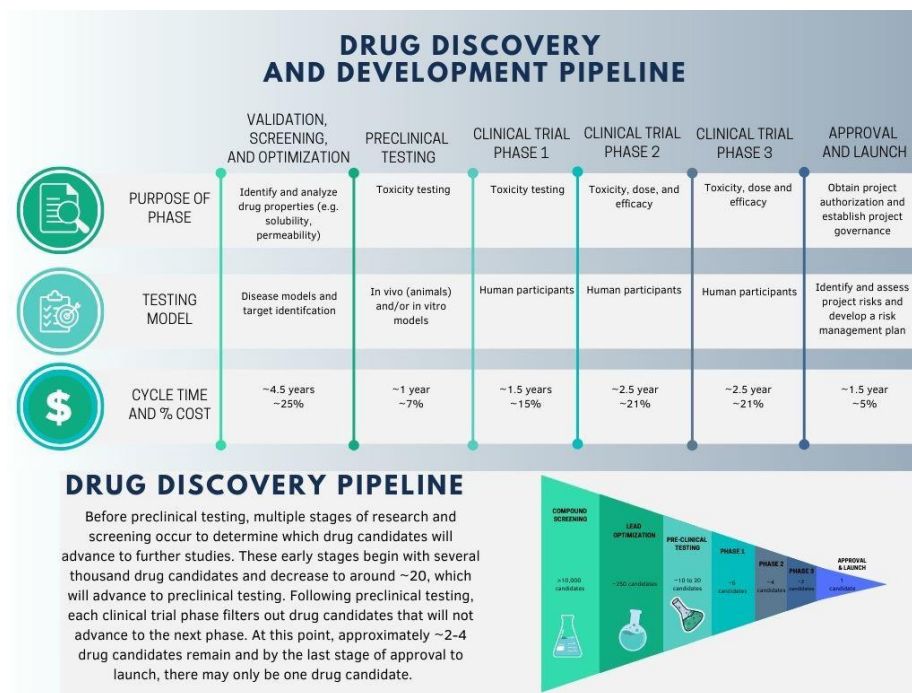


Diagram 1.2: Drug discovery and development process, highlighting the purpose of each phase and the failure rate at each phase. This diagram was made using Canva.⁸

Most of the development cost results from failure during multiple stages of development, specifically phases 1-3. These phases are the most expensive research stages, where phase 3 clinical trials with drug candidates that demonstrated unsatisfactory safety or efficacy are discontinued.⁹ A study was conducted to evaluate clinical trial data between 2010-2017 and four reasons were associated with the clinical failure of drug candidate development.⁸ These included high toxicity rates, poor drug-like properties, and lack of clinical efficacy. Additionally, another study reported failure of drug development resulted from lack of predictive translational safety from *in vitro* to in vivo models, study design outcomes, and reliance of biomarker endpoints that may not be predictive of clinical endpoints.^{9,10}

Human cardiovascular tissues and diseases are difficult to study fundamental cellular/molecular processes due to limited availability of physiologically-relevant *in vitro* models.¹¹⁻¹³ Two-dimensional (2D) cultures and animal models have commonly been used in early

preclinical phases of drug development to study cellular and disease mechanisms including absorption, excretion, distribution, and metabolism.^{14,15} 2D and animal models have provided vital information to drug development; however intercellular crosstalk and complex in vivo processes cannot be reproduced in 2D models and animal models demonstrate differences from human cardiovascular physiology including biochemical signaling, gene expression, and complex cellular processes (**Diagram 1.3**).¹⁵⁻¹⁸

BUILDING DISEASE MODELS

| Model Types | | Advantages | Disadvantages |
|--------------------------------|---|--|--|
| 2D cell culture |  <p>Cells grown in a petri dish.</p> | <ul style="list-style-type: none"> • High throughput screening • High reproducibility • Low cost | <ul style="list-style-type: none"> • Lacks complexity • Cell behavior is different compared to 3D culture |
| Organoid |  <p>An organoid developed using stem cells and extracellular matrix.</p> | <ul style="list-style-type: none"> • Provides structural complexity • Can be used for high-throughput screening • Long-term culture | <ul style="list-style-type: none"> • Low reproducibility • Difficult to image and/or screen |
| Engineered tissue model |  <p>A microfluidic device with microposts and a 3D cardiovascular tissue.</p> | <ul style="list-style-type: none"> • Can be used for high-throughput screening • Flexibility to custom build ECM or substrate for development of tissue • Model physiological and/or biochemical cues | <ul style="list-style-type: none"> • Limited lifespan • May require some technical expertise |
| Organ model |  <p>A microfluidic device used as an organ model.</p> | <ul style="list-style-type: none"> • Realistic emulation of complex physiological processes • Modeling tissue crosstalk • Modeling pathophysiological biochemical cues | <ul style="list-style-type: none"> • Low throughput • Expensive • Handling requires technical expertise • Small size |

Diagram 1.3: Discussion of different disease models with varying complexity, beginning with 2D cell culture to organ models on microphysiological systems. Some images in this diagram were obtained from Biorender and Canva was used to make the final diagram.¹⁵

Between 1937-2013, 201 molecular entities were approved for CVD treatments, where in the least 5 years, 15 therapeutic agents have been approved by the United States Food and Drug Administration (US FDA).³ In 2015-2020, a total of 245 drugs were approved in the United States, where only 6-8% were cardiovascular drugs (**Diagram 1.4**).³ In 1991, approximately 40% of drug candidates were terminated, however between 2000-2010, this number dropped to 4-5%.⁹ This

was attributed to the work conducted over the last two decades to improve *in vitro* and *in vivo* models to better evaluate cardiovascular drug candidates.

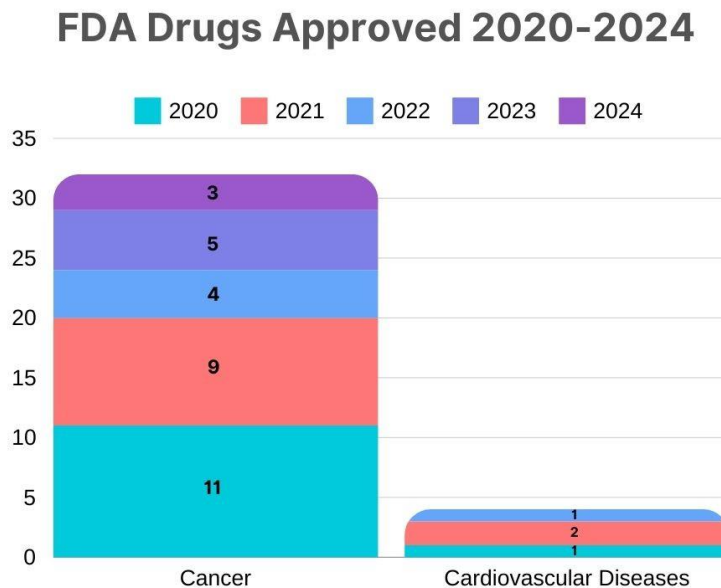


Diagram 1.4: Bar graph figure comparing the number of drug approvals per disease and disorder category, including cardiovascular diseases and cancer. This diagram was made using Canva.³

In recent years, human induced pluripotent stem cells (hiPSCs) have become an alternative model for research on human diseases and drug testing due to their potential to differentiate into different cell types, such as cardiovascular lineages.^{19,20} Patient derived hiPSCs can increase genetic diversity when the cells are differentiated into different cell types for specific studies.^{19,21} There has been significant progress for the development and optimization of directed differentiation protocols for hiPSCs into cardiomyocytes (Cms) and their incorporation into 3D *in vitro* models. Bioengineered tissue models have emerged to combine hiPSCs into an extracellular matrix (natural, synthetic, or polymer based) to create a better representative 3D model.^{15,19,20}

Bioengineered tissue models and microfluidic devices have been used to bridge 3D models and *in vivo* models. Microfluidic technology is based on the manipulation of fluids in small microvolumes and microchannels, as well as providing a controllable environment for cell culture

and drug testing.²² Microfluidic devices can be designed to include microstructures, channels, layers, and other components to mimic the cellular microenvironment and specific applications. Additionally, microfluidic devices can be designed for static or dynamic flow through the 3D tissue with or without additional systems.²³ Fabrication methods for microfluidic devices may include 3D printing, softlithography, and polydimethylsiloxane (PDMS) and sterilized for cell culture.²² Multiple cell-lineages, engineered biomaterials, and small molecules can be added into the microfluidic device to create a system capable of evaluating drug candidates at the cellular level.²⁴ Current 3D cardiovascular tissue models are mostly fabricated using PDMS or injection molding, lack physiologically relevant microenvironments that provide dynamic flow, and biophysical cues to guide cellular structural organization.

In this project, a self-driven microfluidic device will be developed for the formation of 3D *in vitro* cardiovascular and cancer tissues for preclinical drug screening applications. The microfluidic device is designed as a closed-circuit device with microposts in the tissue chamber to provide biophysical stimuli to the 3D tissues. The devices are fabricated using a benchtop 3D stereolithography (SLA) printer and clear polymer casting to allow imaging and monitoring of the 3D tissue. This device is used to develop and culture 3D cardiovascular and cancer tissues to study cellular morphology, alignment, and organization in response to biochemical and physical changes.

The proposed method of creating this platform is by culturing specific cell types (i.e: commercially available cell lines or hiPSC-CMs), encapsulating these cells into a hydrogel to form a 3D tissue, and releasing the cell-hydrogel into the tissue chamber with microposts in the microfluidic device. Microstructures within a tissue chamber have previously been used to guide cellular alignment, which makes it ideal for this project.²⁵ To mimic an *in vitro* 3D tissue, an

extracellular matrix, external stimuli, and exposure to other cell populations is needed.¹⁹ Furthermore, multicellular composition is important in mimicking the physiology and beating behavior of native cardiac tissue, as well as aiding in drug discovery because drugs may directly affect hiPSC-CMs or the surrounding cells.¹⁹ The development of a 3D microphysiological system represents a combined approach to better study cell morphology, alignment, organization and response to specific biochemical or biophysical changes, making them better models for diseases, preclinical drug screening, and developing effective therapeutics.^{17,25-30}

1.2 PROJECT GOAL, HYPOTHESIS, AND INNOVATION

The *goal* of this dissertation is to develop, optimize, and establish a human physiologically relevant 3D cardiovascular and cancer tissue model to study cell function and organization in response to biochemical and physical changes in the microenvironment.

The central *hypothesis* of this dissertation is combining 3D human cardiovascular and breast cancer tissue models within a self-driven microfluidic device will create a physiologically relevant system that facilitates *in vitro* studies of disease pathology and treatment.

The *innovation* of this dissertation is the combination of cell biology, biomaterials, and microfluidics to develop a novel self-driven microfluidic platform to improve cardiovascular and cancer *in vitro* models for preclinical drug screening.

1.3 SPECIFIC AIMS

1.3.1: Specific Aim 1

Specific Aim 1 consists of the design and fabrication of a closed self-driven microfluidic device for 3D tissue culture. Based on previous research, microfluidic devices can be designed on the principle of capillary flow which is governed by capillary effects to manipulate liquids.^{23,31} This concept can be used to control the flow of liquids within microfluidic devices to recreate fluid

flow in specific tissues or vasculature. Although, this phenomenon depends on the wettability of the device surface. We hypothesize the introduction of circular microchannels and microposts within the microfluidic device design will aid in capillary driven flow.

1.3.2: Specific Aim 2

Specific Aim 2 will describe the optimization and development of 3D cardiovascular and cancer tissue models within the microfluidic device to study cell organization and function. We hypothesize the interaction between the developed 3D tissue models (cardiovascular and cancer, respectively) and the microposts will demonstrate changes in morphology and cellular alignment to provide insight into the cellular response to the effects of biophysical stimuli.

1.3.3: Specific Aim 3

Specific Aim 3 will study the effects of biochemical and physical changes in the cardiovascular and breast cancer microphysiological systems. We hypothesize culturing hiPSC-derived cardiomyocytes in two separate technology applications (TA): TA-1) study the effects of Herceptin in a cardiovascular-cancer model and TA-2) study the effects of microgravity on cardiovascular cell morphology and functional changes. These two specific applications will develop better disease models to study complex cellular interactions, recapitulate changes that occur *in vivo* in the *in vitro* models, and drug testing feasibility.

1.4 DISSERTATION OUTLINE

Chapter 2 consists of a literature review of three separate papers which discuss major contributions to developing representative *in vitro* models for specific cardiovascular conditions. One summary will discuss the process of developing a 3D *in vitro* model with hiPSC-derived cardiovascular tissues within a microfluidic device. The following two summaries will discuss two separate applications of hiPSC-CMs to study the effects of cancer treatments and microgravity.

Together, these papers emphasize the importance of developing a system to study cardiovascular diseases.

Chapter 3 addresses Specific Aim 1. Aim 1 is the design and fabrication of a closed self-driven microfluidic device for 3D tissue culture. This chapter discusses the rationale, design process, and design evaluation for a capillary-driven microfluidic device. Fabrication processes using 3D printing and clear polymer casting, as well as validation of self-driven flow are described in detail.

Chapter 4 addresses Specific Aim 2. Aim 2 is the optimization and development of 3D cardiovascular and cancer tissue models within the microfluidic device to study cell organization and function. This chapter explains the development and optimization of 3D cardiovascular and cancer tissues within the microfluidic device and quantitative image analysis is reported.

Chapter 5 addresses Specific Aim 3. Aim 3 is the study of the effects of biochemical and physical changes in the cardiovascular and breast cancer microphysiological systems. This chapter combines all aspects of the microphysiological system, including the engineered tissue, microfluidic device, and applications to create a physiologically relevant model. Two technology applications (TA) will be described: TA-1) the effects of Herceptin in a cardiovascular-cancer model and TA-2) the effects of microgravity on cardiovascular cell morphology and functional changes.

Chapter 6 discusses the conclusions of this work and the future directions of the microphysiological system.

Chapter 2

Literature Review

Cardiovascular diseases remain the leading cause of death worldwide.¹ Although animal models have been used to produce fundamental knowledge for CVDs, translation of preclinical findings into *in vivo* human conditions has remained a challenge. *In vitro* research includes models that utilize human cells and tissues to closely study cell-cell and cell-extracellular matrix (ECM) interactions.¹⁹ Development of reproducible methods for differentiation of human stem cells, including human induced pluripotent stem cells (hiPSCs) into cardiovascular derived cells are currently used to create *in vitro* human cardiac tissue models. These models involve stem cell derived cardiac cells, co-culture of different cell lineages, and engineered platforms that can simulate stimuli experienced by native myocardium tissues, engineered biomaterials, and other design elements. *In vitro* cardiac tissue models using microfluidic platforms have been used to characterize the functionality of the engineered tissue through immunofluorescence, drug responsiveness, and other assays to provide information on the engineered tissue. Veldhuizen and Nikkah (2020) developed a microfluidic device to study 3D cardiovascular tissues and their response to drugs.²⁵ Kitani and Wu (2019), and Wnorowski and Wu (2019) used human induced pluripotent stem cell (hiPSC) derived cardiomyocytes to study effects of specific treatments or extreme conditions on cardiac function.^{32,33}

Veldhuizen and Nikkah (2020) presents a microfluidic device designed with microposts to recapitulate anisotropic structures in the human myocardium to develop a 3D cardiac tissue.²⁵ The microfluidic device was fabricated using photolithography and replica molding techniques. The device design consisted of the main tissue region with staggered elliptical microposts and trapezoidal microposts to help diffuse media to the tissue. First, the device design and coculture

rations were optimized using neonatal rat cardiac cells encapsulated into hydrogel mixtures of fibrin, collagen, and Matrigel, where the final hydrogel composition was 80:20 (collagen:Matrigel), 4:1 (cardiomyocytes CM: cardiofibroblasts CF) and device design with elliptical posts and post spacing of 150 μm and 200 μm (vertical and horizontal spacing, respectively). Human embryonic stem cells (hESCs) and human pluripotent stem cells (hiPSCs) were differentiated into cardiomyocytes. Flow cytometry and immunofluorescence showed a high percentage of cTnT+ cardiomyocytes (90.8%) and in-plate staining showed cardiac-specific expression. Coculture studies with hiPSC-derived cells were completed in 2D cultures for controls, devices without microposts, and devices with microposts for the duration of 14 days. Immunofluorescence staining of tissues in devices without posts (device controls) exhibited unaligned and random structures, while tissues in devices with microposts showed aligned structures. Moreover, cardiac gene expression of the tissues in control and device conditions, demonstrated an upregulation of maturation specific genes (ACTN2, ATP2A2, and TNNT2) compared to the 2D culture and devices without posts. Spontaneous beating signals in devices without and with posts were used to determine contraction synchronicity. Although tissues from both devices (without and with microposts) displayed similar beating rates, there was a more variability in devices without microposts. Calcium transients were analyzed in tissues developed in both devices and tissues cultured in devices with microposts demonstrated consistent and synchronous calcium transients. Lastly, epinephrine was used to test cardiac tissue responsiveness and tissues in devices with microposts displayed organized contractile patterns and a significantly higher change in beats per minute compared to devices without microposts. The 3D tissues formed in devices with posts resulted in elongated CMs, upregulation of mature cardiac-specific genes,

synchronized contractions, and response to epinephrine, creating a physiologically relevant tissue model.

Cancer is the second leading cause of death worldwide, behind cardiovascular diseases.³⁴ The types of treatment depend on the cancer type and the cancer's progression. For most individuals diagnosed with cancer, there is a combination of treatments delivered, including chemotherapy and/or radiation therapy.³⁵ However, these treatments are harsh on the body, affecting both normal, healthy cells and cancerous cells, resulting in short term side effects such as nausea and long-term effects like heart or nerve damage.³⁶ Furthermore, long-term complications of cancer therapy include cardiovascular complications, including cancer therapy-induced cardiotoxicity (CTIC).³⁷ CTIC is detected in a clinic using echocardiography, a test that uses high frequency sound waves to assess the heart's function and structures.³⁸ CTIC is identified by the reduction in cardiac left ventricular ejection fraction and this irreversible cardiac change establishes the need for models to study specific mechanisms that lead to cardiotoxicity, predictability, and treatment and/or prevention.³⁷

Kitani and Wu (2019) conducted a study to examine the effects of trastuzumab (Herceptin) in human induced pluripotent stem cells (hiPSCs) acquired from three healthy individuals and seven patients with breast cancer who were treated with trastuzumab.³² hiPSCs were differentiated into cardiomyocytes (CMs) and prepared for trastuzumab studies to recapitulate cardiac dysfunction. The first set of studies were conducted on hiPSC-CMs from healthy individuals with no history of cardiovascular disease or cancer. HER2 was also expressed in hiPSC-CMs after differentiation. hiPSC-CMs were exposed to low doses of trastuzumab ranging from 0.1 – 1 $\mu\text{mol/L}$ and evaluated for cell viability. Following 7 days of treatment with trastuzumab, hiPSC-CMs cell viability did not decrease and fluorescence staining of cardiac troponin (cTnT) and alpha-

actinin did not display any changes in sarcomere assembly. Additionally, the contractility of hiPSC-CMs following drug treatment were evaluated using high-speed microscopy, which demonstrated a significant decrease in contract velocity and deformation displacement, but no changes in the spontaneous beating rate after treatment. To further investigate the mechanisms causing contractile dysfunction in hiPSC-CMs post-trastuzumab treatment, RNA-sequencing revealed distinct changes in gene expression between untreated and trastuzumab-treated samples. Another analysis showed high occurrence of pathways related to mitochondrial dysfunction and oxidative phosphorylation. Based on this information, mitochondrial function was examined and hiPSC-CMs treated with trastuzumab did not show any major changes in mitochondrial membrane potential. However, when evaluating the mitochondrial respiratory function, there was a significant decrease in ATP-linked respiration in hiPSC-CMs treated with trastuzumab. Next, hiPSC-CMs generated from 7 patients with breast cancer who were treated with trastuzumab treatment were obtained. Three subgroups of patients were formed: nontoxic patients (NP), moderately toxic patients (MP) with left-ventricular ejection fraction decline <20-55%, and severely toxic patients (SP) with left-ventricular ejection fraction decline >20%, but <55%. Patient-specific hiPSC-CMs were treated with trastuzumab and subjected to cell viability, contractile studies, and mitochondrial respiratory studies. Cell viability post-trastuzumab treatment did not demonstrate any reduction in cell viability. Contractile studies revealed patient-specific hiPSC-CMs post-trastuzumab treatment significantly reduced contraction velocity and deformation in the SP compared to NP and MP groups. Likewise, the mitochondrial respiratory capacity post- trastuzumab treatment showed a decrease in the SP group compared to the NP group. Lastly, patient-specific hiPSC-CMs from the most severely toxic patient (SP) were used to determine the changes in contractility following treatment with trastuzumab and several

therapeutic drugs (metformin, rosiglitazone, resveratrol, lipoic acid). In earlier studies, it was observed patient-specific hiPSC-CMs treated with trastuzumab demonstrated a decrease in contraction velocity; when exposed to several therapeutic drugs, the contraction velocity was recovered. This study demonstrated human hiPSC-CMs from healthy individuals and breast cancer patients treated with trastuzumab can be used to study the cellular dysfunction produced from trastuzumab treatment and how to investigate complex interactions for treatment of cardiovascular diseases.

Spaceflight affects the human body and organ functions in several ways. Specifically, the cardiovascular system is affected during microgravity exposure and particularly for long periods of time. Astronauts on space missions have experienced lower heart rate, lower arterial pressure, and an increased cardiac output.³⁹ There is not much known of how microgravity affects cardiac function. For this reason, it is important to study the effects of microgravity on the heart and cardiovascular system. Previous microgravity research studies consisted of animal cardiomyocyte models, such as mouse or rat, and these studies revealed cardiomyocyte contractility changes and changes in mitochondrial metabolism genes.⁴⁰ However, these models do not accurately represent functions that occur in human cardiac tissues or cardiovascular system. However, studies conducted with human cells, such as human induced pluripotent stem cells (hiPSCS) differentiated into cardiomyocytes (CMs) can be used to study cellular interactions and processes that occur in microgravity.

Wnorowski and Wu (2019) send human induced pluripotent stem cell derived cardiomyocytes (hiPSC-CMs) grown and enclosed in BioCells 6-well plates to the International Space Station (ISS) for 5.5 weeks for microgravity cell culture.³³ In addition to the hiPSC-CMs on the ISS, ground samples were maintained in standard incubation conditions to assess the changes

compared to microgravity. First, hiPSC-CMs in microgravity and ground samples were evaluated for morphology and structure changes, where phase-contrast images did not show any distinct changes between both conditions. Immunofluorescence images of ground and flight samples with cardiac troponin T (cTnT) and alpha-actinin displayed standard sarcomere morphology with no significant differences in sarcomere structure or length. This demonstrates hiPSC-CMs maintained in microgravity maintained sarcomeric structure and morphology like ground hiPSC-CMs. Spontaneous beat rate for ground hiPSC-CMs and flight hiPSC-CMs was evaluated using video microscopy. After 2.5 weeks of culture on the ISS, flight hiPSC-CMs maintained a similar beat rate compared to ground hiPSC-CMs of the same culture time and flight hiPSC-CMs did not have a difference in contraction and relaxation velocities. Additionally, the calcium handling of ground and flight hiPSC-CMs was assessed. Flight hiPSC-CMs did not show a change in calcium transient amplitude but did show a significant decrease in calcium recycling rate. Furthermore, there was an increase in standard deviation of the beating rate intervals, suggesting beating irregularity. Next, gene expression of hiPSC-CMs during flight and post-flight were evaluated and sarcomeric genes cardiac troponin T (TNNT2) and troponin I1 (TNNI1) were upregulated during flight. RNA-sequencing showed genes in the mitochondrial metabolic pathway presented the most significant changes in flight vs ground hiPSC-CMs and flight vs. post-flight hiPSC-CMs. This may suggest the return to normal gravity does not restore the normal gene expression of mitochondrial gene expression after 10 days after return to normal gravity. Most of the genes that overlapped were between ground vs. flight and post-flight vs. flight, suggesting that hiPSC-CMs gene expression pattern changes during spaceflight and reverts to a similar pattern to ground controls when placed in normal gravity. It was also expressed that flight samples experienced additional factors such as radiation while on the ISS and launch and re-entry, which may have affected cellular phenotype

and gene expression. This study demonstrated the potential of hiPSC-CMs to study the effects of spaceflight and microgravity to evaluate cellular cardiac function and gene expression.

Microfluidic technology has aided in the development of more complex, representative models to study cellular processes, tissue functions, and preclinical drug screening within one platform. Microfluidic devices can be designed based on the requirements outlined by the scientist and user. Similarly, the fabrication methods for microfluidic devices have also evolved to include polydimethylsiloxane (PDMS), 3D printing, polymer casting, and many other methods, allowing the scientist to choose the fabrication method. Though there has not been a microfluidic device developed for every type of model or disease, there is the possibility of moving from traditional 2D models to incorporating 3D cell-hydrogel samples into a microfluidic device to create a more representative cellular environment. Cardiovascular-cancer models mostly consist of 2D models or organoids developed in multi-well plates. Incorporating a 3D cancer model into a microfluidic device may allow for further exploration of cellular interactions and mechanisms. Furthermore, microgravity studies are mostly composed of stem cell derived cardiovascular cells cultured in specialized multi-well plates and sent on payload space flights and do not fully recapitulate the changes that would occur in 3D. Payload flights can be expensive and may not be available to all researchers. Microgravity can be reproduced on Earth with specialized 3D culture systems, including bioreactor systems which function on a rotary cell culture system for continuous rotation. There are not many studies that combine microfluidic devices with either cardiovascular-cancer or microgravity studies of cardiovascular studies.^{41,42} Microfluidic devices with cardiovascular tissues may serve as an opportunity to explore novel ways of studies specific cellular processes and/or extreme conditions.

Chapter 3

Aim 1 - Design and fabricate a closed self-driven microfluidic device for 3D tissue culture

Part of the work presented in Chapter 3 was peer-reviewed and published in Esparza, Aibhlin, et al. "Development of in vitro cardiovascular tissue models within capillary circuit microfluidic devices fabricated with 3D stereolithography printing." SN Applied Sciences 5.9 (2023): 240.⁴³ For this reason, the information and images displayed in this chapter are based off the article referenced above. This chapter discusses Specific Aim 1.

3.1 AIM OVERVIEW

Specific Aim 1: Design and fabricate a closed self-driven microfluidic device for 3D tissue culture.

Goal: Design, manufacture, test, and obtain fluid flow rates of capillary-driven microfluidic devices.

Hypothesis: The combination of microposts and surface properties microfluidic device will function with capillary-driven flow.

Rationale: Biophysical stimuli and fluid flow integration into a microfluidic device creates a model that better recapitulates the complex cellular microenvironment.

Aim 1.1: Design capillary circuit microfluidic device for self-driven fluid flow.

Aim 1.2: Refine fabrication process of microfluidic device with 3D stereolithography (SLA) printing and clear polymer casting.

Aim 1.3: Validate self-driven flow in silico with finite element analysis (FEA) and *in vitro* experimental fluid flow studies.

3.2 ABSTRACT

Microfluidic devices are systems capable of handling small volumes and are low cost, controllable, and reproducible platforms. These platforms open the possibilities to study specific

cell processes and interactions more closely by customizing the design of the microfluidic device to fit the needs of a project. This may include designing microenvironments that can guide cell orientation and behavior, with channel spacing, microfeatures, and fluid control. Furthermore, researchers have the freedom to pick substrate material, device dimensions, and fabrication techniques to build a physiologically relevant platform. Specifically, microfluidic devices can be designed using capillary effects, which relies on the relationship between the surface tension of a liquid, geometry of microchannels, and the surface properties of the device material. These types of devices are called capillary-driven microfluidic devices and operate with the addition of liquid at an inlet to control the direction of flow into the outlet. In this chapter, the design of the capillary-driven device using the Young-LaPlace and Navier-Stokes equations for capillary fluid flow are presented. With the finalized design, the fabrication techniques using 3D stereolithography (SLA) printing and clear polymer casting will be discussed. Finally, the testing of capillary-driven flow within the devices with finite element analysis (FEA) and *in vitro* experimental fluid flow validation will be explained.

3.3 INTRODUCTION

In vitro 3D microfluidic culture systems provide an inexpensive, controlled, and reproducible platform to quantify and evaluate cellular processes in more detail.^{17,25–29,44} These systems need a physiologically-relevant microenvironment that provides dynamic fluid flow and biophysical cues to guide cellular organization.^{45,46} Customizing microenvironments within microfluidic devices may include geometries, branching structures and substrate material.⁴⁷

Fabrication techniques to make microfluidic devices include photolithography, casting, injection molding and 3D printing. Photolithography incorporates polydimethylsiloxane (PDMS), where SU-8 is used to create a master mold for PDMS microfluidic devices. However, PDMS

requires multiple steps and processes to create a final microfluidic device and can be time consuming in initial steps.^{48,49} Moreover, 3D printing has become an inexpensive, fast, and reproducible manufacturing technique. This technique gives the user the ability to print devices in a single process. 3D Stereolithography (SLA) printing operates on the principle of high-energy laser that harden liquid resin layer by layer to create a solid shape. Microfluidic devices can be 3D printed and tested with different types of cells and microenvironments to study specific interactions.^{50,51}

One type of 3D printing, 3D Stereolithography (SLA) printing, operates on the principle of high-energy laser that hardens liquid resin layer by layer create a solid shape. SLA printers are common resin printers and produce high quality prints, ideal for rapid prototyping. SLA prints are considered stronger and more durable compared to other 3D printing technologies and there is a wide range of resins that can be used for printing.⁵² Another type of 3D printing is two-photon polymerization which functions based on simultaneous absorption of two photons into a photoresist that is photosensitive. The Nanoscribe Photonic Professional GT+ printer is a system based on laser lithography that allows for the printing of high precision micro and nano structures.^{53,54} Microfluidic devices can be 3D printed and tested with different types of cells and microenvironments to study specific interactions.^{50,51}

Capillary circuit microfluidic devices function without the help of external pumps, valves, or support, and liquid movement is driven by capillary forces determined by the geometry and surface chemistry of microchannels through the microfluidic device.^{23,31} Here, the design, manufacturing process, and validation for a capillary-driven microfluidic device is presented.

3.4 MATERIALS AND METHODS

3.4.1 Capillary driven-flow microfluidic device design

The microfluidic devices presented in this section were designed based on the concept of capillary-driven flow. The device requirements included an inlet, channel, chamber, microposts, and self-driven flow. However, only a few designs were selected based on their flow rate, fabrication capability, and application to future studies. The device designs that were selected for fabrication were based on 3D stereolithography (SLA) printing and polymer casting methods. One set of single devices and another set of closed-circuit devices operate on the principles of capillary action, which allows for continuous fluid movement without the need for external support.

Microfluidic capillary pumps incorporate different geometries of microstructures and surface properties to generate capillary pressure and self-regulated liquid delivery.³¹ The final capillary-flow microfluidic device was designed in Solidworks CAD Software (Solidworks Corporation) with the Young-LaPlace and Navier-Stokes equations for capillary fluid flow with dimensional constraints dictated by the printing resolution of a Formlabs Form3B SLA printer and Formlabs V4 Clear Resin.

Based on the design considerations, capillary pressure and flow rate were numerically calculated. Capillary pressure occurs at the liquid-air interface within a microchannel as a result of surface tension of the liquid and the curvature formed by the wettable contact angle. The Young-Laplace equation outlines the relationship between contact angle, microchannel size, and capillary pressure (Eq. 1).³¹

$$P = -2\gamma \left[\frac{\cos \theta_t + \cos \theta_b}{h} + \frac{\cos \theta_l + \cos \theta_r}{w} \right] \quad [\text{Eq. 1}]$$

Where P is the capillary pressure, γ is the surface tension of the liquid, h is the channel height, w is the channel width, θ_t is the contact angle of the liquid with the top microchannel wall,

θ_b is the contact angle of the liquid with the bottom microchannel wall, θ_l is the contact angle with the left microchannel wall, and θ_r is the contact angle with the right microchannel wall.

The contact angle on the microchannel walls is equal for devices built from a single material.³¹ A contact angle of 72°C was used for the microfluidic devices in this work based on the contact angle studies on the Ostemer.⁵⁵ Surface tension of water at room temperature (γ) and the height and width of the microchannels of the devices were used to calculate capillary pressure.

The Navier-Stokes equation assumes a laminar, steady state flow, and absence of gravitational effects to evaluate the flow rate (Q) of a liquid in a microchannel. The equation is as follows:³¹

$$Q = \frac{h^3 w \Delta P}{12 \eta L(\epsilon)} \left[1 - 0.630 \frac{h}{w} \right] \quad [\text{Eq.2}]$$

Where h is the microchannel height, w is the microchannel, ΔP is the difference in capillary pressure across the microchannel, η is the fluid dynamic viscosity, and L is the length of liquid in the microchannel. The height and width of the microchannels and dynamic fluid viscosity of liquid water at room temperature were used to calculate the flow rate.

With these considerations, several device designs were created, where **Figure 3.4** and **Table 3.4** show the design evolution and dimensions.

3.4.2 Three-dimensional (3D) printing techniques

1. 3D (SLA) Stereolithography printing

A Formlabs Form3B SLA printer with Clear V4 resin (Formlabs, Somerville, Massachusetts) was used to print microfluidic devices and inverted device molds with a printing resolution range of 25-100 μm and wavelength of 405 nm. The microfluidic devices and inverted device molds were designed in Solidworks and uploaded to PreForm 3D Printing Software (Formlabs). Printing supports were autogenerated and the print job was initiated. The printing time

ranged from 1-2 hours depending on the overall dimensions and intricate features of the device and/or inverted mold.

After printing, post-processing techniques were followed as recommended by the manufacturer for Clear V4 resin (Formlabs, Somerville, Massachusetts). Prints were removed from the build platform and submerged in the Form Wash (Formlabs) with fresh isopropyl alcohol (IPA) for 10 minutes.⁵⁶ The prints were air dried in the Form Wash rack. The prints were added into Form Cure (Formlabs) and ultraviolet (UV) cured at 60°C for 15 minutes. After the cure, flush cutters (Formlabs) were used to carefully remove the supports from the 3D prints molds.⁵⁶

II. 3D printing with Nanoscribe Quantum X Printer

Device 7b with microposts was downscaled by a factor of 0.8 and prepared to print using a Nanoscribe Photonic Professional printer (Karlsruhe, Germany), which used two-photon lithography polymerization to produce 3D structures. IP-Q (Nanoscribe, Karlsruhe, Germany) resin allows for high-speed fabrication of millimeter sized designs and used for micro rapid-prototyping was used for the printing resin.⁵⁷ The printing resolution of the Nanoscribe printer is in the range of 200-300 nm, which is ideal for investigating the feasibility of developing a microfluidic device with higher range 3D printing technologies. The microfluidic device file was downscaled in Solidworks using the Scale Function and saved as an .stl file. The entire process of printing and processing Nanoscribe prints is outlined below.⁵⁸

The .stl file was uploaded into DeScribe, a print job development software for the Nanoscribe 3D printer. The 3D model was centered to ensure it would fit within the square silicon substrate (3D LF DiLL) and identified as a solid for high accuracy printing. The GWL print job files were saved. The substrate was cleaned by rinsing the reflective side with acetone, isopropanol, and distilled water. The surface of the substrate was blow dried to remove moisture. The substrate

was transferred to the sample holder and fixed by placing sticky tape along the edge of the substrate on two opposite ends. The 10x objective was inspected and cleaned prior to starting the print. The objective was cleaned with isopropanol and dried. A silicon ring was placed on the objective to prevent resin from spreading on the objective lens. The objective was placed on the nose piece. IP-Q resin was added to the center of the clean substrate, approximately the size of a 1cm circle, and allowed to spread across the substrate.

Next, the microscope objective was positioned at the lower z-limit and the user interface program to control the 3D printer, NanoWrite, was launched. After the NanoWrite initialization, the Exchange Holder was selected, and the sample holder was carefully inserted with the label “TOP” facing upwards. The objective was moved towards the interface by selecting Approach Sample, to put the working distance to the interface in focus. To load the job, the print job saved as a .GWL file was selected and imported, where NanoWrite will load the data automatically. After completing all of these steps, the printing process is initiated by clicking Start Job.

To unload the 3D print, click Exchange Holder, allow the stage to move and objective lower to the z-drive limit, and remove the sample holder. The substrate is then removed from the sample holder and submerged in a bath with SU-8 developer propylene glycol monomethyl ether acetate (PGMEA) for 20 minutes to wash away excess liquid resin. Then submerged in isopropyl alcohol (IPA) for 5 minutes to wash the developer away and blow dried. To remove the 3D print from the substrate, the substrate is placed on top of a heating plate for 1 minute and lightly sprayed with IPA on the sides of the print to slide the 3D print off the substrate.

3.4.3 Contact angle tests

To calculate capillary pressure and flow rate using the Young-LaPlace and Navier-Stokes equations, it was necessary to calculate the contact angles of the Formlabs clear resin, the

Nanoscribe IP-Q resin, and Ostemer322, a clear polymer used for microfluidic device fabrication. Although some materials are identified for their uses in biomedical engineering and prototyping applications, it is important to investigate the applications of 3D printing resin, its biocompatibility, surface properties.^{59,60} A contact angle test can be used to determine a material's surface properties, including its wettability.

All samples were subjected to contact angle experiments the same day (Day 0). The squares were placed on a flat stage and a 20 μ L pipette with DI water was placed directly on top. With the pipette, a droplet of DI water was released onto the surface of the Ostemer square. After the formation of the droplet on the surface, images were captured with a Canon SX620 HS camera placed directly in front of the stage holding the square. Images were analyzed with Drop Analysis ImageJ plugin to determine contact angles.⁵⁹ Averages and standard deviation were calculated in Microsoft Excel using "AVERAGE" and "STDEV.S" commands.

3.4.4 Fluid flow finite element analysis (FEA)

To further evaluate the device designs and their potential for sustaining fluid flow, designs 2 and 3-7 were evaluated using FEA. Design 2, an early design, was evaluated for fluid flow with finite element analysis (FEA) using Ansys Fluent (Canonsburg, PA). The simulation study parameters were modeled after human capillary blood flow velocity ranging from 0.04 to 1.2 mm/s to determine flow rate within the 3D printed device.⁶¹ The procedure for FEA with Ansys Fluent steps is described here.⁶² The 3D model was saved as an .IGES file and uploaded into the mesh folder. An automatic mesh for the model was created by selecting quadratic or tetrahedral, depending on the complexity of the region with microposts. The inlet, outlet, and chamber regions were identified by selecting each feature and naming them individually. Air and liquid water at room temperature were assigned to either the device interface, or the faces that would interact with

the liquid (i.e: inlet, channels, chamber, outlet). The inlet velocity was set to 0.04 mm/s, the system was initialized, and the calculation was started. Contour and pathway graphics for the fluid flow were selected and the scenes were saved.

The next set of designs 4-7 were further validated with FEA using COMSOL Multiphysics software (Burlington, Massachusetts) (**Figure 3.5**). The computational simulation study parameters were modeled after experimental results from fluid flow experiments using Trypan Blue diluted in Phosphate Buffered Solution (PBS) to compare flow velocities. The procedure for FEA with COMSOL Multiphysics steps simulation began with importing the 3D model of the microfluidic device and selecting stationary Laminar Flow study. Liquid water at room temperature (RT) was selected for the simulation. Inlets and outlets were added, named, and assigned inlet velocities based on initial fluid flow experiments, outlined in **Table 3.1**. The study was conducted, and the velocity magnitude graphs were saved.

Table 3.1: Assigned inlet velocities for each device design for FEA fluid flow studies.

| Design | Assigned Inlet Velocities |
|---------------|----------------------------------|
| 1 | No study conducted |
| 2 | 0.04 mm/s |
| 3 | No study conducted |
| 4 | 0.04 mm/s |
| 5 | 0.04 mm/s |
| 6a | 0.02 mm/s |
| 6b | 0.02 mm/s |
| 6c | 0.02 mm/s |
| 7a | 1.39 mm/s |
| 7b | 1.87 mm/s |

3.4.5 Device fabrication optimization

Three different processes were combined to create the final microfluidic devices, including 3D printing, polydimethylsiloxane (PDMS) silicon molds, and polymer casting with Ostemer322.

First, the microfluidic devices were either printed using Formlabs or Nanoscribe 3D printers. The 3D prints were post-processed according to the resin and type of 3D printer used.

I. PDMS mold fabrication

Next, the PDMS molds were prepared. Dow SYLGARD 184 Silicone Elastomer Clear was used to make flexible, PDMS molds for the microfluidic devices. SYLGARD 184 components base and curing agent were mixed according to the manufacturer ratio of 10:1 (base to curing agent, respectively).⁶³ Each component was weighed, added into a conical tube, and mixed. The mixture was centrifuged to remove air bubbles.

To create molds of the microfluidic devices, the 3D printed microfluidic device was placed into an aluminum pan (14.5 cm wide x 7.6 cm depth x 5 cm height) with the solid back of the device in contact with the bottom of the pan. The PDMS mixture was poured on top of the device. Air bubbles were removed by placing the pan using a vacuum chamber for 5 minutes. Next, the pan was placed into a furnace (ThermoScientific Lindberg/BlueM Moldatherm Box Furnace) at 110°C for 35 minutes to heat cure the mold. The mold was allowed to cool down and the 3D printed device was removed from the PDMS mold.

II. Ostemer322 polymer casting

Next, the clear polymer Ostemer322 was prepared for casting to fabricate the final microfluidic device. The final microfluidic devices were fabricated with Ostemer 322, a clear UV-curable resin, a material Dr. Joddar introduced our lab to.⁶⁴ The material Ostemer 322 will henceforth be referred to as Ostemer and any or all devices fabricated with Ostemer322 will be referred to as Ostemer devices, All work with Ostemer was completed inside of a chemical fume hood and with personal protective equipment (PPE), including a lab coat and gloves. The approximate volume needed to fill the molds for the device were calculated (circuit device: 12 mL,

nanoscribe device: 500 μ L). Ostemer bottles were referenced for specific mixing ratios for component A and B (A:B, 1.09:1, respectively).⁶⁴ The following equation was used to calculate how much of each component was needed:

$$1.09A : 1 B, \text{ let } B = x$$

$$1.09x + 1x = \text{desired final volume (i. e: 20 g)}$$

$$2.09x = 20g$$

$$x = 9.57$$

$$\text{So } A = 1.09x = 1.09(9.57g) = 10.43 g$$

$$A = 10.43g, B = 9.56g$$

Component B was measured first, followed by Component A. A wooden stirrer was used to mix both components to ensure a homogenous mixture and centrifuged for 3 minutes at 1300 RPM to remove air bubbles.

The PDMS mold was cleaned with tape to remove any debris. The liquid Ostemer mixture was slowly poured into the PDMS mold and air bubbles were removed with a pipette tip. The PDMS mold was placed in the Formlabs UV cure machine for UV curing at 60°C for 3 minutes. The Ostemer slightly hardens during the UV cure and the device is removed from the PDMS mold by bending the mold. The Ostemer devices are then subjected to a heat cure 90-100°C in a furnace (ThermoScientific Lindberg/BlueM Moldatherm Box Furnace). The PDMS mold was reused to make a total of 10 devices before the mold showed signs of damage (e.g tears in the mold) or decreased quality of the final devices (e.g. missing microposts, uneven surfaces of the channel or chamber).

3.4.6 Fluid flow validation experiments

Designs 4-7 of microfluidic devices underwent initial fluid flow experiments to determine capillary-flow within the device. A Canon PowerShot SX620 HS camera was placed on a tripod positioned above the microfluidic device. The camera was set to video and the recording was started once the microfluidic device was set in frame. This set up was repeated for each microfluidic device.

The liquid (Trypan Blue and PBS) was added into the microfluidic device as outlined here. Trypan Blue (Fisher Scientific) and PBS (1x, Gibco) at a ratio of 0.1 to 10, respectively, were mixed thoroughly. Trypan blue (100 μL) and PBS (10 mL) were measured into a 15 mL conical tube and mixed. A standard 1000 μL pipette was used to release the liquid into the inlets of each device. **Table 3.2** describes the volume loaded into each device design.

Table 3.2: Volumes of Trypan Blue and PBS added to microfluidic devices for fluid flow studies.

| Design | Name | Posts? | Volume Added |
|---------------|--|--------|--------------------|
| 1 | | Yes | No study conducted |
| 2 | | Yes | No study conducted |
| 3 | | Yes | No study conducted |
| 4 | | Yes | 100 μL |
| 5 | | Yes | 100 μL |
| 6a | Device without Posts (DWO _P) | No | 1000 μL |
| 6b | Device with Posts Grid (DWPG) | Yes | 1000 μL |
| 6c | Device with Posts Staggered (DWPS) | Yes | 1000 μL |
| 7a | Device without Posts (DWO _P) | No | 2000 μL |
| 7b | Device with Posts (DwP) | Yes | 2000 μL |
| 7b Nanoscribe | Nanoscribe | Yes | 20 μL |

For microfluidic device designs 4-5, the liquid was loaded into the left channel of the device. For designs 6-7, the liquid was loaded into a cut standard 1000 μL pipette tip to fit the

circular inlet of the microfluidic device. The cut pipette tip was placed in the inlet of the device and 1000 μL of the Trypan Blue and PBS mixture was released into the cut pipette in the inlet of the microfluidic device with a new, uncut pipette tip. Another 1000 μL was measured and released into the inlet. Similarly, designs 7 were subjected to fluid flow experiments without a pipette tip to further evaluate fluid flow through the device. Trypan Blue and PBS were allowed to flow from the inlet to the outlet of the device, without any external aid. The experiment concluded when the outlet was either filled, or the flow remained stationary over the course of an hour. The same steps were repeated for all devices.

I. Dynabead fluid flow studies

A similar process was repeated with Dynabeads (M-280, ThermoFisher) diluted in PBS at 1:10 ratio. The Ostemer device (design 7b) was placed onto the microscope platform and positioned in frame. Videos were recorded using a stereomicroscope (Swift Microscope World, Carlsbad, California). The video was started prior to loading the mixture into the inlet. The liquid was allowed to flow throughout the device and the video was stopped. Only a fraction of the device was visible under the microscope, due to the overall size dimensions of the device (50 x 40 mm). Additional videos were recorded at different locations in the device after the liquid mixture was added.

II. Fluorescence microspheres fluid flow studies

Fluorescent beads (Red Aqueous Fluorescent Particles, ThermoFisher) were diluted in PBS at a 1:50 ratio and loaded into the inlet of each Ostemer device without posts (design 7a), device with posts (design 7b), and Ostemer Nanoscribe device. A time lapse video was recorded on a Leica Thunder Imaging Live Cell and 3D Assay fluorescent microscope (Leica Microsystems, Buffalo Grove, IL) using a 10x objective. Only a fraction of the device was visible under the lens,

due to the overall size dimensions of the device designs 7a and 7b (50 x 40 mm). Time lapse videos were recorded at the inlet and microchannel for additional views.

III. Additional fluid flow experiments

Furthermore, to access the mixing of liquid after loading, two different colored solutions were diluted in PBS and placed into inlets of the Ostemer device (design 7b) to visualize mixing and flow through the device. Videos were recorded using a Canon PowerShot SX620 HS camera placed on a tripod positioned above the microfluidic device. The camera was set to video and the recording was set once the microfluidic device is set in frame.

3.4.7 Statistical Analysis

All quantitative measurements were performed at least in triplicates and values are expressed as mean \pm standard deviation (SD).

3.5 RESULTS

3.5.1 Contact angle

To calculate capillary pressure and flow rate using Young-LaPlace and Navier-Stokes equations, the contact angle for the Clear V4 resin (Formlabs), IP-Q (Nanoscribe) and Ostemer322 were needed. In **Figure 3.1**, the experimental setup of the contact angle experiment is shown and was repeated for all materials.

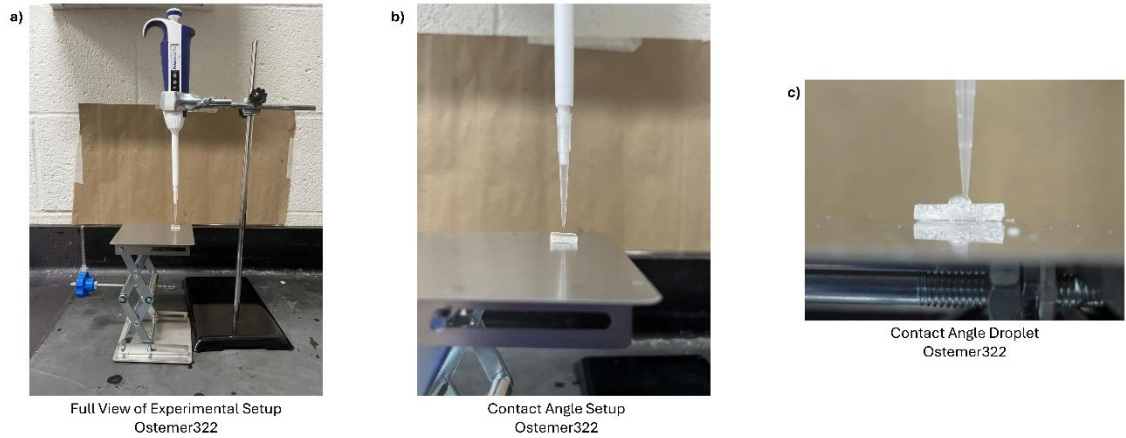


Figure 3.1: Contact angle experimental setup for Ostemer322.

The contact angle for the clear resin ranged from 50-70° depending on post-print day, as reported in a study conducted by our lab.⁶⁵ Similarly, IP-Q resin from Nanoscribe printer was subjected to contact angle studies, where **Figure 3.2** shows the experimental setup for the Nanoscribe samples and the ImageJ analysis for contact angle.

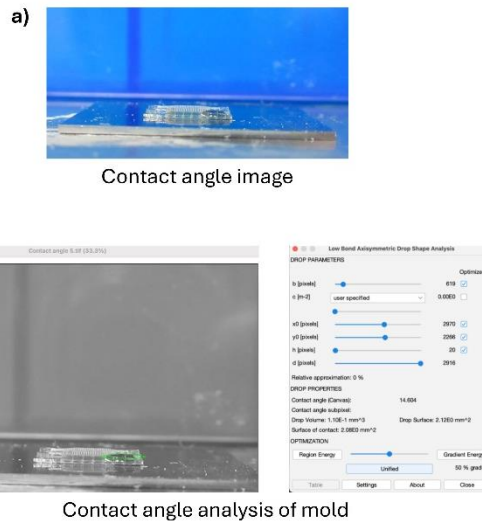


Figure 3.2: Experimental setup for Nanoscribe contact angle test and contact angle analysis using ImageJ/Fiji.

The IP-Q Nanoscribe resin resulted in an average value of 14° (± 0.11 , $n=3$). The contact angles of the Ostemer had an average value of 72° (± 8.29 , $n=20$). **Figure 3.3** and **Table 3.3** compare the contact angle of all three materials. A contact angle less of 90° indicates high surface energy, which suggests the polymer hydrophilic and supports capillary action and flow when used as a microfluidic device.

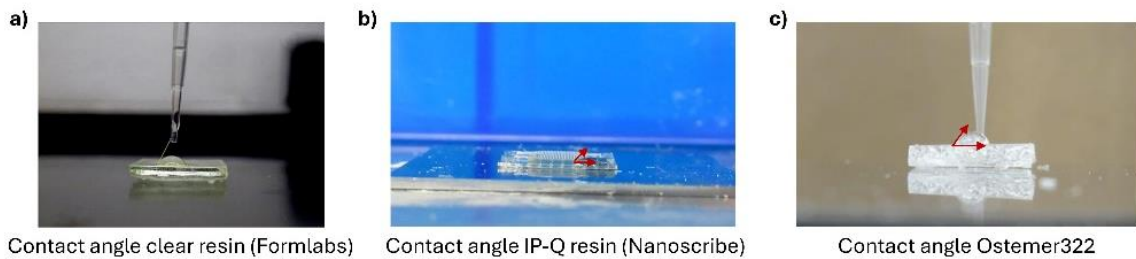


Figure 3.3: Representative contact angle images for clear resin (Formlabs 3D printer), IP-Q resin (Nanoscribe 3D Printer), and Ostemer322.

Table 3.3: Comparison of contact angle values.

| Material | Manufacturer | Contact Angle |
|-----------------|---------------------|-----------------------------|
| Clear resin | Formlabs | 53.1° (± 4.67) |
| IP-Q resin | Nanoscribe | 14° (± 0.11) |
| Ostemer322 | Mercene Labs | 72° (± 8.29) |

3.5.2 Fluid flow Finite Element Analysis (FEA)

Figure 3.4 shows the design evolutions of all devices designed. This section will describe fluid flow simulations for designs 2-7. Designs that were designed in Solidworks were saved as .STL files and then subjected to FEA fluid flow simulations. Early design 2 was analyzed using Ansys Fluent software and designs 3-7 were analyzed using COMSOL Multiphysics (**Figure 3.5**).

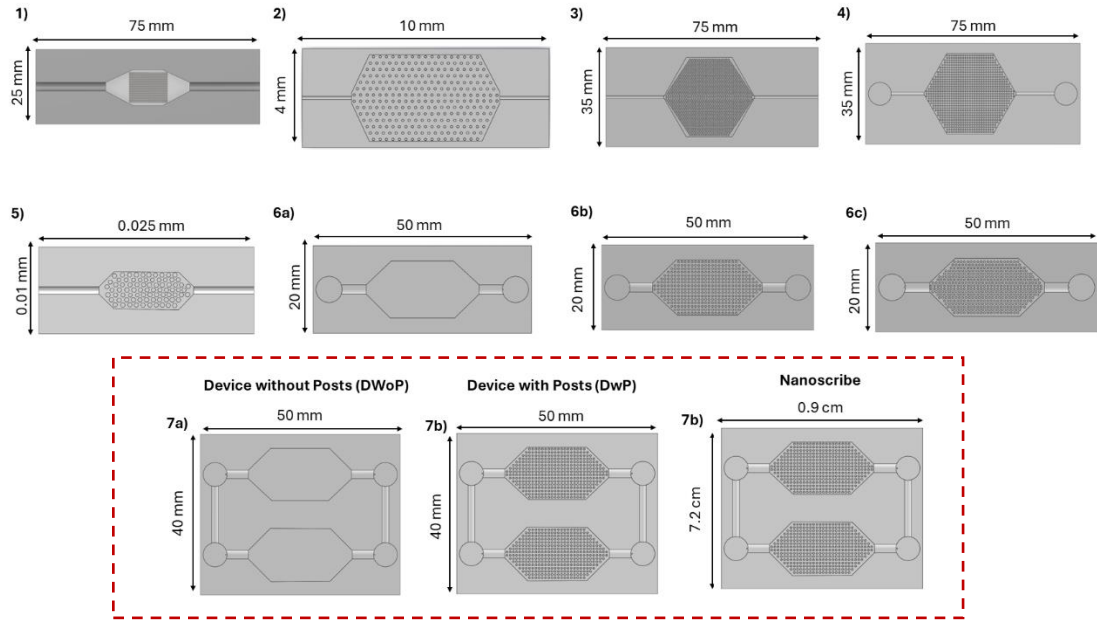


Figure 3.4: Microfluidic device design evolution. Multiple 3D models are presented from the early stages of this study into the final devices used for future experiments (outlined in red).

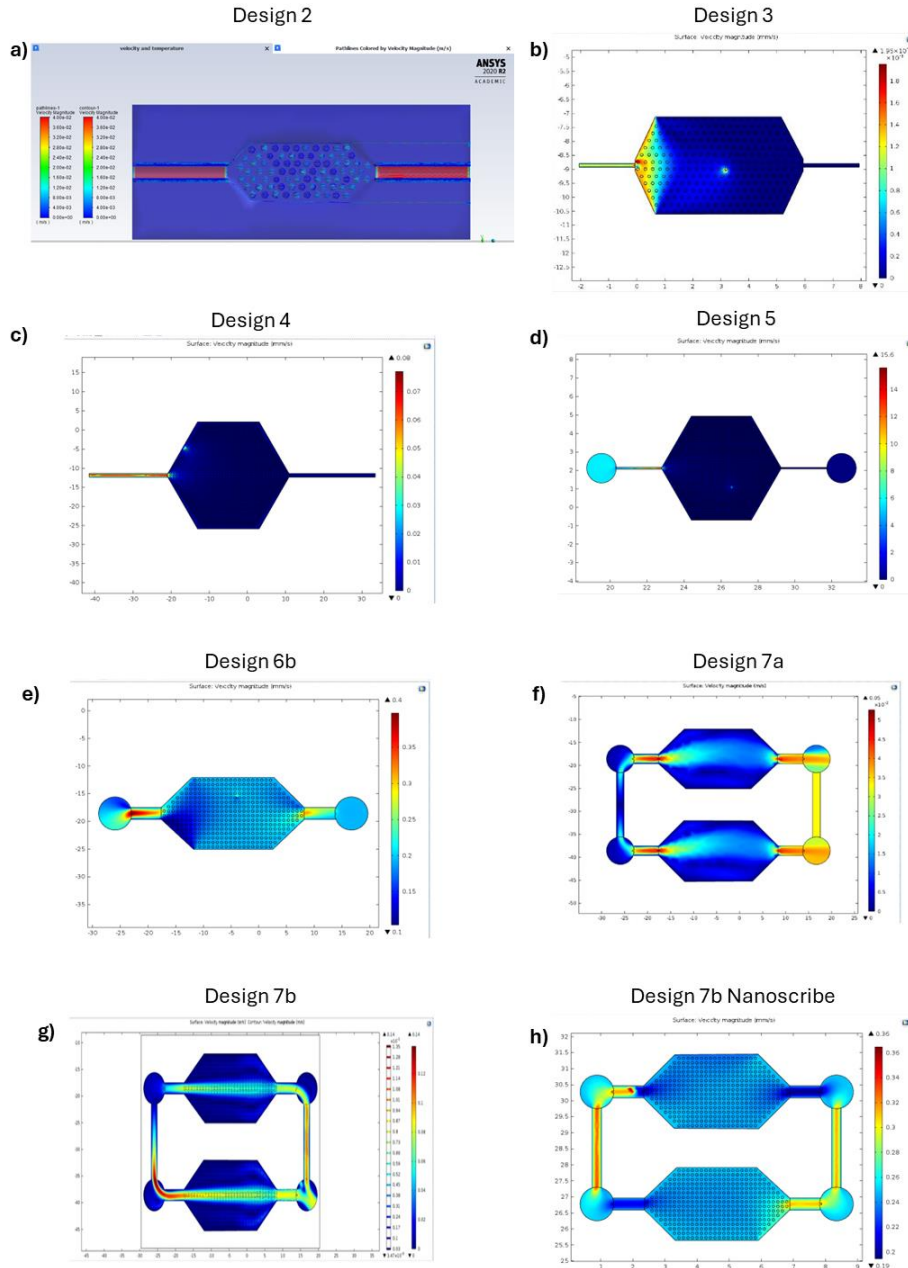


Figure 3.5: FEA analysis of devices 2-7.

Device designs 2-5 faced several design problems. These specific designs had a small, shallow inlet that was designed to not hold a substantial volume. Similarly, the channel width and length were not proportional to the size of the chamber. For these reasons, the fluid flow was not sufficient to flow through the entire device. Designs 6-7 incorporated these changes and this allowed the fluid to move through the entire device as presented in the simulations. Design 6 and

its iterations followed similar fluid flow trends in the FEA simulations. The fluid movement from the inlet to the outlet of the device is consistent and steady. Design 6 was a precursor to Design 7, where design 7 was designed as a capillary-circuit device. Design 7a (device without posts, DWoP) and 7b (device with posts, DWP) used the average fluid velocity of 1.87 mm/s (± 0.81 , n=5) for DWoP and 1.39 mm/s (± 0.20 , n=5) for DWP. The respective FEA models for these devices (7a and 7b) show the flow at the inlet split evenly into both channels leading into the tissue chambers. When the flow reaches the outlets of the device, there is an increase of fluid flow allowing the fluid to continue moving into the second tissue chamber. Based on the FEA simulations, designs 6 and 7 demonstrate promise for capillary-driven flow and were used for future experiments, including fluid flow validation and cell culture experiments.

3.5.3 Optimization of Formlabs 3D Printing

Microfluidic devices are systems that operate using small amounts of fluids and have features, such as channels, with sizes ranging in the micrometer to nanometer scale.⁶⁶ Microfluidic devices are versatile and can be applied in various applications. With these considerations, the initial design requirements included an inlet, outlet, a chamber, and channels connecting all components together. Each component serves a purpose, such that the inlet is where liquid would be added, the channels would deliver the liquid from the inlet to other areas of the device, and the chamber is where the cells or tissue would be added. Additionally, microfeatures in microfluidic devices have played a role in cellular alignment and capillary fluid flow and for this reason, microposts were added into the design requirements of the device.

To begin the design process, preliminary models were designed in Solidworks, saved as .STL files, and 3D printed using a 3B Formlabs SLA printer. There were many design iterations, all designed with the concept of capillary-driven flow. **Figure 3.4** shows the entire design

evolution for this project. The first set of designs did not have a distinctive inlet or outlet and had a large chamber compared to the size of the channels compared to later adapted versions. Designs 6 and 7 would be used for future experiments based on their design and fluid flow properties. The chamber region includes hundreds of microposts, where all designs feature different dimensions, including micropost size, post spacing, and post arrangement as outlined in **Table 3.4**.

Table 3.4: Design parameters for each microfluidic device concept.

| <u>Design</u> | <u>Name</u> | <u>Length x Width</u> | <u>Height</u> | <u>Post Size</u> | <u>Post Height</u> | <u>Post Spacing</u> | <u>Channel Length</u> |
|---------------|------------------------------------|-----------------------|---------------|------------------|--------------------|----------------------------|-----------------------|
| 1 | n/a | 75 x 35 mm | 2 mm | 0.10 mm | 0.05 mm | 0.05 mm | 23 mm |
| 2 | | 10 x 4 mm | 0.2 mm | 0.10 mm | 0.05 mm | 0.15 mm (h&v) | 2 mm |
| 3 | | 75 x 35 mm | 4.5 mm | 0.25 mm | 0.8 mm | 0.3 mm (h) 0.4 mm (v) | 22 mm |
| 4 | | 75 x 35 mm | 4.5 mm | 0.25 mm | 0.8 mm | 0.3 mm (h) 0.4 mm (v) | 22 mm |
| 5 | | 0.025 x 0.01 mm | 0.003 mm | 50 um | 0.001 mm | 50 um (h&v) | 0.007 mm |
| 6a* | Device without Posts (DWO P) | 50 x 20 mm | 4.5 mm | n/a | n/a | n/a | n/a |
| 6b* | Device with Posts Grid (DWPG) | 50 x 20 mm | 4.5 mm | 0.25 mm | 0.8 mm | 0.3 mm (h&v) | 5.5 mm |
| 6c* | Device with Posts Staggered (DWPS) | 50 x 20 mm | 4.5 mm | 0.25 mm | 0.8 mm | 0.26 mm (h) 0.17 mm (v) | 5.5 mm |
| 7a* | Device without Posts (DWO P) | 50 x 40 mm | 3.25 mm | n/a | n/a | n/a | n/a |
| 7b** | Device with Posts (DwP) | 50 x 40 mm | 3.25 mm | 0.25 mm | 0.8 mm | 0.3 mm (h&v) | 15 mm |
| 7b** | Nanoscribe | 0.9 x 7.2 cm | 0.5 mm | 0.01 mm | 0.14 mm | 0.05 mm (h) 0.06 mm (v) | 2.45m |

Legend: h = horizontal spacing, v = vertical spacing, * = used for cell experiments in Aim 2, ** = final device used for Aim 2 and Aim 3

I. Micropost size and spacing

Design 1 was the first prototype to be 3D printed and it was used to determine the printing capabilities of the 3D printer. The microposts were originally designed as hexagons with intermittent spacing between each post of 0.3 mm. During the PreForm quality check, there were no potential errors identified by the software. Following post-processing, the 3D printed device was placed under a light stereomicroscope and examined closely. **Figure 3.6** shows three different areas of the microfluidic device post-printing. The microchannel was clear and easily discernable from the solid face of the microfluidic device, as seen in **Fig. 3.6a**. The channel leads directly into the chamber and the first set of microposts are visible, however, they are circular instead of hexagonal (**Fig.3.6b**). Amid the microposts, there are areas where it seems as if some microposts merge with neighboring microposts, identified by red dashed circles (**Fig.3.6c**). When comparing the 3D model to the final 3D print, there were some differences, such as the shape of the microposts and resin in between posts, indicative of a printing tolerance. Based on these observations, the spacing between microposts was increased to avoid merging of microposts as demonstrated in future designs. In a similar way, the micropost size was optimized, to the smallest the 3D printer was capable of printing while avoiding merging of the microposts. These changes were implemented in early designs 2 and 4 and completely adopted in the later, finalized designs.

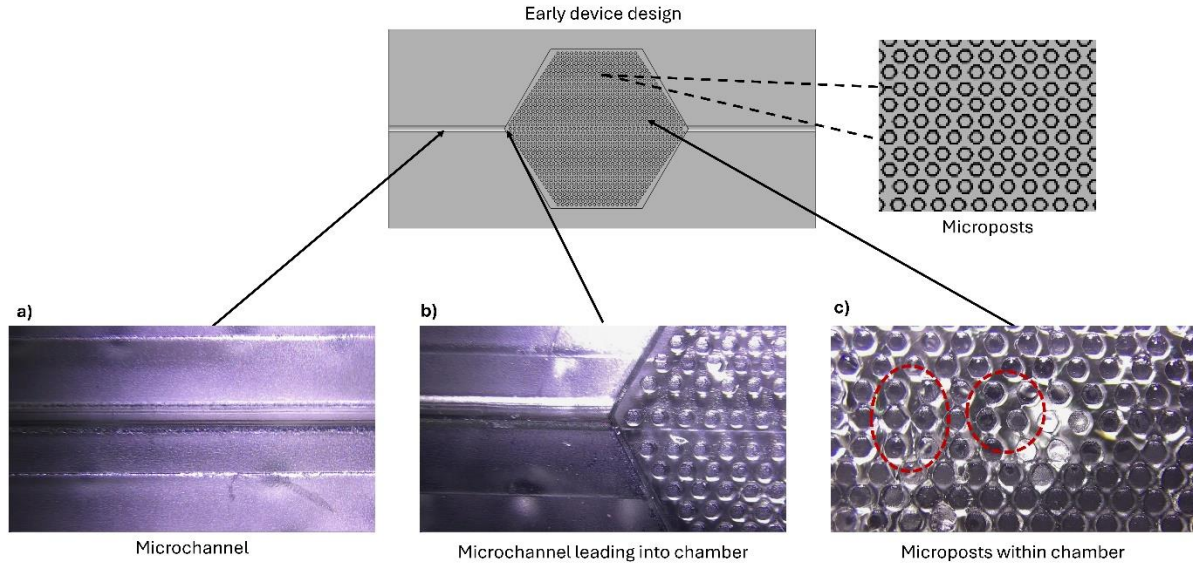


Figure 3.6: Post-processed 3D printed device to assess printing accuracy. a) shows the first microchannel, b) shows the microchannel leading into the chamber and some microposts, and c) shows microposts in the chamber.

II. Visibility of 3D printed devices

Several 3D printed devices were made using the same clear SLA resin and post processed following the manufacturer's recommendations. These devices were placed under a benchtop light microscope and fluorescence microscope (3D Leica microscope) to test optical clarity for future use in cell culture or 3D tissue development. **Figures 3.7 and 3.8** show the images captured with both types of microscopes using a 3D printed device.

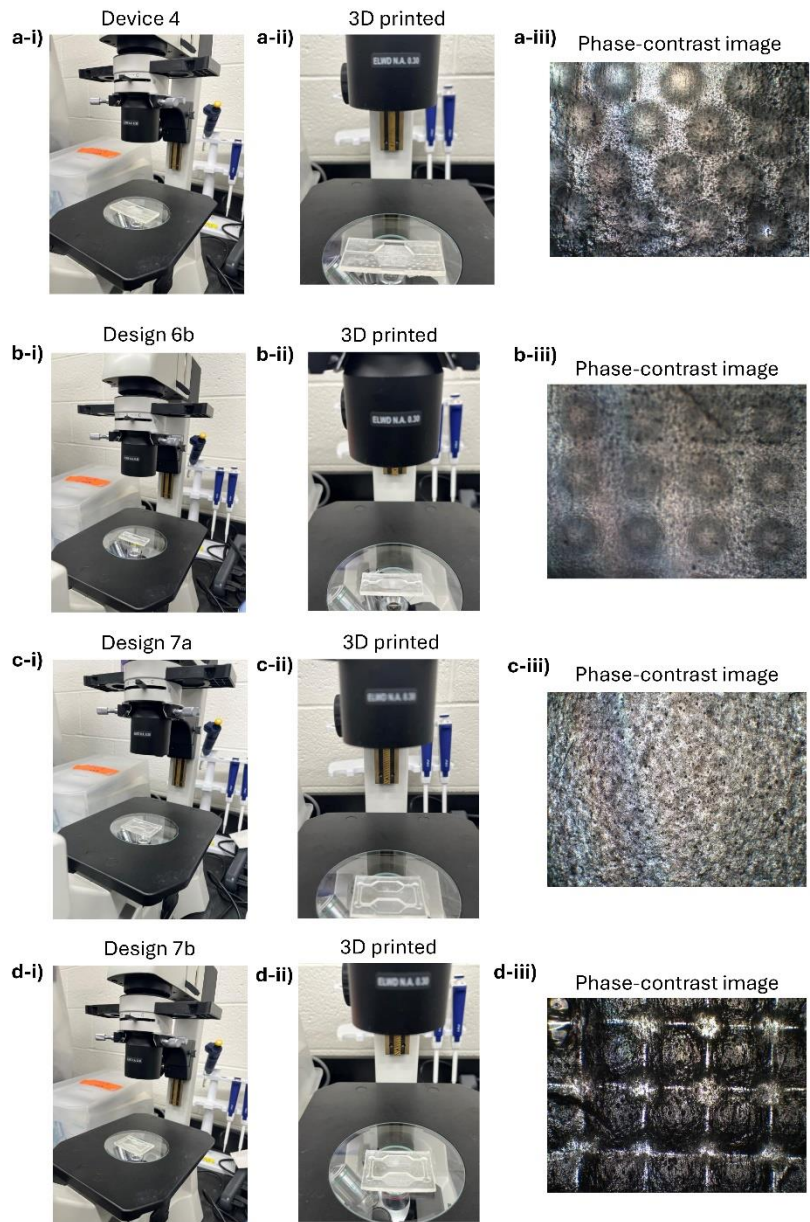


Figure 3.7: Images acquired using a benchtop light microscope of various 3D printed devices.

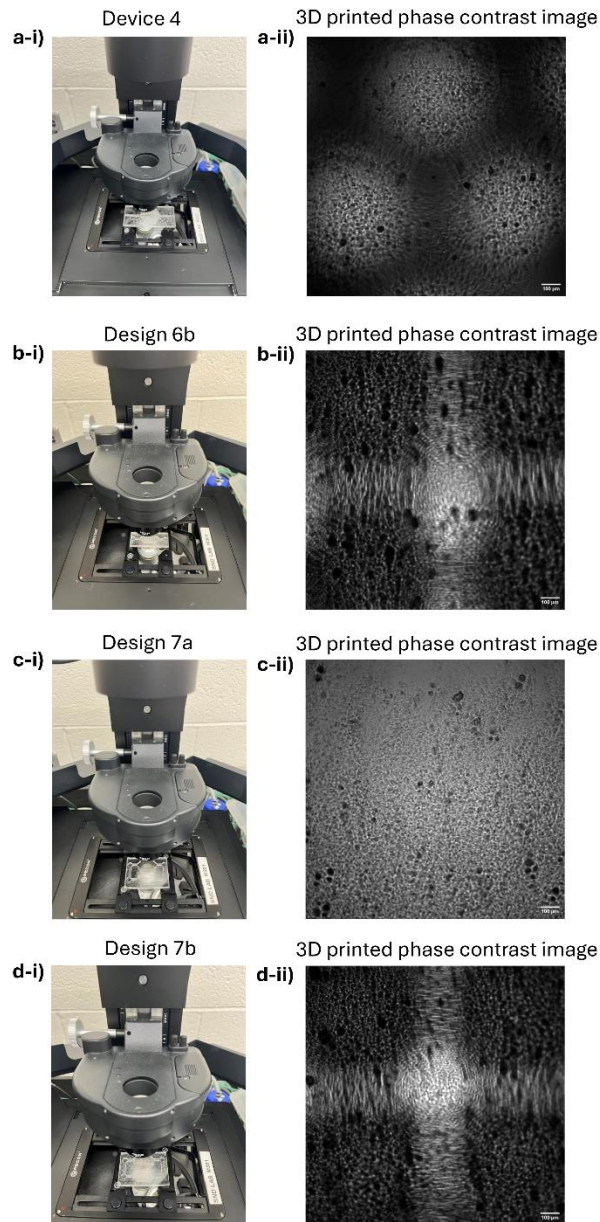


Figure 3.8: Images acquired using fluorescence microscope (Leica Thunder Imager) of various 3D printed devices.

Images acquired with both the light and fluorescence microscope show 3D printed devices are not completely visible. For future implementation in cell culture and tissue development, this could make it difficult to image samples within the 3D printed devices. Furthermore, after repeated

prints and post-processing, the finish of the 3D printed devices varies. **Figure 3.9** shows two 3D printed devices printed within the same month with the same resin cartridge.

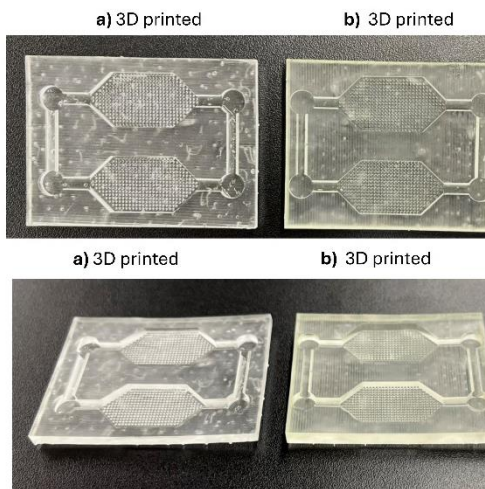


Figure 3.9: Two 3D printed devices printed within the same month with the same resin cartridge.

The final finish of the device depends on resin shelf age, post processing techniques, and printing with or without printing supports. During post processing techniques, the isopropyl alcohol (IPA) plays a heavy role in the final finish of the device. It is recommended for the wash station to be cleaned and filled with fresh IPA once a month for low printing and every 2 or 3 weeks with consistent 3D printing. This is to ensure the IPA can remove all or most of the resin adhered to the 3D print.

III. Material change to Ostemer322

To address the issue of clarity, the Inspired Materials & Stem-Cell Based Tissue Engineered Laboratory (IMSTEL) and Dr. Joddar, shared a material called Ostemer 322 with our lab. Ostemer 322 is a high transparency, clear UV-curing resin used for developing microfluidic devices. The focus shifted from implementing 3D printed devices in future cell studies to using Ostemer 322 to create the final, clear devices. The following sections describe the polymer casting process in two different types of molds (3D printed and PDMS).

IV. Improvement of mold creation and utilization for polymer casting of Ostemer322

The 3D printed molds were created by inverting the microfluidic device and printed using the Formlabs SLA printer. There were two different 3D printed molds designed as seen in **Figure 3.10**. The first design is one single piece containing the inverted geometry to make a device without microposts. The second design consists of two parts, the border enclosing liquid resin and the inverted geometry of the device. The molds were used to cast Ostemer322 to create the final devices. However, there were many challenges with this fabrication technique. The removal of the device from the printed mold was difficult due to the stiffness of the mold. A spatula was then used to help remove the device from the mold, however, this often would leave scratches on the surface or completely break the device. Heat seemed to play a key role in removal from the mold to obtain devices with little to no damage by immediately removing the device after the thermo-cure in the furnace. The two-piece mold was slightly easier to use but shared the same issues with integrity of the device features and removal from the base. This technique yielded 1-2 devices from a single 3D printed mold. The integrity of the microposts decreased after the second use of the printed mold. This process required multiple printed molds to produce sufficient final devices.

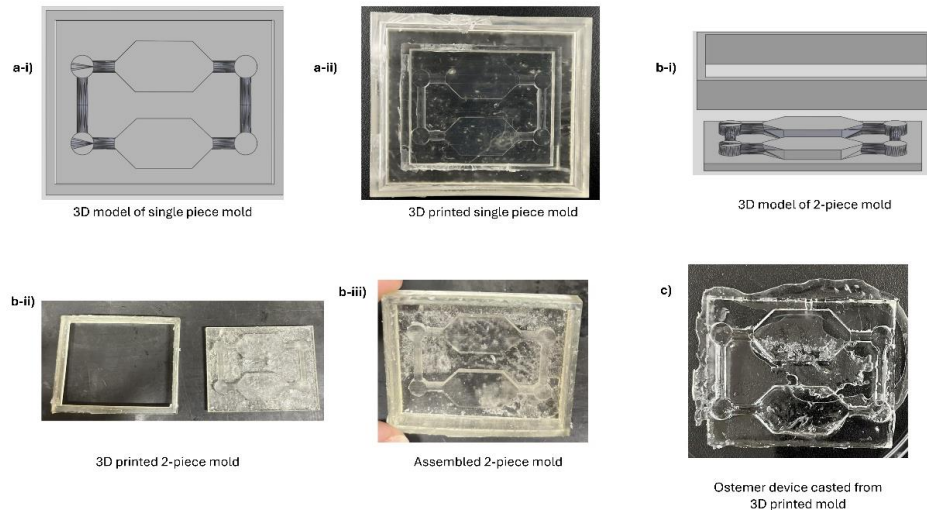


Figure 3.10: 3D printed molds for circuit device without posts (DWoP) and the resultant Ostemer device.

To optimize this process, polydimethylsiloxane (PDMS) molds were made for Ostemer322 casting. This fabrication technique greatly improved the structure and integrity of the entire device. Instead of casting into a 3D printed mold, the device was 3D printed, post processed, and PDMS was prepared and poured over the printed device and thermo-cured. The 3D printed device was extracted from the PDMS mold. The entire process for polymer casting these devices is explained in **Figure 3.11**. Under the inspection of the mold under a stereomicroscope, the micropost indents, inlets, and channels in the mold were preserved. The PDMS mold was then used for clear polymer casting to create the final, Ostemer322 devices. The PDMS mold could be used repeatedly without significant damage to the mold.⁶⁷⁻⁶⁹ The 3D printed device could be used repeatedly to make more PDMS mold. Adjusting the method of creating the mold significantly improved the workflow of device creation, the number of devices produced, and consistent features within the devices. The final devices after casting maintained all features, were clear, and visible through different microscopes (**Figure 3.12**).

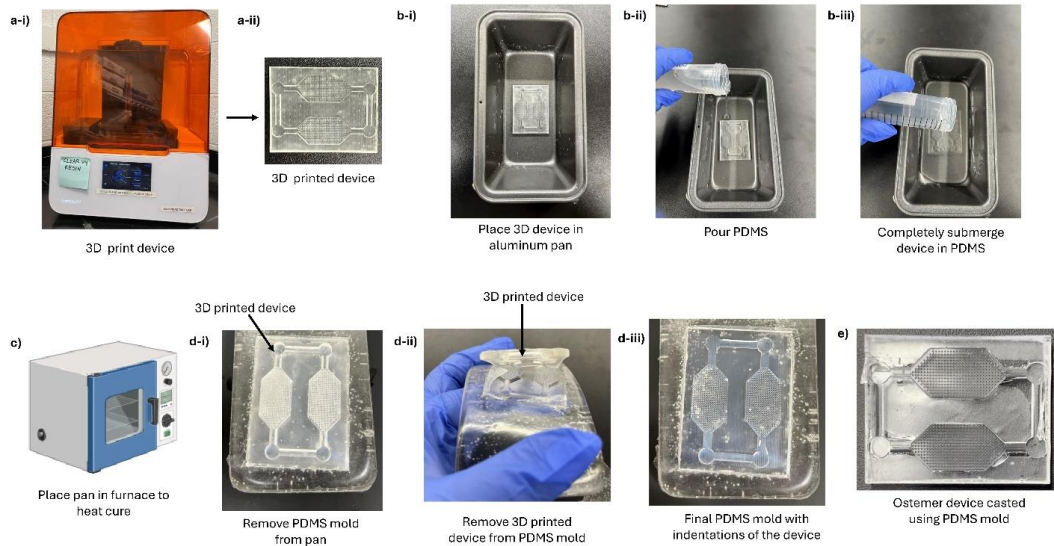
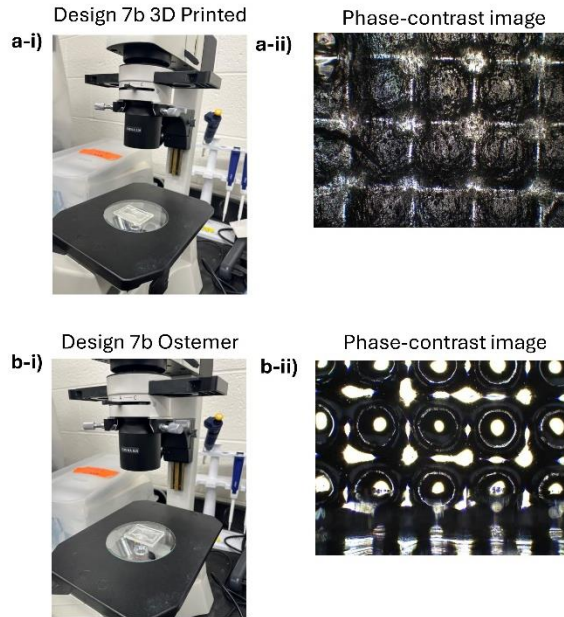


Figure 3.11: Outlines the process of 3D printing a device, creating a PDMS mold, and Ostemer322 casting to create final Ostemer device.

Light Microscope



Fluorescence Microscope

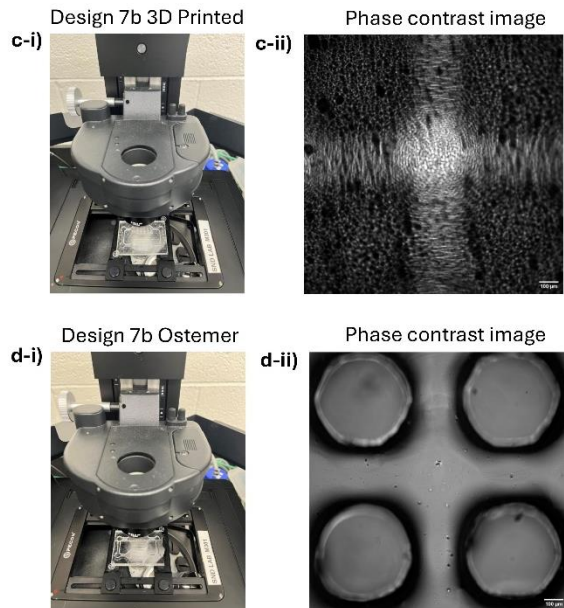


Figure 3.12: Compares 3D printed devices and fabricated Ostemer322 devices under light and fluorescence microscopes.

An additional study revealed Ostemer devices that are not used 1-5 days after the fabrication date will auto-fluorescence when observed under a fluorescence microscope. **Figure 3.13** shows two devices fabricated with Ostemer on different days and imaged using the 3D Leica

Thunder Imaging microscope. The device made and imaged on the same day displays little autofluorescence as seen by the light green background. The second device was fabricated more than a month prior to the image presented and shows more green background. ImageJ/Fiji can be used to remove some background; however, it is apparent the longer the devices are not used, the device changes. It is recommended to fabricate the devices one day prior or the day of experiments to eliminate the chance of autofluorescence. The scope of this project did not include investigating the material changes over time.

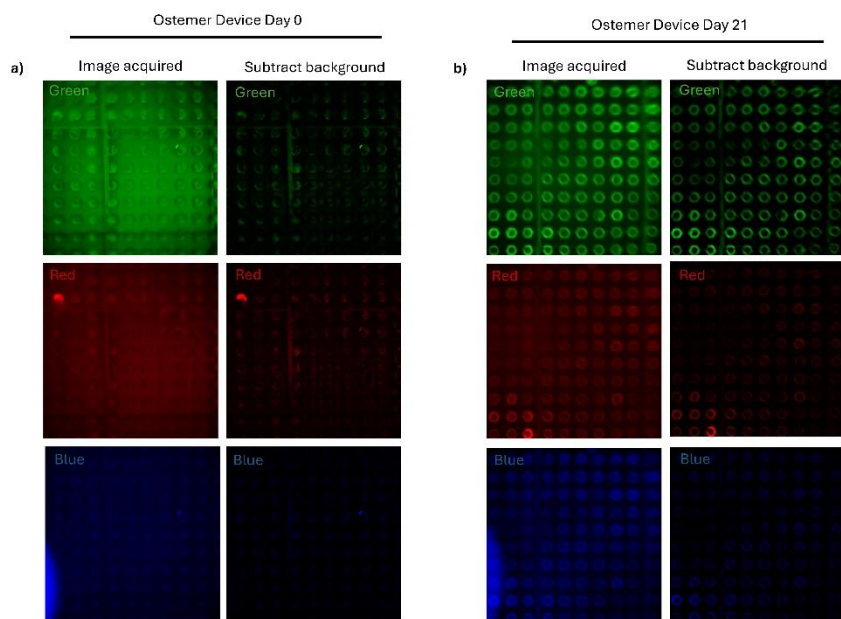


Figure 3.13: Autofluorescence comparison between Ostemer devices fabricated on different days.

3.5.4 Nanoscribe device fabrication

Design 7 was downscaled to explore the potential of using the Nanoscribe printer as a fabrication method, less material to fabricate and use the microfluidic devices, and how a smaller device would affect cell interactions in future experiments.

The Nanoscribe 3D printer demonstrated a high printing resolution over the course of a long print time (~43 hours) for one print. Device 7b (device with posts, DWP) was downscaled

and uploaded to the Nanoscribe system. **Figure 3.14** shows the first 3D printed device using the Nanoscribe printer, henceforth referred to as Nanoscribe device.

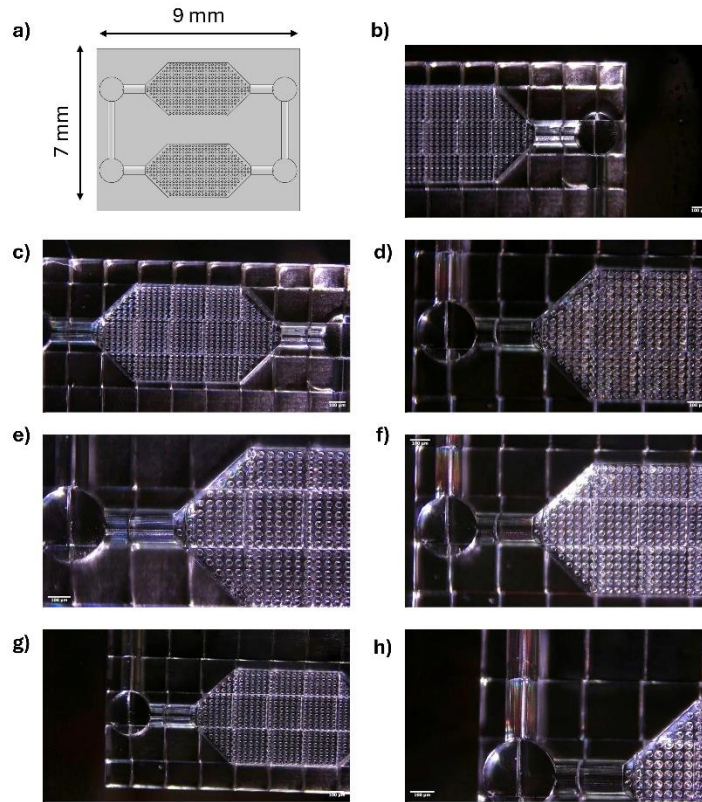


Figure 3.14: Nanoscribe device CAD model and stereomicroscope images of first Nanoscribe print.

Many 3D printers have the capability to print multiple models at once. The Formlabs 3B printer was capable of printing 4-6 devices in one session with a print time ranging from 4 -6 hours. The Nanoscribe 3D printer was tested to determine if it was possible to print more than one device in a print session. **Figure 3.15** shows the printing concept of a 2 x 2 array for a total of 4 devices. After approximately 63 hours, the Nanoscribe printer printed 1 device successfully outlined in a red rectangle, with parts of the other three devices. After troubleshooting, it is possible to print 4 devices if the layout of the devices is centered on the wafer. However, the total print time has

increased substantially in this case. Furthermore, the properties of the IP-Q resin were not evaluated for biocompatibility or application of 3D cell culture.

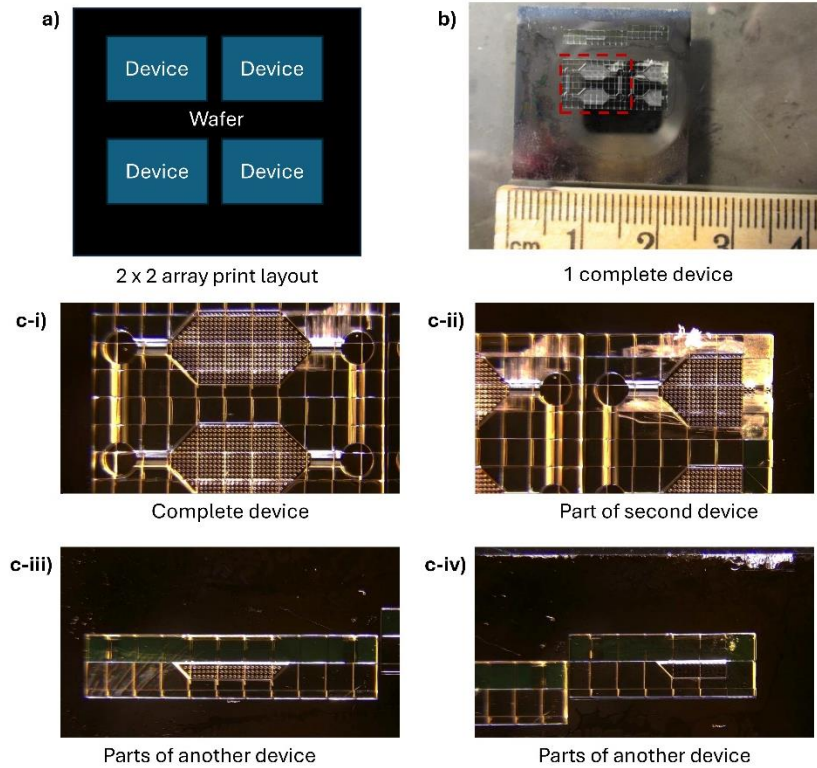


Figure 3.15: Attempt to print multiple devices on one single wafer using Nanoscribe 3D printer.

I. Mold creation and polymer casting of Ostemer322 for Nanoscribe devices

Similarly, Nanoscribe devices printed using the Nanoscribe Photonic Professional GT2 system, were used to make PDMS molds following the same protocol outlined in previous sections. With the PDMS mold, Ostemer322 was casted to make final Nanoscribe devices with Ostemer322. **Figure 3.16** compares the size of a device with posts (DWP) and the Nanoscribe device.

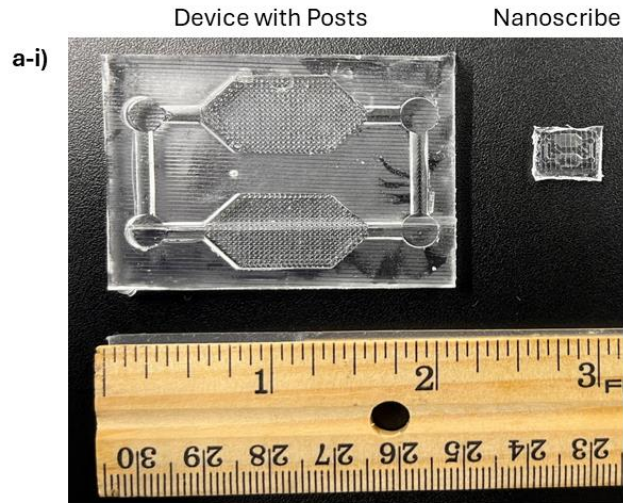
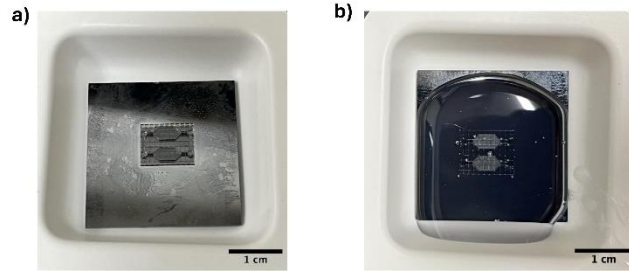


Figure 3.16: Overall size dimension comparison between Ostemer devices with posts and the Nanoscribe device.

Even at this small scale, it was possible to retain the microscale features and manufacture multiple devices using the same mold. Scanning electron microscopy (SEM) images of Nanoscribe 3D printed and Ostemer322 devices confirm the resolution of all features are maintained (courtesy of Brittany L. Stark) in **Figure 3.17**.

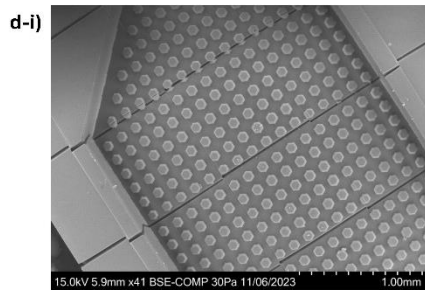


Nanoscribe printed mold

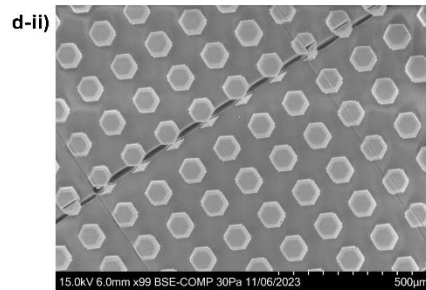
PDMS poured on top of print to create PDMS mold



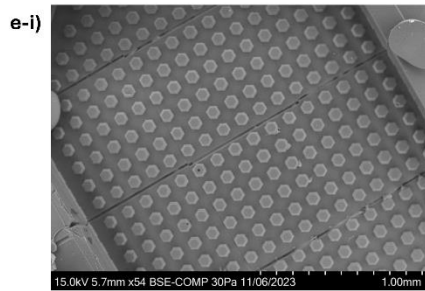
Final Ostemer casted device



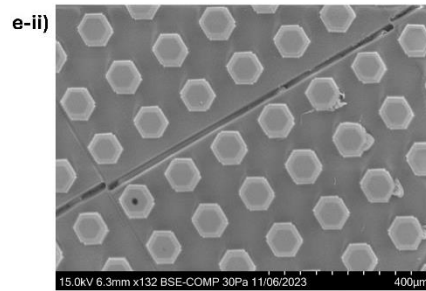
3D printed Nanoscribe device
SEM Image



3D printed Nanoscribe device
SEM Image



Ostemer322 casted Nanoscribe device
SEM Image



Ostemer322 casted Nanoscribe device
SEM Image

Figure 3.17: PDMS mold and Ostemer322 Nanoscribe device process. Scanning electron microscopy (SEM) images of 3D printed Nanoscribe device and Ostemer322 casted Nanoscribe device.

3.5.5 Capillary fluid flow validation experiments

Validation experiments for microfluidic devices were performed to confirm the system's ability to use and/or maintain capillary fluid flow.

1. Fluid flow experiments for 3D printed devices and Ostemer devices

Fluid flow experiments were conducted with Trypan Blue and PBS with 3D printed devices and Ostemer devices. **Figure 3.18** shows time lapse images of various 3D printed devices from early designs and Ostemer devices of later designs. **Table 3.5** outlines the fluid velocity for each device design either 3D printed or Ostemer322 casted devices.

Table 3.5: Fluid velocities of 3D printed and Ostemer devices.

| Design | Posts? | 3D Printed or Ostemer | Fluid Velocity | Flow? |
|---------------|---------------|------------------------------|---------------------------------|--------------|
| 6a | No | 3D printed | 0.238 mm/s (± 0.11 , n=3) | Yes |
| 6b | Yes | 3D printed | 0.043 mm/s (± 0.11 , n=3) | Yes |
| 6c | Yes | 3D printed | 0.143 mm/s (± 0.026 , n=3) | Yes |
| 7a | No | 3D printed | 2.34 mm/s (± 0.20 , n=5) | Yes |
| 7a | No | Ostemer | 1.39 mm/s (± 0.20 , n=5) | Yes |
| 7b | Yes | 3D printed | 2.80 mm/s (0.35, n=3) | Yes |
| 7b | Yes | Ostemer | 1.87 mm/s (± 0.81 , n=5) | Yes |
| 7b Nanoscribe | Yes | Ostemer | 0.009 mm/s | Yes |

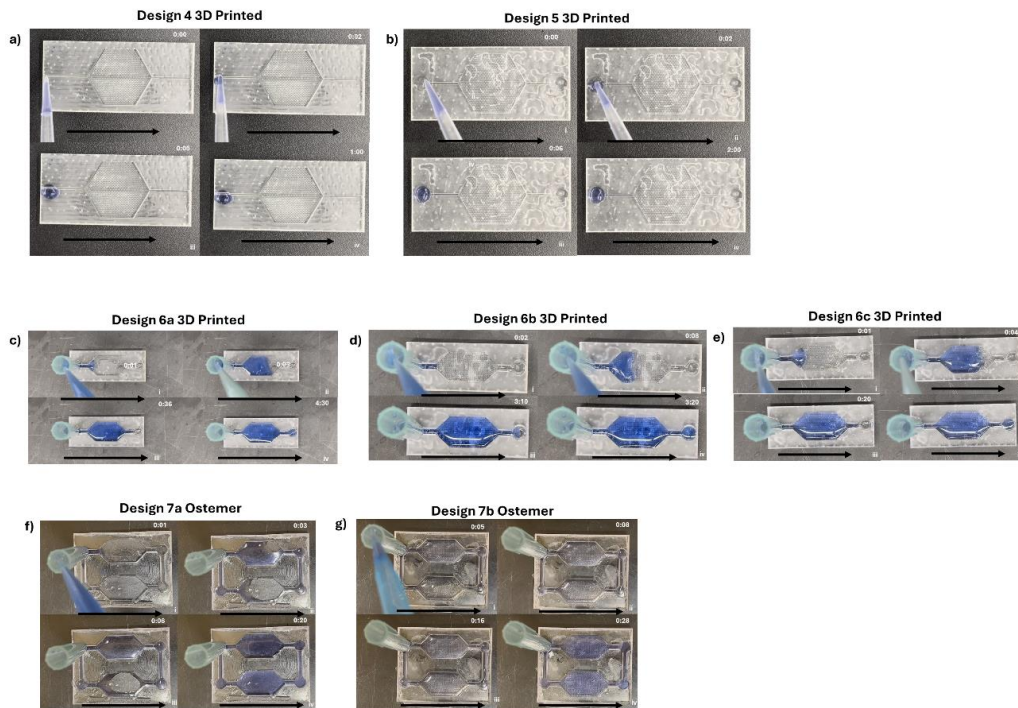


Figure 3.18: Time lapse picture of Trypan Blue and PBS through different device designs of 3D printed or Ostemer devices.

Designs 4 and 5 were 3D printed and were not able to maintain capillary-driven flow throughout the device. Design 4 did not have an inlet, only a channel leading into the main chamber, which made it difficult to add a substantial amount of fluid to the device. Design 5, on the other hand, was designed with a circular inlet and still did not allow fluid flow. This can be attributed to the small depth of the inlet, the size of the channel and the chamber. The dimensions allowed for only a small volume of liquid to be added and it was not enough to flow through the whole device. However, designs 6 and 7, regardless of the fabrication type, 3D printing or Ostemer casting, allowed fluid to flow throughout the device with capillary-action. This was possible due to several design modifications including: increased depth of the inlet to hold ~1 mL of liquid, increased width and decreased length of the channel, and reduced width and length of the chamber. Additionally, design 6 was the precursor to design 7, the circuit device. Design 6 consisted of a device without posts, device with posts in a grid formation, and device with posts in a staggered

formation to evaluate if the formation of the posts played a role in fluid flow. After conducting fluid experiments, the devices with posts resulted in a faster velocity compared to devices without posts. This trend was the same in design 7 devices, the capillary circuit device.

To further evaluate the fluid flow, Ostemer devices with outposts (DWoP) and with posts (DWP) were tested without the pipette at the inlet. **Figures 3.19** and **3.20** show the time lapse images of the fluid flow experiment without the pipette. Both devices hold a maximum of 2 mL and the fluid flow through the device took approximately 6 minutes.

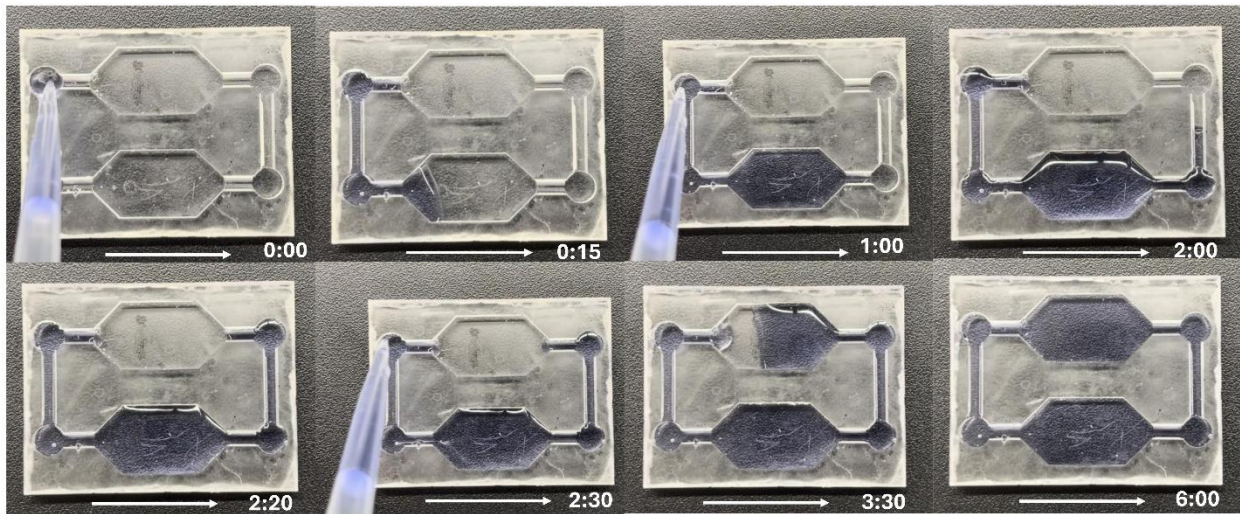


Figure 3.19: shows a time lapse of Trypan Blue and PBS through the device without posts (DWoP).

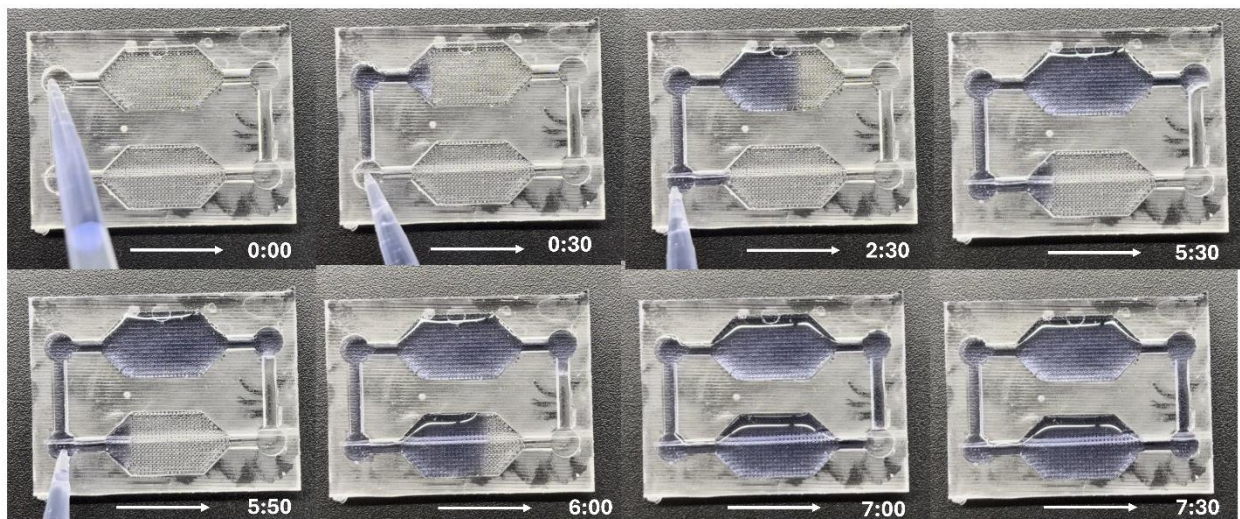


Figure 3.20: shows a time lapse of Trypan Blue and PBS through the device with posts (DWP).

Similarly, the Nanoscribe device was tested for fluid flow under a stereomicroscope with red dye and PBS to provide better contrast. **Figure 3.21** shows a time lapse of the Nanoscribe device. The device holds a maximum of 20 μL in the device and the inlet diameter is approximately 1.5 μm , like the diameter of a 10 μL pipette tip. The fluid flow through the Nanoscribe took 55 minutes to complete, with the addition of 0.5 μL over the course of the total time. The addition of liquid into the inlets of the Nanoscribe device may serve as a challenge, as it's difficult for the user to see.

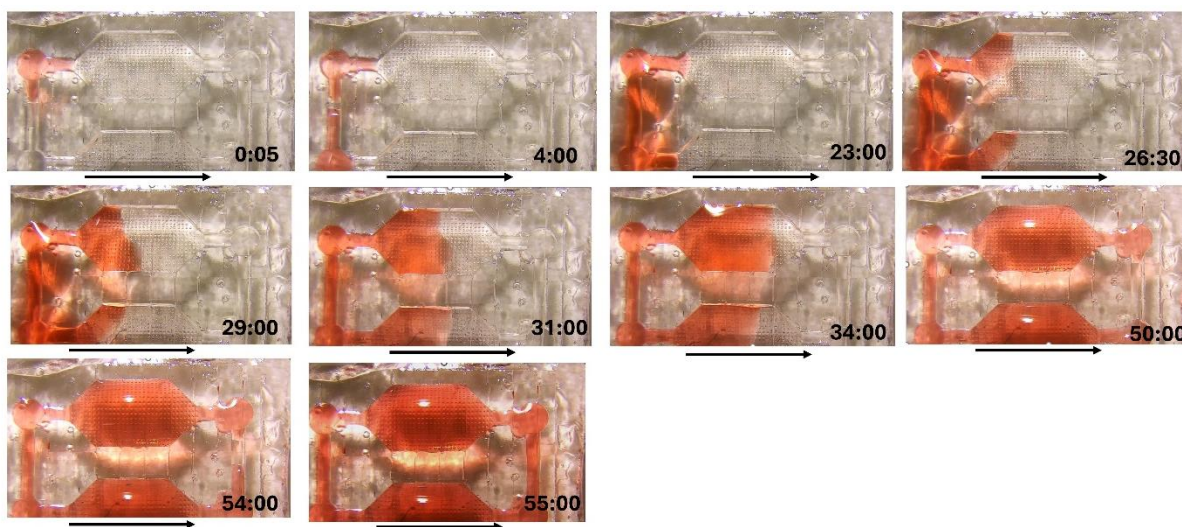


Figure 3.21: shows a time lapse of Trypan Blue and PBS through the Nanoscribe device.

Both 3D printed devices and Ostemer devices can function using capillary-driven flow. This is consistent with the contact angle results, where both clear resin (Formlabs) and Ostemer322 (Mercene Labs) have a contact angle of a hydrophilic surface. Although the downscale of Design 7b was possible and fabrication with Ostemer322 preserved all micro-scale features, the capillary-driven flow slowly than the original device with posts (50 x 20 mm). This may be attributed to the size limitations of the device, which greatly reduced the amount of liquid that could be added to the device from 2 mL (original device) to 20 μL (Nanoscribe device). Furthermore, the diameter

of the inlet of the Nanoscribe device is smaller than the diameter of a 10 μ L pipette tip. This poses a challenge to adding liquid to the inlet of the Nanoscribe device.

II. Additional fluid flow studies

To further visualize the flow within Ostemer devices of design 7a and 7b, studies were conducted with Dynabeads and fluorescence microspheres. Dynabeads M-280 (ThermoFisher) were diluted in PBS at a 1:10 (Dynabead:PBS) ratio for Dynabead experiments. Dynabeads circulated through the chamber of the device without posts for 1 minute. **Figure 3.22** shows time lapse pictures of the Dynabead fluid flow experiment.

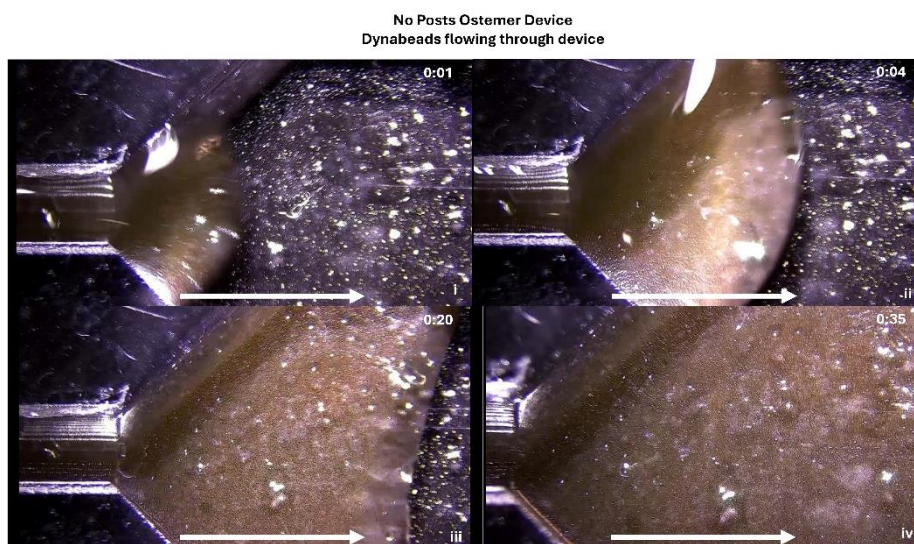


Figure 3.22: Time lapse of Dynabeads flowing through a no posts Ostemer device. Original video captured using a stereomicroscope.

Fluoro-Max Red Fluorescent Polymer Microspheres (ThermoFisher) were diluted in PBS at a 1:50 ratio for devices with posts (DWP), device without posts (DWoP), and Nanoscribe devices to avoid autofluorescence of the Ostemer material. One area of the device was recorded, due to the overall size dimensions of the devices. A total time lapse time of 10 minutes was conducted on each device, where all three devices maintained microsphere movement in their

respective chambers. **Figures 3.23-3.25** show the time lapse videos with fluorescent microspheres over the course of 1 minute for visualization.

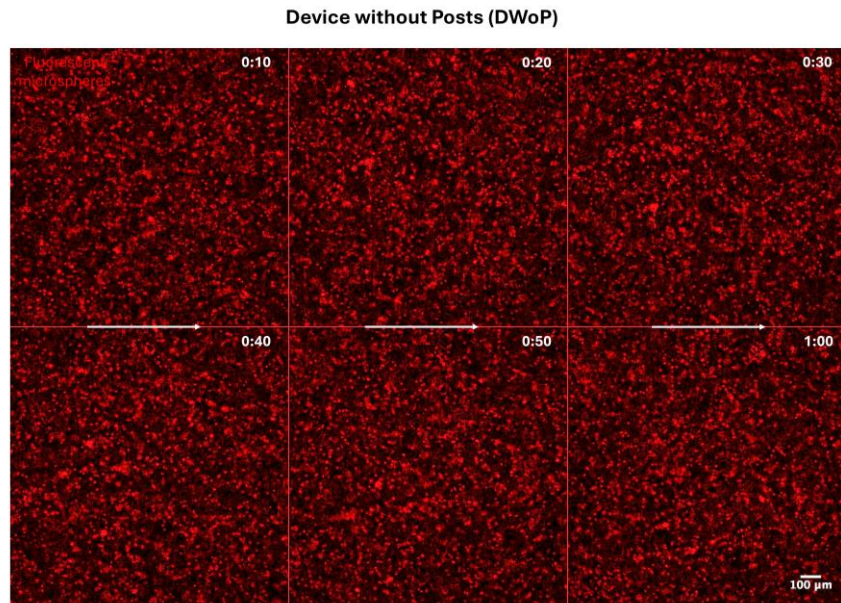


Figure 3.23: Time lapse of red fluorescent beads flowing through a device without posts Ostemer device. Original video captured using a 3D Leica fluorescence microscope.

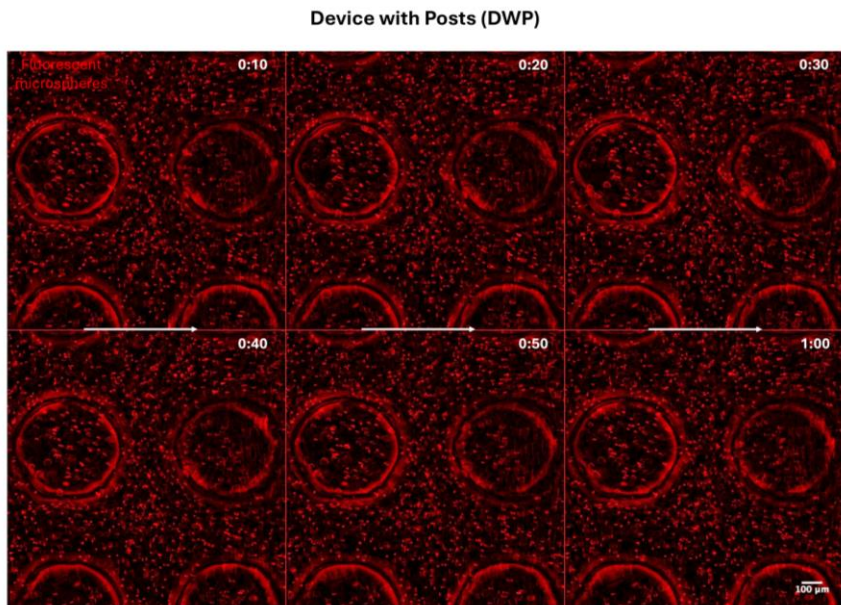


Figure 3.24: Time lapse of red fluorescent beads flowing through a device with posts Ostemer device. Original video captured using a 3D Leica fluorescence microscope.

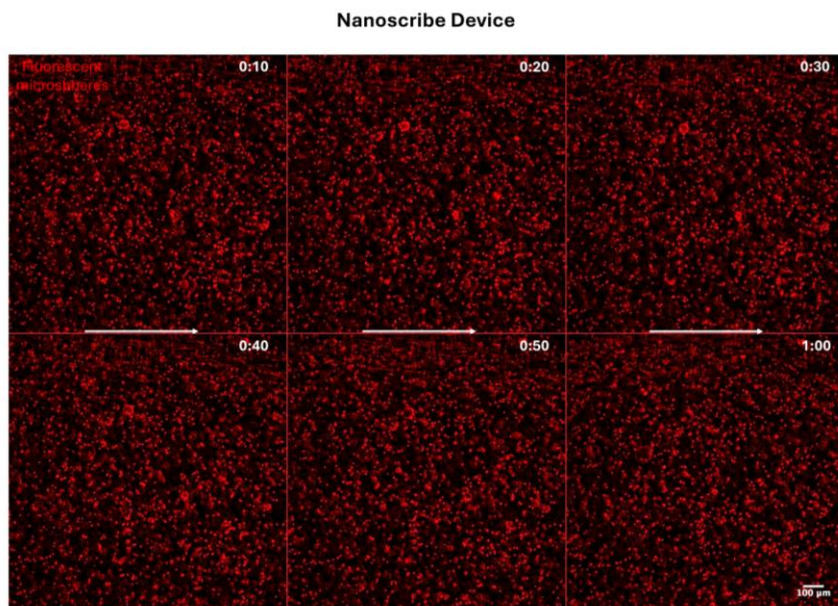


Figure 3.25: Time lapse of red fluorescent beads flowing through a Nanoscribe device. Original video captured using a 3D Leica fluorescence microscope.

Additional studies with colored liquid demonstrated that there is continuous internal movement and mixing of the liquids after addition into the device (**Figure 3.26**). This supports the findings of the continuous flow of fluorescent microbeads within the device.

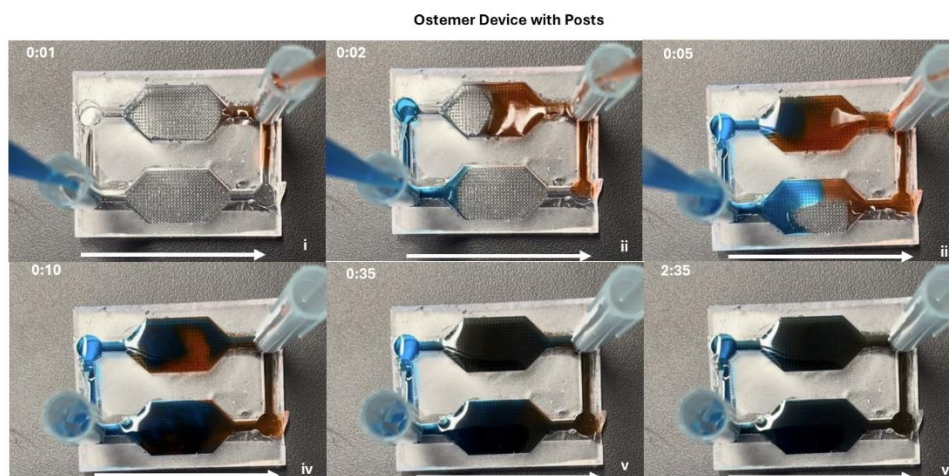


Figure 3.26: Time lapse of mixing of colored fluids to demonstrate continuous movement of liquid.

3.6 DISCUSSION AND CONCLUSIONS

After several design iterations and fluid flow experiments, a capillary-driven microfluidic device was designed based on the concepts of capillary pressure and its fabrication through 3D SLA printing and clear polymer casting. The final microfluidic device designs chosen were design 6 and 7 based on the fabrication methods and capillary-driven flow. The microfluidic device demonstrated a hydrophilic surface that supports self-driven flow when liquid is added to the surface. The design iteration and prototyping phases for initial microfluidic devices had a quick turnaround time when combined with the capabilities of the 3D SLA printer. Although, the SLA resin was not clear when placed on a microscope, the concepts of 3D printing master microfluidic devices and implementing a 3D printed mold for polymer casting were beneficial to the overall project. The implementation of a PDMS mold for polymer casting increased the workflow for device production. FEA simulations to validate fluid flow of all device designs, further demonstrated designs 6 and 7 were the most suited for potential capillary-driven flow, in agreement with Trypan Blue and PBS fluid flow experiments, where flow continued to move through the device. Contact angle studies of clear resin (Formlabs), IP-Q resin (Nanoscribe), and Ostemer322 all resulted in a contact angle less than of 90° , indicating a hydrophilic surface, capable of capillary action and capillary-driven flow in devices fabricated with these materials. When comparing velocities between devices without microposts (DWoP) and with posts (DWPG), DWPG had a faster velocity (1.87 mm/s), where the microposts helped propel fluid flow forward. Both DWoP and DWPG, presented capillary-driven flow and have the potential to serve as platforms for 3D tissue culture.

Chapter 4

Aim 2 – Optimization and development of 3D cardiovascular and cancer tissue models within the microfluidic device to study cell organization and function.

Part of the work presented in Chapter 4 was peer-reviewed and published in published in Esparza, Aibhlin, et al. "Development of in vitro cardiovascular tissue models within capillary circuit microfluidic devices fabricated with 3D stereolithography printing." SN Applied Sciences 5.9 (2023): 240.⁴³ For this reason, some of the information and images displayed in this chapter are based off the article referenced above. This chapter discusses Specific Aim 2.

4.1 AIM OVERVIEW

Specific Aim 2: Optimization and development of 3D cardiovascular and cancer tissue models within the microfluidic device to study cell organization and function.

Goal: Engineer 3D cardiovascular and cancer tissues within self-driven microfluidic device for analysis of cell orientation, alignment and structure.

Hypothesis: The interaction between the 3D tissue models (cardiovascular and cancer, respectively) and the microposts will demonstrate changes in morphology and cellular alignment.

Rationale: The integration of biophysical stimuli as microposts will guide cellular organization.

Aim 2.1: Development of 3D cardiovascular tissue model culture within microfluidic device.

Aim 2.2: Development of 3D cancer tissue model within downscaled Nanoscribe microfluidic device.

4.2 ABSTRACT

Cardiovascular diseases are difficult to study due to the lack of physiologically-relevant 3D in vitro models. The combination of 3D in vitro models with microfluidic devices can provide better platforms to study cell morphology, cell behavior, and cellular processes in greater detail.

Additionally, microfluidic devices may be inexpensive to fabricate and provide a controlled and reproducible way to quantify or evaluate changes in biochemical or physical stimuli. In this chapter, the development and analysis of 3D cardiovascular and cancer tissue models retained with capillary-circuit microfluidic devices will be explained. The tissue models actively changed their cell morphology and alignment in response to the microposts within the chambers of the microfluidic devices. The cardiovascular tissue models were developed using human umbilical vein endothelial cells (HUVECs) and human AC16 cardiomyocytes in an extracellular matrix (gelatin-alginate or fibrin hydrogel), which were loaded into the microfluidic device. Similarly, the cancer tissue models were developed using patient derived xenograft (PDX) cells and SKBR3 cells in a collagen hydrogel, which were loaded into the Nanoscribe device, the downscaled device of the capillary-circuit device with posts. The cardiovascular tissue models were analyzed with fluorescence microscopy and quantified for cell orientation and network length, where HUVEC and AC16 models demonstrated morphological differences and preferred cell alignment. Lastly, a Python based script was adapted to further quantify fluorescence images, including cell count and cell diameter, is validated to determine its potential to serve as a tool for researchers.

4.3 INTRODUCTION

Cardiovascular diseases (CVDs) and cancer are the leading causes of death worldwide but remain as a challenge to study due to the limited availability of physiologically-relevant in vitro models.^{11-13,70} Two-dimensional and animal models have been used to study cardiovascular and cancer biochemical and physiological processes, however, there are species differences between these models, including physiology, biochemical signaling, and gene expression.^{16,17,71,72} The integration of specific cell lineages and extracellular matrix (ECM) into tissue models within microfluidic devices provides a controlled, inexpensive, and reproducible system for evaluation

and quantification of cellular processes in the presence of biochemical or physical stimuli.^{17,27–29,44} Specifically, incorporating cardiovascular and cancer cells into microfluidic devices produces a novel and physiologically-relevant system to study cellular processes and mechanisms of these tissues *in vitro*.^{73–77}

Current 3D cardiovascular and cancer tissue models incorporate several types of cells, including human lineage cells and human induced pluripotent stem cells (hiPSCs).^{12,25,26,78–80} These models need microenvironments that will recapitulate the cellular microenvironment, including fluid flow and biophysical stimuli to guide cellular organization.^{12,81,82}

Microfluidic devices can be designed and tailored to cellular microenvironments customized or specific cell types or tissues. Fabrication methods for microfluidic devices include 3D printing, photolithography, and polymer casting, to name a few. Several research studies have been conducted microfluidic devices with various fabrication techniques, including 3D printing and photolithography, to study specific cellular interactions.

Moreno-Rivas et. al 3D printed microfluidic devices using stereolithography (SLA) printing with three different types of resin (Clear, High Temp, and Dental Resin LT).⁸³ The devices were printed using a Form2 Formlabs 3D printer, surface treated with Poly-D-Lysine, and subjected to a 5-day study with HeLa cells to evaluate cell viability. The study revealed Clear and High Temp resins were best for consistent and reproducible prints, although, the High Temp resin influenced the cell viability. This effect was not observed in Dental Resin LT or Clear resin. A long-term study would enhance the findings of this study and provide more information for the biocompatibility of each resin for cell studies.

Kurokawa et. al investigated the vascular formation of human induced pluripotent stem cell derived endothelial cells (hiPSC-ECs) within 3D microfluidic devices.⁸⁴ The microfluidic

devices were fabricated using soft lithography and replica molding. Prior to cell loading, the devices were coated with fibronectin. hiPSCs were differentiated into endothelial cells and then cocultured with fibroblasts with a fibrinogen hydrogel to study vascular network formation. After 14 days, network formation was observed and with the addition of a small molecule (TGF-B), the networks were responsive. This study demonstrates vascular networks can be created within microfluidic devices and studied in detail.

Furthermore, a method for fabricating a capillary-circuit microfluidic device using 3D printing and polymer casting with Ostemer322 has been published, combining two fabrication techniques.⁴³ This novel method allows for the fabrication of capillary-circuit microfluidic devices and their application in cardiovascular and cancer cell studies. Here, the optimization and development of cardiovascular and cancer tissue models within the microfluidic device will be discussed.

4.4 MATERIALS AND METHODS

4.4.1 Device fabrication

1. 3D SLA printing of microfluidic devices

Three microfluidic devices (design 6a-c) were designed with a single chamber and the following conditions: no posts, grid arrangement microposts, and staggered formation microposts within the chamber. This set of devices was designed with the intent to study if micropost formation affected cell morphology or alignment of the cells. This set of 3 devices were 3D printed using the Form3B SLA printer, post-processed according to the clear V4 resin specifications, and sterilized prior to any cell work. Additional details of the 3D printing process are discussed in Chapter 3 (Aim 1).

II. Polymer casting with Ostemer322

Furthermore, the capillary-circuit microfluidic devices (design 7a and b) were printed with the Form3B SLA printer, post-processed, and prepared for PDMS mold fabrication. The PDMS molds were then used for polymer casting of Ostemer322 to fabricate the final devices. This set of devices were used for the majority of the experiments discussed in this section and identified by the following names: Nanoscribe (downscaled device), device with posts (DWP, 50 x 40 mm), or device without posts (DWPoP). Specific steps outlining this process are discussed in Chapter 3 (Aim 1).

4.4.2 3D cardiovascular tissue model development

I. HUVEC culture and dissociation

HUVECs (ATCC, CRL-1730) between passages 4–6 were used to develop the vascular tissue model (VTM). HUVECs were cultured on 6-well plates coated with 0.2% Gelatin Type B (Sigma) with EGM-2 media (Lonza). HUVECs were passaged every 2–3 days or at 80% confluency. HUVECs were dissociated using Trypsin (0.25% Corning). Trypsin was neutralized with addition of EGM-2 and the cell suspension was centrifuged at 1300 RPM for 3 min at 23 °C. Supernatant was aspirated and resuspended in 500 µL fresh EGM-2. The cell count was obtained using a hemocytometer.

II. AC16 culture and dissociation

AC16 human cardiomyocytes cell line (SCC109, EMD Millipore, MA) between passages 4–6 were used to develop the cardiac tissue model (CTM). AC16 were cultured in T75 flasks maintained with Dulbecco's Modified Eagle Medium (DMEM/F12, Sigma) supplemented with 2 mM L-glutamine (EMD Millipore), 12.5% fetal bovine serum (FBS) (EMD Millipore), and 1 × penicillin–streptomycin solution (EMD Millipore). At 80% confluency, AC16s were

dissociated using Trypsin (0.25% Corning). Trypsin neutralized by adding DMEM media with its supplements listed above. The cell suspension was centrifuged to obtain the cell pellet. The cells were resuspended in 500 uL of media and then counted using a hemocytometer.

III. Gelatin-alginate hydrogel formation and loading into 3D printed microfluidic devices

A 2% (w/v) gelatin and 3% (w/v) alginate hydrogel was used to study the effect of micropost arrangement on HUVECs and AC16 cells. Gelatin Type A (MP) and alginate (Alginic Acid Sodium Salt, Medium Viscosity, mpbio), were measured and added to 10 mL of PBS. The solution was vortexed in 1–2-minute intervals. The hydrogel mixture was then manually mixed using a sterile spatula and vortexed for an additional 2 minutes. The hydrogel was placed into a bead bath at 37°C for 1-2 hours to obtain the desired viscosity.

HUVECs and AC16 cells were dissociated, and the cell pellet was resuspended in 500 uL of media. HUVECs (500,000 cells/mL) and AC16 cells (500,000 cells/mL) were added into the gelatin-alginate hydrogel, separately, and then loaded into the chambers of each single chamber 3D printed device (no posts, grid posts, and staggered posts). The 3D printed devices were printed one day prior to experiments and sterilized by submerging in 70% ethanol for 15 minutes and air dried. The hydrogels were crosslinked with CaCl₂ (100 mM) for 5-7 minutes. The excess CaCl₂ was removed, and the cell-hydrogels were supplemented with their respective media (EGM-2 for HUVECs and DMEM for AC16 cells). Cell media was changed every other day for 5 days.

IV. Fibrin hydrogel formation loading into microfluidic device and Transwell inserts

A fibrin hydrogel was used to develop the cardiovascular tissues (CTM and VTM) with human umbilical vein endothelial cells (HUVECs) and human AC16 cardiomyocytes. The fibrinogen solution was prepared by dissolving 75% clottable fibrinogen (Fibrinogen from bovine

plasma, Sigma Aldrich) in thrombin bovine (Thrombin, Bovine, Sigma Aldrich) in 1% bovine serum albumin (BSA, Fisher Bioreagents). Fibrinogen (25 mg) was mixed in sterile PBS warmed to 37°C. HUVECs and AC16 cells were dissociated, and the cell pellet was resuspended in their respective media. The cells were collected at 500,000 cells/ mL (HUVECs) and 1×10^6 cells/mL (AC16s). The cells were added into the fibrinogen and PBS mixture separately, for the formation of individual hydrogels.

Capillary-circuit microfluidic devices (device with posts, DWP, and device without posts, DWoP) were fabricated with Ostemer322 at least 1 day prior to cell encapsulation into the fibrin hydrogel. Devices were sterilized in 70% ethanol for 15 minutes and allowed to completely dry before addition of the cell-hydrogel. When devices were sterilized and dry, 1000 μ L of the cell-fibrinogen-PBS mixture was collected and slowly released into the tissue culture chambers of the microfluidic device. To crosslink the hydrogel, 150 μ L of thrombin in 1% BSA was added directly to the hydrogel. The cell-hydrogel in microfluidic devices were incubated for 10–15 min at 37 °C and 5% CO₂. The cells were supplemented with 1000 μ L of media (EGM-2 for HUVECs and DMEM for AC16s) after cross linking. The microfluidic devices were placed into a 100 mm petri dish (Fisherbrand Petri Dish, 100 mm) and then cultured for 1, 3, and 5 days.

For control conditions, Transwell inserts (12 mm) for 12 well multi-well plate were used as a control in this study to better assess cell morphology and behavior without exposure to Ostemer322 and microenvironment biophysical cues (microposts). The cell-fibrinogen mixture (700 μ L) was added to each Transwell insert and crosslinked with 150 μ L of Thrombin in 1% BSA. The multi-well plate was incubated for 10–15 min at 37 °C and 5% CO₂. After incubation, maintenance media (500 μ L) was added.

For maintenance of VTM (HUVECs encapsulated within fibrin hydrogel) and CTM (AC16 cells encapsulated within fibrin hydrogel), spent media was removed from the microfluidic devices with a pipette tip 24 h after initial loading and supplemented with media every other day (day 3 and day 5).

4.4.3 Doxorubicin studies with 3D coculture of HUVECs and AC16 cells within capillary circuit microfluidic device

HUVECs and AC16 cells were grown and maintained separately until ~80% confluent. Both cell types were dissociated using Trypsin and centrifuged to obtain the cell pellet. After counting both cell pellets, HUVECs and AC16 cells were mixed at a ratio of 3:1 (HUVECs: AC16 cells) at a density of 300,000 to 100,000 cells/mL. The cells were added into a fibrinogen mixture, which was then loaded into either the chambers of the microfluidic device with posts (DWP) or a Transwell insert (12 mm, 12 well multiwell plate). The fibrinogen hydrogel was crosslinked with thrombin solution and incubated for 10-15 minutes. The samples were cultured for 3 and 5 days to study cell behavior and alignment. Maintenance media was added every other day.

Furthermore, the additional coculture studies with HUVECs and AC16 cells were extended to include drug exposure studies with Doxorubicin (DOX, Doxorubicin Hydrochloride, TCI), a drug that plays a role in cardiomyopathy and affects endothelial cell signaling to cardiomyocytes, as well as cell survival and function.⁸⁵ DOX was reconstituted and directly dissolved in EGM-2 media, the common media between HUVECs and AC16 cells. The 3D coculture of HUVECs and AC16 cells were maintained in culture for 5 days and treated with the final concentration of 1 μ M DOX for 48 hours, for the total of a 7-day study.

4.4.4 3D cancer tissue model development

I. PDX culture and dissociation

Patient derived xenograft (PDX) cells were maintained in T75 flasks with Dulbecco's Modified Eagle's Medium (DMEM). PDX cells were passaged approximately once a week. At 80% confluency, PDX cells were dissociated with Trypsin and quenched with DMEM. The cells were counted and either used for experiments or placed back into culture. Cells were maintained at 37°C and 5% CO₂.

II. SKBR3 culture and dissociation

SKBR3 cells were maintained in T75 flasks with Dulbecco's Modified Eagle's Medium (DMEM). SKBR3 cells were passaged every 3-4 days. At ~80% confluency, SKBR3 cells were dissociated with Trypsin and quenched with DMEM. The cells were counted and either used for experiments or placed back into culture. Cells were maintained at 37°C and 5% CO₂.

III. Collagen hydrogel formation and loading into Nanoscribe devices

Collagen hydrogels of 0.2 wt% were prepared using Collagen Type I Rat Tail (100 mg, Millipore Sigma). The collagen hydrogel was prepared by mixing cold collagen (4.25 mg/mL) with 10x Phosphate Buffered Solution (PBS) and Molecular Grade Biological Water to a final concentration of 2 mg/mL. PDX and SKBR3 cells were encapsulated into separate collagen hydrogels with a density of 100,000 cells/mL. The loading volume into Nanoscribe devices is 10 µL per chamber, for a total of 20 µL. After loading the cell-hydrogel into the chambers of the Nanoscribe devices, the devices were placed in standard incubation for 10-15 minutes to allow crosslinking of the hydrogel. After this, the respective cell media was added to each device with the specific cell type. Loaded devices were cultured for 2 days within the Nanoscribe devices to determine the feasibility of using a small device.

4.4.5 Characterization with fluorescence microscopy

On either day 1, 2, 3, or 5, samples were rinsed with 1x PBS (Gibco) and fixed with 4% paraformaldehyde (PFA, ThermoFisher) for 10 min. PFA was removed and samples were rinsed with PBS twice. Samples were permeabilized with 0.1% Triton for 5 minutes and then rinsed two times with 1x PBS. Samples were then blocked with 2% Bovine Serum Albumin (BSA, Fisher Bioreagents) for 10 minutes. The 2% BSA solution was removed, and samples were stained with 1:200 primary antibodies in 2% BSA overnight at 4°C. **Table 4.1** outlines the cell type, primary antibodies, and secondary antibodies used for immunostaining. The following day, samples were rinsed twice with 1x PBS and stained with fluorescent secondary antibodies at a 1:200 ratio in 2% BSA at room temperature for 1 hour. Samples were rinsed twice with PBS and subsequently stained with Actin-stain 555 phalloidin (ActinRed 555 ReadyProbes Invitrogen) and nuclei were stained with DAPI (NucBlue Fixed Cell Stain ReadyProbes, Invitrogen) for 10 min at RT. Samples were washed with PBS once and fluorescence images were captured with a Leica Thunder Imager Live Cell and 3D Assay fluorescent microscope with a 10x or 40x objective lens (Leica Microsystems, Buffalo Grove, IL).

Table 4.1: Primary and secondary antibodies for immunostaining.

| Cell Type | Primary Antibody | Secondary Antibody |
|---------------------|---|--|
| HUVECs | CD31 Monoclonal Antibody WM59, Invitrogen | Alexa Fluor 488 goat anti-mouse secondary antibody |
| AC16 cardiomyocytes | Cardiac Troponin T Monoclonal Antibody (13-11), Invitrogen | Alexa Fluor 488 goat anti-mouse secondary antibody |
| AC16 cardiomyocytes | Monoclonal Anti- α -actinin (Sarcomeric) antibody, Sigma Aldrich | Alexa Fluor 555 goat anti-mouse secondary antibody |
| SKBR3 | Primary anti-human HER2, Biologend | Alexa Fluor 488 goat anti-mouse secondary antibody |
| PDX | EPCAM | Alexa Fluor 488 goat anti-mouse secondary antibody |

4.4.6 Computational image analysis

I. Computational fluorescence image analysis – cell orientation

Cell orientation in vascular tissue models (VTM, HUVECs in fibrin hydrogel) and cardiovascular tissue models (CTM, AC16 cells in fibrin hydrogel) samples were quantified with ImageJ OrientationJ plugin by measuring the gradient structure in fluorescence images.⁵⁹ Fluorescence images were loaded into ImageJ, evaluated using evaluated using Gaussian function, and exported into a histogram. Axis ranges were adjusted to include 0° to 90° preferred orientation in the images. Angles begin at 0° in the east direction and the orientation is measured counterclockwise (**Figure 4.1**).

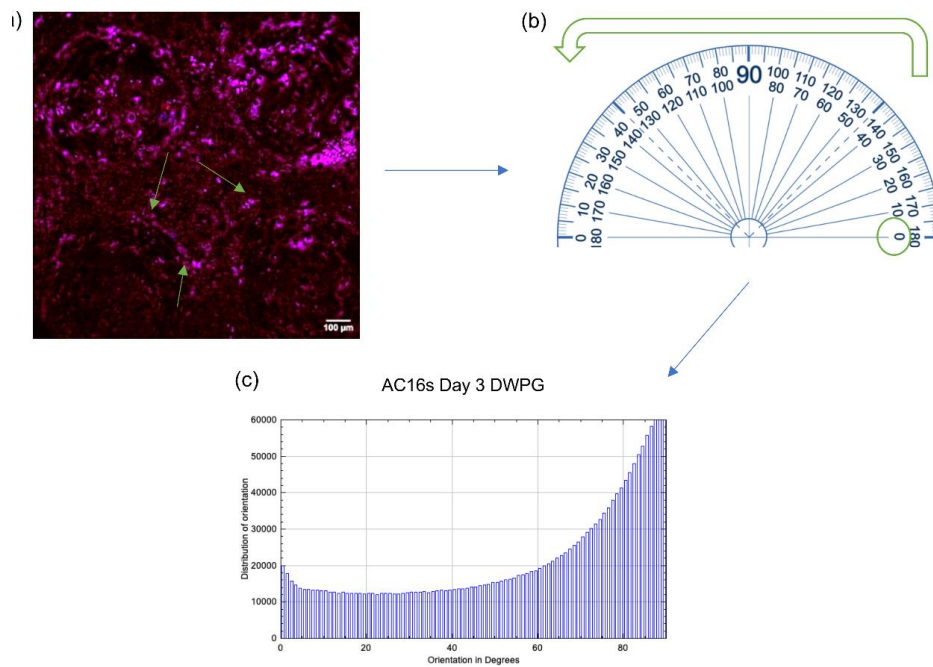


Figure 4.1: referred orientation is measured with OrientationJ plugin in ImageJ. The orientation is measured from z-stack fluorescence images (a) with reference to the 0° on the right side of the image (as indicated in (b)) and measured counterclockwise. Following the orientation analysis, the orientation histogram is formed (c).

II. Computational fluorescence image analysis – network formation

VTM (HUVECs within fibrin hydrogel) and CTM (AC16 cells within fibrin hydrogel) samples were evaluated for tube formation and quantified using ImageJ Angiogenesis Analyzer plugin, which measures the tube length and diameter in fluorescence images.^{86,87} This plugin was also used to measure total network length of CTM, AC16 cells within fibrin hydrogel) to quantify cell behaviors, including cell elongation. F-actin and DAPI channels (red and blue channels, respectively) were merged to form 1 image. This image was then changed to a binary image using ImageJ and the Angiogenesis Analysis plugin measured the binary image.

4.4.7 Automated Image Analysis Python Script (AIAPS) Validation

The combined efforts of researchers from the University of Texas at El Paso within the Biomedical Engineering and Computer Science departments modified an original code (Automated Image Analysis Python Script, AIAPS respectively) developed from the Southwest Research Institute (SWRI). The script was modified to fit the needs of our lab, including image analysis. This script is unique in that it takes a JPEG image with one or more colors, measures the cell diameter and/or cell count of the image, and produces a modified image with identified cells outlined and an .CSV sheet with the image label and the data measured.

Due to the modifications to the original script, the AIAPS needed to be validated and compared to other standard methods of cell count or cell measurement, including ImageJ/Fiji, an open and free source image processing package. Images of different microbead densities (FluoroMax Green Fluorescent Polymer Microspheres, ThermoFisher), were acquired and processed through the AIAPS Script and ImageJ (Fiji, National Institutes of Health, Version 1.54F). Low density (LD), medium density (MD), and high density (HD) microbeads were prepared using the fluorescent microspheres and diluting in PBS for final microbead concentrations of 3 beads/ μ l, 50

beads/ μl and 100 beads/ μl , respectively. Different densities were used to determine the accuracy of the algorithm when there is a high confluency of cells or particles in an image. The same set of images were analyzed in ImageJ/Fiji using the “Analyze Particles” function, as well as, in the AIAPS Script. The image sets consisted of $n=3$ image replicates per group and $N=5$ images per replicate. All outputs were saved, and values were saved as .CSV files for statistical analysis.

4.4.8 Statistical Analysis

All quantitative measurements were performed at least in triplicate samples and values are expressed as mean \pm standard deviation (SD). One- or Two-way ANOVA with post-hoc Tukey tests were used to compare treatment groups and $p < 0.05$ was used to assess statistical significance using GraphPad Prism Software.⁸⁸

4.5 RESULTS AND DISCUSSION

4.5.1 Fluorescence microscopy of single chamber 3D printed devices

After conducting a 5-day study within 3D printed devices with microfluidic devices with no microposts and microposts, there was a difference in HUVEC and AC16 cell structure. **Figure 4.2** displays the microfluidic devices used for this study, which include no microposts, grid formation microposts, and staggered microposts.

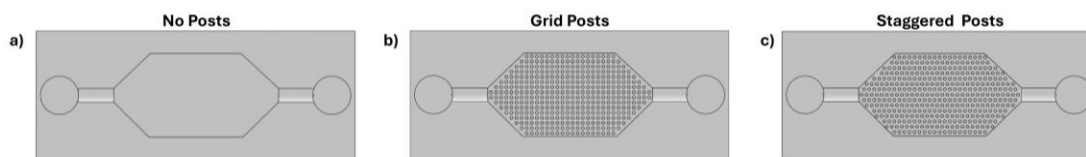


Figure 4.2: Schematic of 3D printed microfluidic devices with no microposts (a), grid formation microposts (b), and staggered formation microposts (c).

Although Chapter 3 discusses the development and optimization of a fabrication protocol to produce clear devices for visibility through a device, this study demonstrated HUVECs and AC16 cells can be cultured within 3D printed devices for at least 5 days with minimal effects to

the cells. Furthermore, after fixing and staining the 3D cell-hydrogel samples, the samples could easily be removed from the 3D printed device and fluorescently imaged. **Figure 4.3** shows the fluorescence images acquired from HUVEC and AC16 samples within each 3D printed microfluidic device. By day 5, both HUVECs and AC16 cells spread and became elongated in devices with posts, while cells in devices without posts showed random positioning. This quick study demonstrated the implementation of microposts in the microfluidic device influenced HUVEC and AC16 cell structure and alignment.

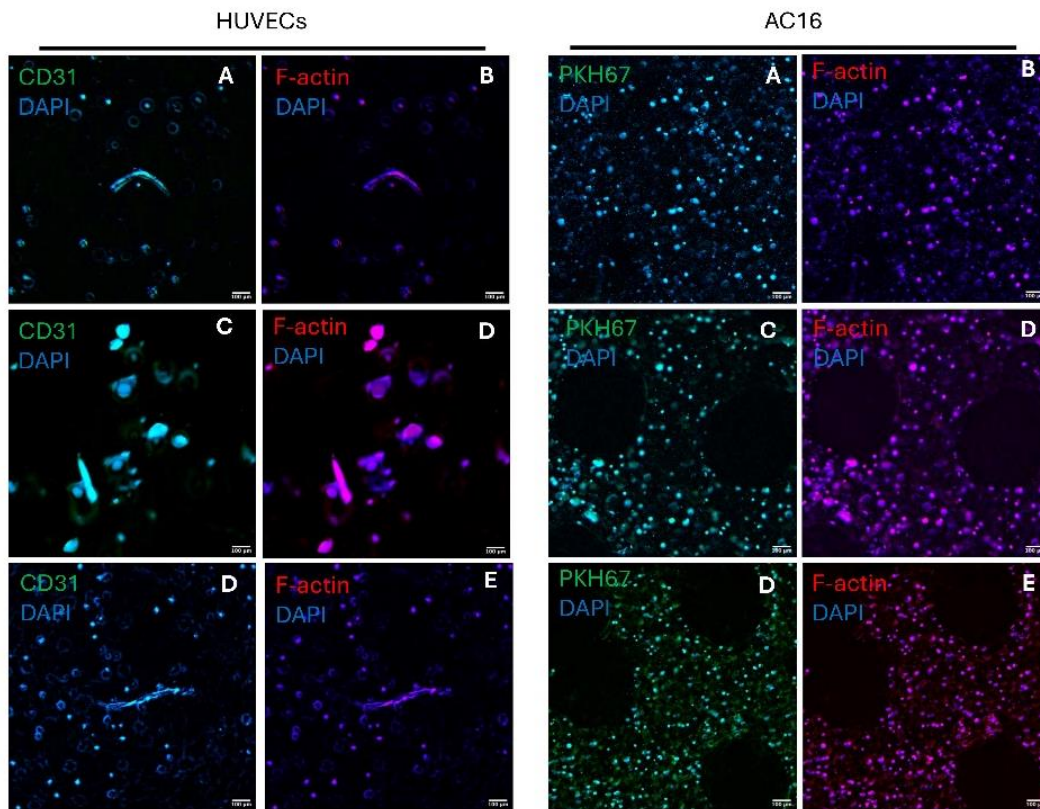


Figure 4.3: Fluorescence images acquired on day 5 from HUVEC and AC16 samples of 3D printed devices with no microposts (a-b), grid microposts (c-d), and staggered microposts (e-f).

4.5.2 Cardiovascular and Vascular Tissue Models within capillary-circuit microfluidic device

I. Fluorescence microscopy

Figures 4.4 and **4.5** shows fluorescence microscopy images of HUVECs and AC16s encapsulated within a fibrin hydrogel and cultured in either Transwell inserts (12 mm, control) and capillary-circuit devices (DWP and DWP) fabricated using Ostemer322. These studies were conducted over 1, 3, and 5 days. HUVECs in Transwell inserts show capillary-like tube formations at all time points, while HUVECs in devices without posts (DWP) show capillary-like tube formations that are curved and disjointed (**Figure 4.4**). In devices with posts (DWP), HUVECs form elongated, continuous capillary-like tubes with circular structural orientation that appear to be guided by the device microposts. Capillary-like lumen formation was also demonstrated in each microenvironment condition (white arrows).

Figure 4.5 shows fluorescence microscopy images of CTM cultured in Transwell inserts (12 mm, control) and capillary circuit devices (DWP and DWP) for day 1, 3, and 5. AC16 cells in Transwell inserts show high density cell confluency, typical in stationary 3D culture conditions. In DWP, AC16 cardiomyocytes show little to no alignment or specific orientation, which may be due to the lack of interaction between the cells and device. In DWP, AC16 cells show alignment around the microposts, demonstrated by elongated cells arranged in circular orientations at micropost locations (dashed circles).

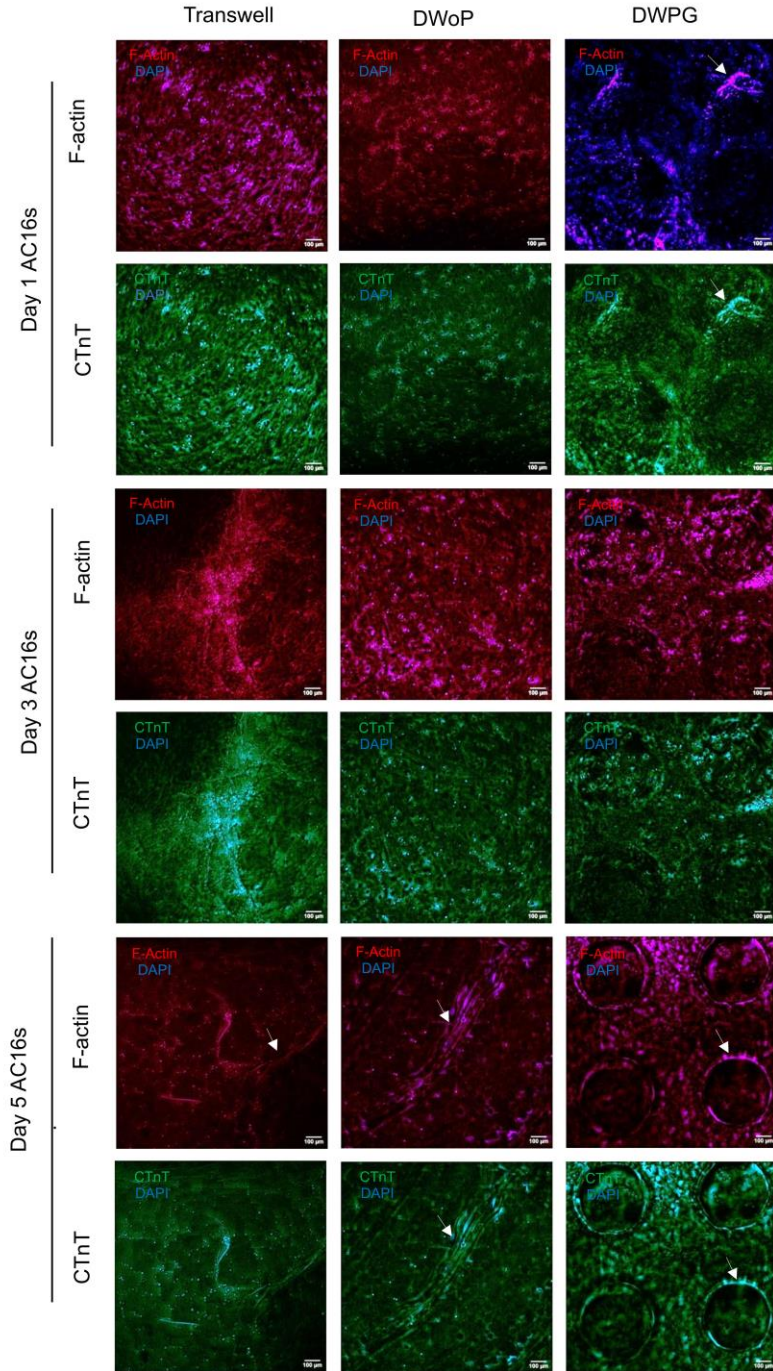


Figure 4.4: Representative 3D z-stack fluorescence images for days 1, 3, and 5 for HUVEC samples in Transwell inserts, device without posts (DWoP), and device with posts (DWP). White arrows indicate capillary-like lumen formation in each microenvironment condition.

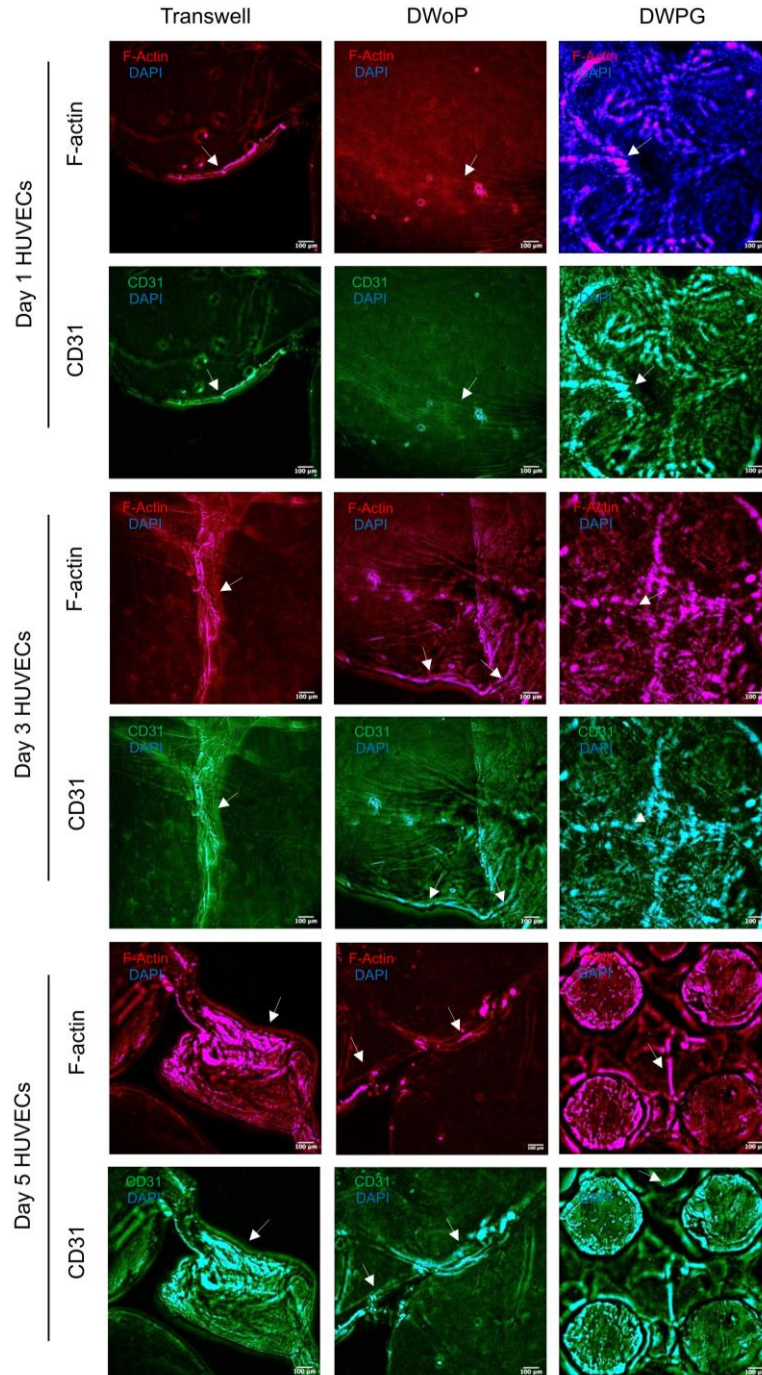


Figure 4.5: Representative 3D z-stack fluorescence images for days 1, 3, and 5 for AC16 samples in Transwell inserts, device without posts (DWoP), and device with posts (DWP). White arrows indicate capillary-like lumen formation in each microenvironment condition.

II. Cell orientation

Fluorescence images stained for F-actin cytoskeleton and nucleus visualization (Phalloidin and DAPI) from each time point and condition (cell type and culture condition) were analyzed using OrientationJ ImageJ plugin. HUVECs in the VTMs did not demonstrate any significant differences in alignment along the 0° and 90° axis (**Figure 4.6a** and **b**), this non-preferential alignment is demonstrated in the fluorescence microscopy images. In contrast, AC16 cardiomyocytes in CTMs statistically significant differences in orientation at 0° for DWPG where alignment decreased from Day 1 to Day 5 (**Figure 4.6c**) The AC16 cardiomyocytes also demonstrated statistically significant differences in orientation at 90° for DWPG on Day 5 (**Figure 4.6d**). These results demonstrate HUVECs are forming stable capillary-like networks with non-preferential orientation while AC16 cardiomyocyte structural organization is affected by physical cues in the microenvironment.

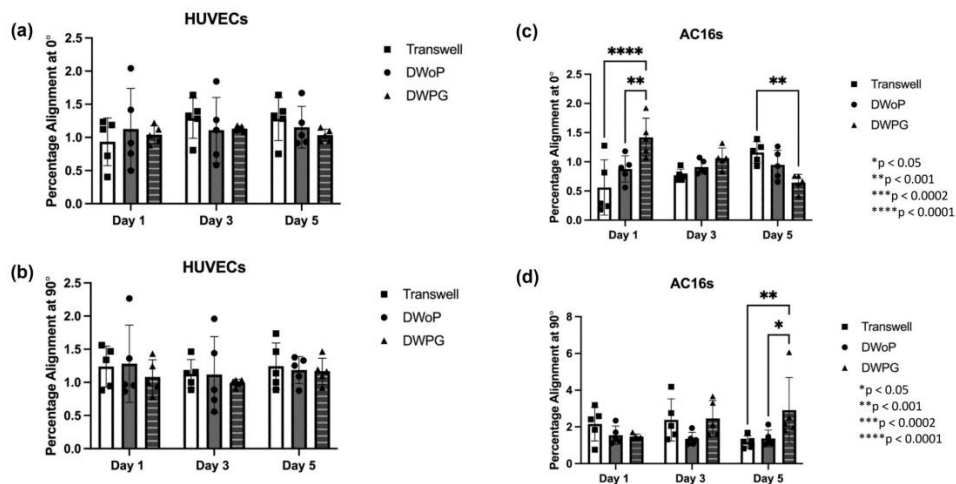


Figure 4.6: Cell percentage alignment at 0° and 90° distribution from VTM (HUVEC) and CTM (AC16) samples on day 1, 3, and 5 in Transwell, DWoP, and DWPG. (n = 5) *p < 0.05, **p < 0.002, ***p < 0.0002, ****p < 0.0001.

Overall, Day 1, 3, and 5 HUVEC Transwell samples showed different preferred orientations, ranging from 40° to 60° , whereas AC16s Transwell samples showed preferred

orientation around 75° on Day 1 and by Day 3 and 5, there was a range from 40° to 80° (**Figure 4.7**).

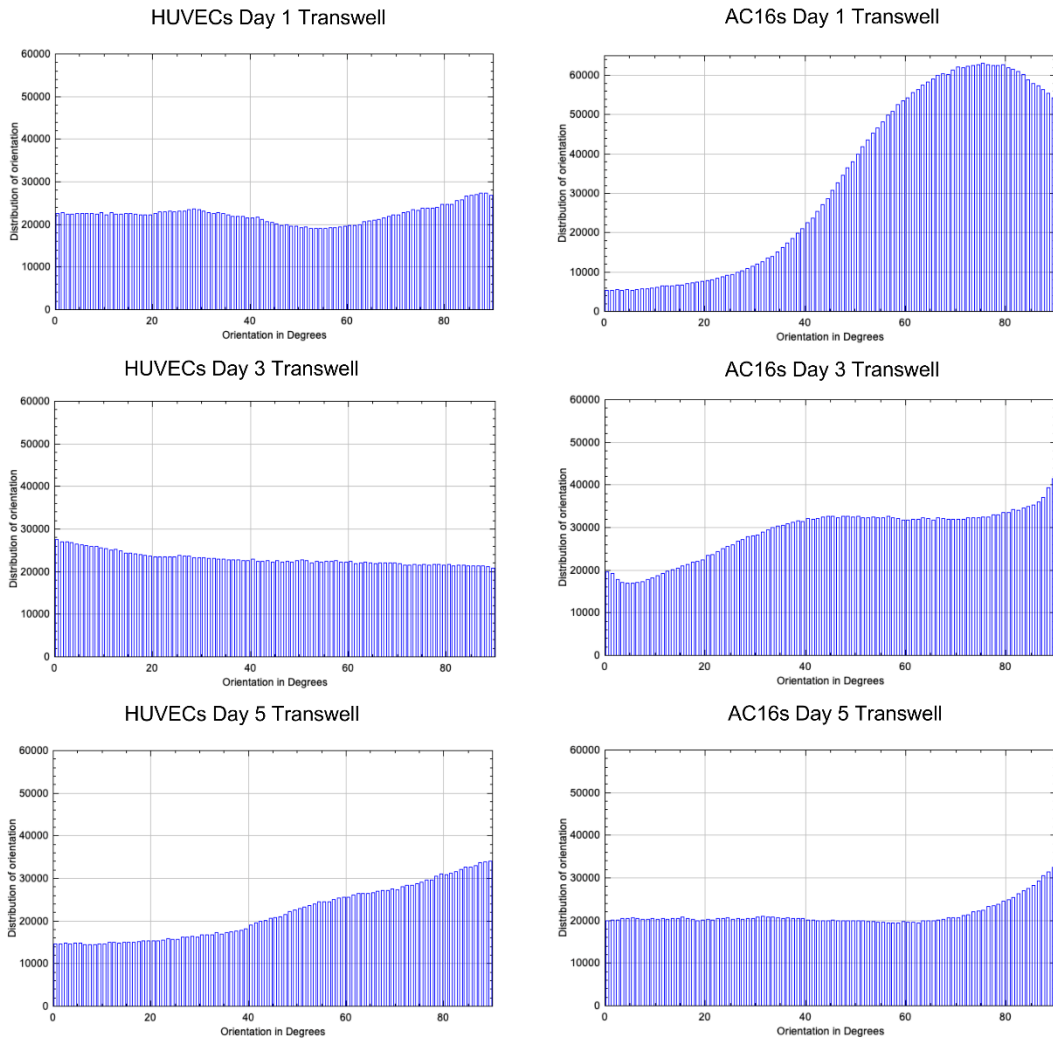


Figure 4.7: Representative cell orientation distribution graphs (OrientationJ ImageJ plugin) from VTM and CTM samples on day 1, 3, and 5 in Transwell inserts. (n=5)

Day 1 HUVECs samples in DWoP, showed a preferred orientation at 60° while Day 1 AC16s samples in DWoP demonstrated preferred orientation at 80° (**Figure 4.8**). Day 3 and Day 5 DWoP for both cell types, did not have a preferred orientation (**Figure 4.8**).

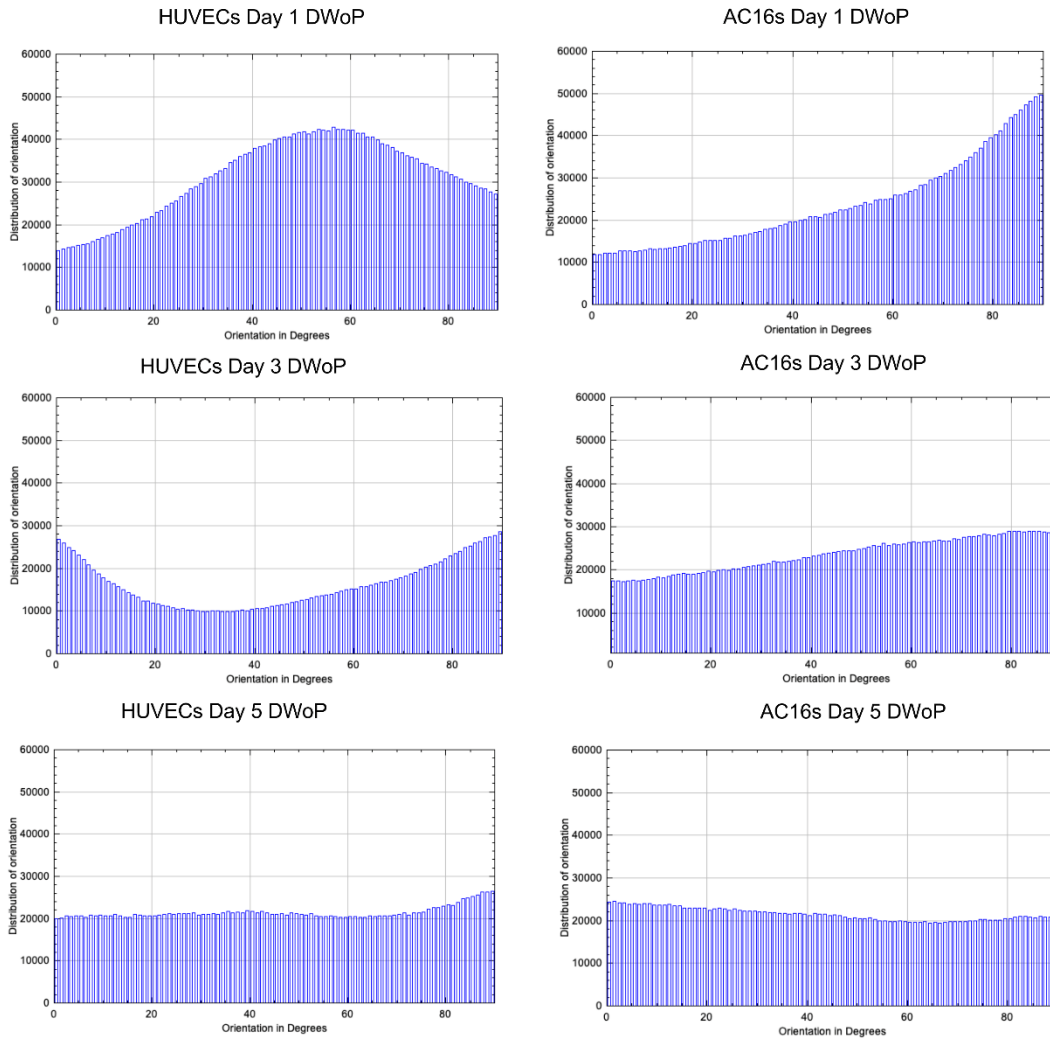


Figure 4.8: Representative cell orientation distribution graphs (OrientationJ ImageJ plugin) from VTM and CTM samples on day 1, 3, and 5 in DWoP. (n=5)

Day 1 and 3 HUVECs samples in DWPG did not have a preferred orientation (**Figure 4.9**). Day 1 AC16s DWPG did not show a preferred orientation. HUVECs Day 5 DWPG showed preferred orientation at 60°. Day 3 and 5 AC16s samples in DWPG showed preferred orientation around 90° (**Figure 4.9**). These results indicate cells are expanding their networks and orientations around the grid microposts.

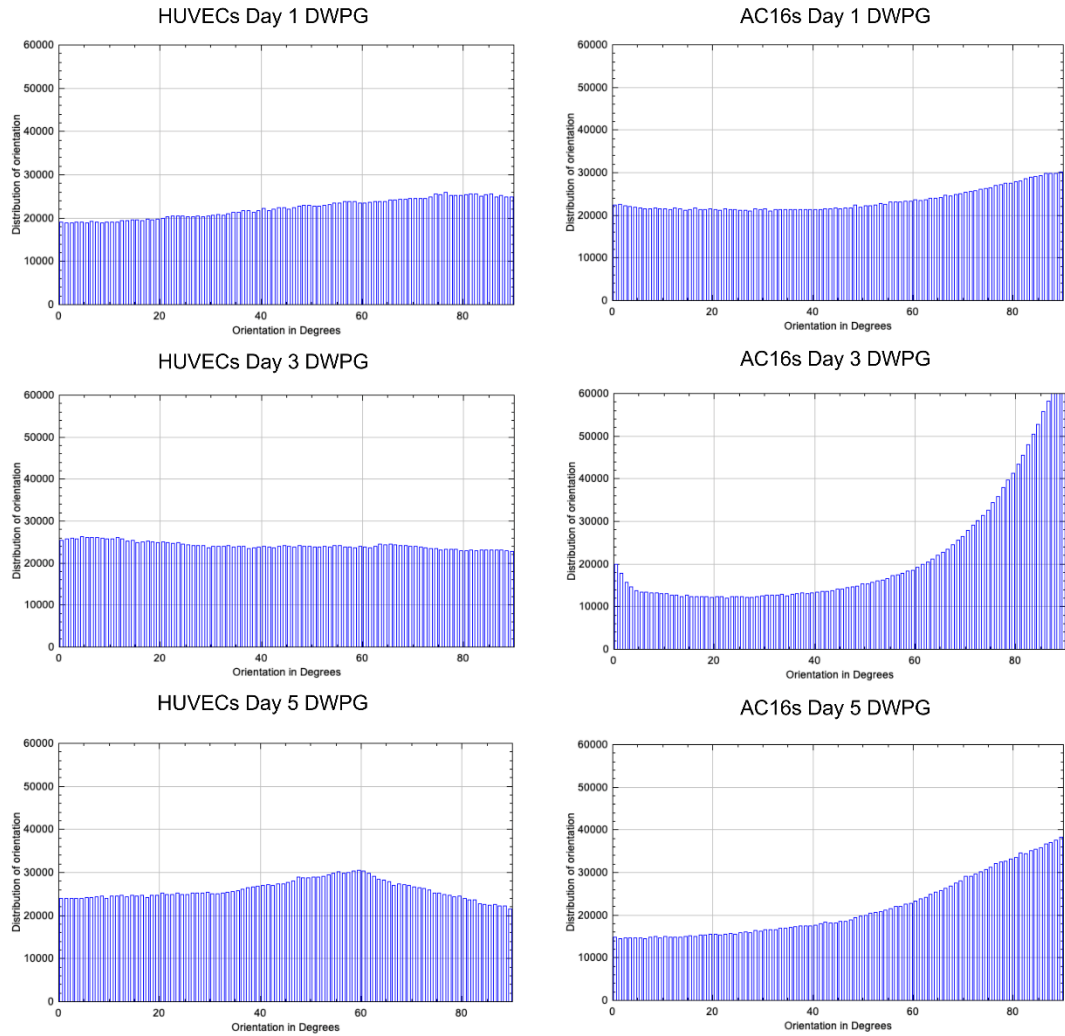


Figure 4.9: Representative cell orientation distribution graphs (OrientationJ ImageJ plugin) from VTM and CTM samples on day 1, 3, and 5 in DWP. (n=5)

III. Average network length

Average network length for day 1, 3, and 5 were quantified using ImageJ Angiogenesis Analyzer. For VTM (HUVECs) samples, there was no statistically significant difference between Transwell inserts, DWP, and DWPG. However, for CTM (AC16 cells) samples, there was a statistical significance between Day 3 DWPG and Day 5 DWPG (**Figure 4.10**).

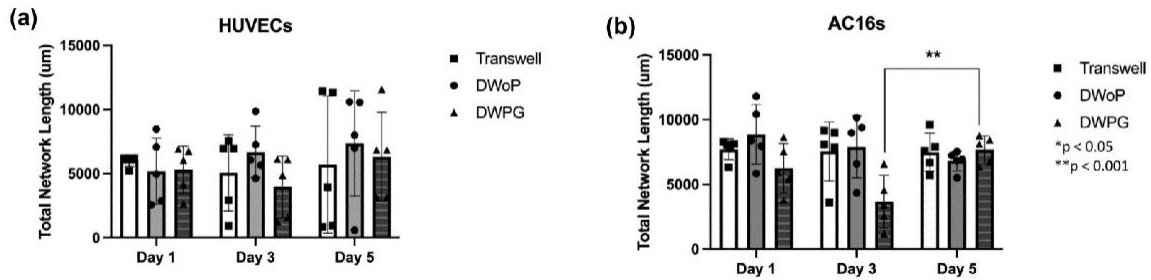


Figure 4.10: Quantification of cellular network formation within VTM (HUVECs) and CTM (AC16). Analysis of total network length in fluorescence images. (a) shows day 1, 3, and 5 data with HUVECs and (b) shows day 1, 3, and 5 data with AC16s. (n = 5) *p < 0.05, **p < 0.001.

Fluorescence images and computational analysis using ImageJ plugins demonstrated morphological differences between tissues cultured in devices without posts vs. devices with posts (DWoP vs. DWPG). In DWPG VTMs (HUVECs) displayed capillary-like tube formation with visible cell alignment, while AC16s continued to elongate around microposts by day 5 which indicated the microposts induced biophysical cues to guide cell structure and specific organization. Computational analysis of fluorescent images resulted in statistically significant differences in alignment at 0 and 90° for CTMs and total network length. Quantifying alignment at 0° displayed a statistically significant increase in preferred alignment at 0° for Day 1 CTMs DWPG. Alignment at 0° displayed a statistically significant decrease in preferred alignment at Day 5 for CTMs in DWPG. At 90 degrees, there is a statistically significant increase in preferred alignment at 90° for Day 5 CTMs in DWPG, indicating AC16s in CTMs preferred alignment toward 90° instead of 0° after a few days in culture. This suggests cardiomyocytes in the CTM are sensing the spacing between microposts in vertical and horizontal directions.

4.5.3 Doxorubicin studies with 3D coculture of HUVECs and AC16 cells within capillary circuit microfluidic device

I. Fluorescence microscopy

Figure 4.11 shows the coculture of HUVECs and AC16s within a fibrin hydrogel in Transwell inserts (12 mm) and capillary-circuit devices with posts (DWP) fabricated with Ostemer322. HUVECs and AC16s were co-stained and can be identified by their respective cell marker, CD31 for HUVECs and alpha-actinin for AC16 cells. Transwell insert conditions display random and varied cell alignment, while tissues cultured in DWP, show cell spreading, elongation, and orientation around microposts. This data is consistent with previous studies conducted with individual cell types within the same device, DWP.

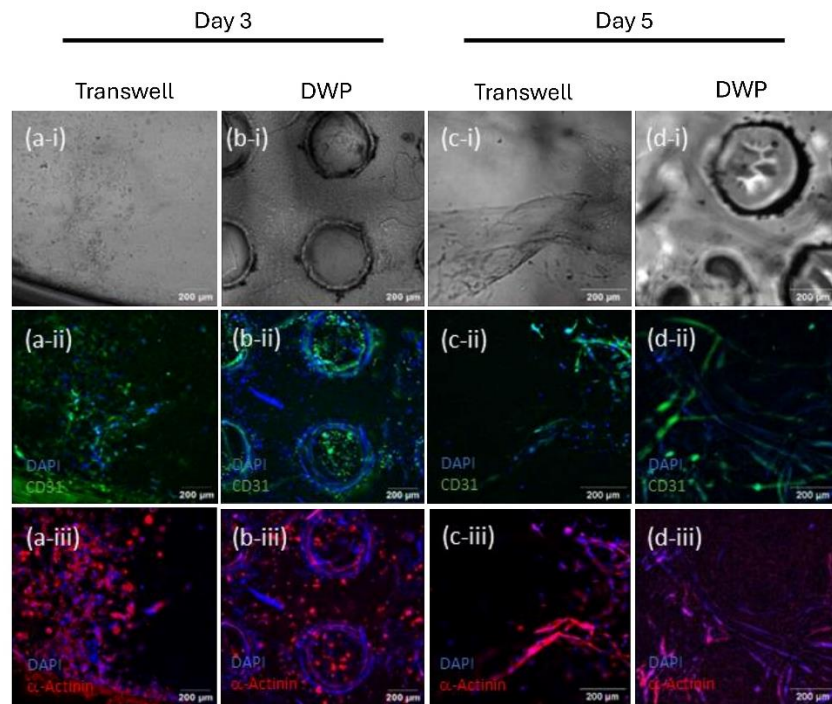


Figure 4.11: Coculture of HUVECs and AC16s within capillary-circuit microfluidic device. Images acquired for day 3 and 5 in Transwell insert (12 mm) and DWP.

II. Network formation analysis

Average network length for day 3 and 5 were quantified using ImageJ Angiogenesis Analyzer (**Figure 4.12**). Though this was a coculture study, the individual network formation for each individual cell type was evaluated. For HUVECs, there was no significant difference in network formation in Transwell insert or DWP at any time point. However, for AC16 cells, there was an increase in network formation on day 5 DWP compared to the Transwell insert. This is also consistent with data acquired on previous studies with individual cell types within the same device.

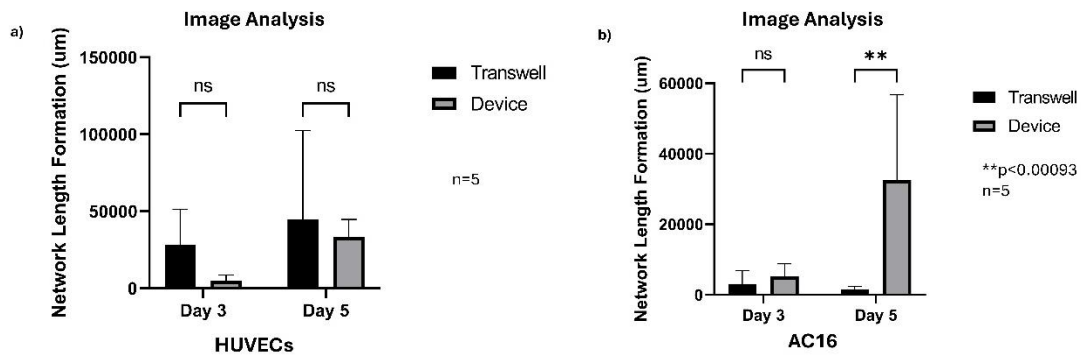


Figure 4.12: Network formation image analysis for day 3 and 5 coculture studies in Transwell inserts and DWP.

II. Doxorubicin studies with 3D coculture of HUVECs and AC16s

A drug test with Doxorubicin Hydrochloride (DOX) was conducted to assess cellular response to biochemical and/or physical stimuli. **Figure 4.13** shows phase contrast images of a coculture study with HUVECs and AC16 cells encapsulated within a fibrin hydrogel in either a Transwell insert or capillary-circuit device with posts (DWP). The samples were cultured for 5 days in normal incubation conditions and at this time point, the cells in both the Transwell insert and DWP look rounded. After addition of DOX on day 6, 24-hour exposure time, the same area was imaged, and the cells appear the same. At 48 hours post-exposure (day 7), both Transwell

insert and DWP show rounded cells. This experiment was repeated 2 more times and the cocultured cells had the same rounded morphology at all three time points (pre-exposure, 24 hours post-exposure, and 48 hours post-exposure). This may be attributed to the variability in the crosslinking of the fibrin hydrogel, high passage of the cells used in this experiment (HUVECs passages 6-9 and AC16 passages 8-10). Although this drug study was inconclusive, it demonstrated the need to use biomaterials that have less batch-to-batch variability and will provide the cells an environment to grow.

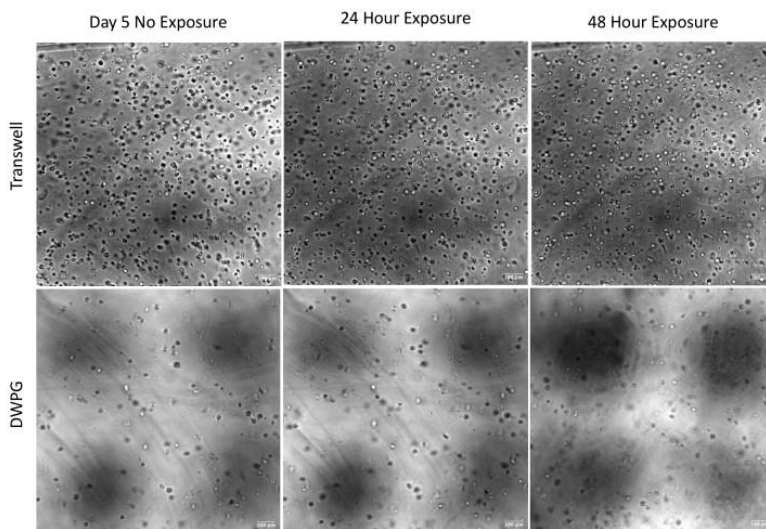


Figure 4.13: Phase contrast images of HUVEC and AC16 coculture study for 5 days followed by DOX exposure for 2 days.

4.5.4 3D cancer tissue model

SKBR3 and PDX cells were encapsulated into collagen hydrogels, placed into separate Nanoscribe devices, and cultured for 2 days. This was to determine the feasibility of maintaining a small scale device, including cell survival, hydrogel degradation, and cell behavior. **Figure 4.14** shows fluorescence images of 3D PDX and SKBR3 models within the Nanoscribe microfluidic device. Both cell types maintained their respective cell morphology in 3D culture (within a

collagen hydrogel) and in the Nanoscribe device. This suggests the cells did not experience any detrimental effects or major changes when cultured in the Nanoscribe device.

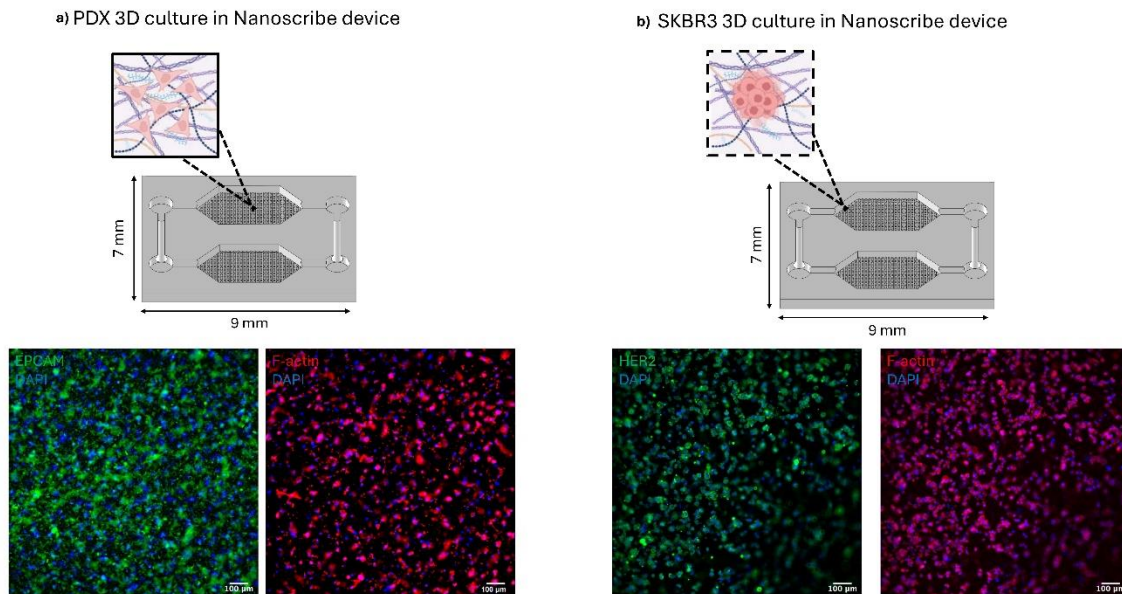


Figure 4.14: shows PDX and SKBR3 3D culture schematic in Nanoscribe devices and representative fluorescence images.

4.5.5 AIAPS Script Validation

Previously, we found some difficulties using ImageJ to analyze images taken by fluorescence microscopy, therefore an algorithm using Python coding to analyze fluorescent images was developed with the help of several researchers at the University of Texas at El Paso and the Southwest Research Institute (SWRI).

First, when comparing the original fluorescence image to the counted output image, ImageJ may count a single particle more than once and multiple particles in the image. This makes it difficult for the user to visually compare the original image to the output. In addition, ImageJ requires the image to be changed to an 8-bit color Image. After this, the threshold of the image must be changed to produce a black-and-white image. In comparison, the algorithm uses the images as they are, no change is needed. Also, the algorithm can analyze multiple images at once.

Furthermore, the results produced by ImageJ are given as area and perimeter; this must be converted to diameter using an equation. We compared the algorithm to ImageJ using images of fluorescent microbeads diluted in PBS at three working densities: low density (LD), medium density (MD), and high density (HD) microbeads were prepared using the fluorescent microspheres and diluting in PBS for final microbead concentrations of 3 beads/ μl , 50 beads/ μl and 100 beads/ μl , respectively (**Figure 4.15a**). The diameter, or size, of the microbeads shows that ImageJ analysis demonstrates a significant difference in size whereas the algorithm keeps the sizes consistent with the size of the microbeads, ranging from 1 – 10 μm (**Figure 4.15b**).^{89–91} The results that the algorithm produces for diameter and size align with the proposed size ranges as well. Previous work has included creating an automated image analysis method using a Java plugin for ImageJ for fluorescence images to determine cardiotoxicity on phenotype changes in hiPSC-CMs.⁹² The algorithm proposed here does not rely on ImageJ and can be modified to include other measurements. In conclusion, the data show that the algorithm is comparable to ImageJ and that it is consistent with the size of cells and microbeads, therefore, we consider it can be used to analyze cells and particles of interest.

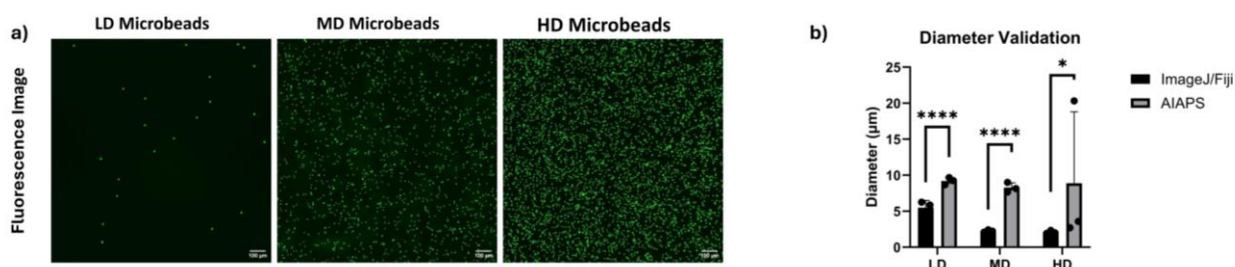


Figure 4.15: AIAPS Validation. (a) original images of green fluorescent microspheres were used to compare the new algorithm (AIAPS) to ImageJ analysis software. Images were analyzed using ImageJ and the AIAPS. (b) ImageJ analysis for diameter was different compared to the new algorithm AIAPS. * $p < 0.05$, ** $p < 0.001$, *** $p < 0.002$, **** $p < 0.001$, $n = 3$, and $N = 5$ images. Low density (LD), medium density (MD), and high density (HD) microbeads were prepared using the fluorescent microspheres and diluting in PBS for final microbead concentrations of 3 beads/ μL , 50 beads/ μL and 100 beads/ μL , respectively.

4.6 DISCUSSION AND CONCLUSIONS

Several studies using capillary-driven microfluidic devices with microposts were conducted. The formation of microposts was first studied to determine if the arrangement of the microposts had any effect on the orientation or morphology of the cells being cultured. Although there was no difference between grid or staggered formation of the microposts, there was a visible difference in the cell formation and morphology of the cells cultured in devices with microposts. These results are consistent with other studies that have investigated alignment of cardiomyocytes in *in vitro* systems developed with microfluidic devices, such as the study conducted by Velhduizen and Nikkah, where after 14 days, the proportion of cells aligned along the horizontal axis significantly increased.²⁵ Following this, the capillary-circuit device was used to study the individual culture of HUVECs and AC16 cells over the course of 1, 3, and 5 days and to determine if 3D vascular and cardiac tissues cultured within the microfluidic devices would respond to the biophysical cues from microposts and exhibit organized cell alignment. Specifically, cardiac tissue models (CTMs) in DWPG displayed preferred cell alignment toward 90° by day 5, whereas vascular tissue models (VTMs) did not show any preferred cell alignment in either device (DWPG or DWoP). This study focused on the separate culture of HUVECs and AC16 cells within microfluidic devices. To further test the capability of the device for coculture studies, HUVECs and AC16 cells were cocultured within Transwell inserts and devices with posts (DWP) to determine cell behavior and changes in morphology. Fluorescence images showed even in coculture studies, AC16 cells elongated around and in between the microposts. Furthermore, two cancer cell lines, SKBR3 and PDX cells, were encapsulated into a collagen hydrogel and placed into Nanoscribe devices, the downscaled size of the DWP for 2 days. These results indicated that tissue models can be cultured within a small-scale device. Lastly, to extract and quantify additional

information from fluorescence images, a Python based code (AIAPS) was developed and modified to meet this need. The AIAPS Script was evaluated and compared to ImageJ/Fiji, where the count and diameter of AC16 cells and fluorescent microbeads were compared. Although the size of AC16 nuclei is unknown, the AIAPS Script did a better job of counting cells or microbeads identified in an image, compared to ImageJ. While ImageJ more accurately measured diameter, it was time consuming to repeat this process for multiple images and with a significantly higher count of items identified in an image. This script demonstrates the possibility of extracting useful information from fluorescence images and its comparison to ImageJ/Fiji. Altogether, this work streamlines the implementation of 3D tissue models within a capillary-circuit microfluidic device.

Chapter 5

Aim 3 – Study the effects of biochemical and physical changes in the cardiovascular and breast cancer microphysiological systems.

5.1 AIM OVERVIEW

Specific Aim 3: Application-specific 3D hiPSC-derived microphysiological system with self-driven microfluidic device.

Goal: Develop 3D tissue models within microphysiological systems to study biochemical and physical effects cardiovascular and breast cancer technical applications.

Hypothesis: The microphysiological systems will be used to study changes in morphology, functionality, and gene expression in cardiovascular and breast cancer technical applications.

Rationale: The developed microphysiological systems will create a 3D cellular microenvironment with capillary-driven flow to study cellular behavior more closely.

Aim 3.1: Develop a 3D breast cancer model to study the effects of Herceptin on hiPSC-CMs.

Aim 3.2: Develop a 3D cardiovascular model to study the effects of microgravity on hiPSC-CMs.

5.2 ABSTRACT

The cardiovascular system is responsible for maintaining blood flow and homeostasis of the human body in normal and in extreme conditions. Two extreme conditions include cancer, one of the leading causes of deaths worldwide, and microgravity exposure of astronauts during spaceflight and long-term missions. Both conditions affect the cardiovascular systems of individuals. For example, breast cancer patients who receive cancer treatments, are more likely to suffer cardiotoxicity in the future and astronauts experience changes in their blood flow while in microgravity and suffer long-term cardiovascular issues when back on Earth's microgravity. These examples of cardiovascular changes need to be investigated to improve the quality of life and

prevent long-term issues in both situations. In this chapter, the capillary-circuit device will be used to develop specific microphysiological systems to study two Technology Applications (TA): TA-1 aims to create a 3D cardiovascular and breast cancer tissue model to study the effects of Herceptin and TA-2 aims to create a 3D cardiovascular tissue model to study the effects of microgravity. Both TAs will utilize hiPSC-CMs within a collagen hydrogel and the capillary-circuit devices to study morphological changes and cell behavior. The fluorescence images acquired for both studies were analyzed using the AIAPS Script. At the end of both studies, it was determined that the capillary-circuit device can be used to develop specific models to study cardiovascular tissues in detail.

5.3 INTRODUCTION

The cardiovascular system plays an essential role in the human body by delivering oxygen, nutrients, and other crucial substances to the organs of the body.⁹³ Additionally, the cardiovascular system is responsible for maintaining homeostasis of the body, including the continuous and controlled movement of blood throughout the body.⁹⁴ It also helps the body manage different activities, such as exercise, stress, and adapt to extreme conditions. Some examples of extreme conditions may include cancer treatment and spaceflight. Although both conditions are undergone separately, they both affect the cardiovascular system and impose long term effects on the individual. The following sections will dive into each condition individually, discuss current research, and identify gaps in each research field.

Cancer is one of the top leading causes of death worldwide and responsible for approximately 10 million deaths in 2020.⁹⁵ The most common cancers in 2020 were breast cancer with 2.26 million cases, lung cancer with 2.21 million cases, and colon cancer with 1.93 million cases.⁹⁵ Cancer mortality can be reduced with early detection and treatment, however not

individuals or countries have the financial means or clinics with the equipment needed to accomplish this. Effective cancer treatment is based on the cancer diagnosis and often consists of a combination of treatments including surgery, medications and/or therapies to decrease the size of the cancer or the progression or migration of cancer.⁹⁶ Specifically, breast cancer is the most common cancer among women in the United States (US), where the average women in the US will have a 13% chance of developing breast cancer.⁹⁷ Advances in early detection and treatment options have improved survival changes and due to this, there has been a shift to focus on reducing the acute and chronic side effects following cancer treatment.⁹⁸ One chronic effect is cardiotoxicity, which is any damage to the heart or cardiovascular system, after cancer treatment and affects survivor quality of life and cause of death.⁹⁹ Cardiovascular mortality is the top cause of death in breast cancer survivors, where the change of cardiotoxicity death increases with pre-existing cardiovascular conditions before cancer treatment.⁹⁹ The research for reducing the effect of cardiotoxicity and/or management in breast cancer survivors is limited. There is a need to develop in vitro models to study how cardiovascular cells are affected by cancer cells and cancer therapeutics to predict cardiac toxicity levels in patients.

One study conducted by Weng and George, a microfluidic device platform was used to culture human induced pluripotent stem cell derived endothelial cells (hiPSC-ECs) and cardiomyocytes (hiPSC-CMs) and incorporate human tumors within the same space.¹⁰⁰ Several drugs (Doxorubicin and Oxaliplatin) were tested on this multicellular platform to monitor how the function of the cardiomyocytes changes as the tumor grows. Doxorubicin affected the cardiomyocyte spontaneous beating and conduction velocity, while Oxaliplatin also affected overall cardiac function. This demonstrated one way to study cardiac toxicity of tumor and cardiac cells at the same time.

In the last few decades, there has been a major push for space exploration to study Earth and our solar system, as well as advance and create new technologies to improve our lives on Earth, but also in space and beyond. It is known if a person stays in space for an extended period, there will be physiological changes, including the weakening of muscles and bones, and increased exposure to microgravity and radiation. Spaceflight and microgravity cause astronauts to experience changes in blood volume, aerobic capacity, and increased chances of cardiovascular problems upon their return to Earth's gravity.¹⁰¹ The post-spaceflight effects of the cardiovascular system are not well understood, including the molecular and cellular changes and the translation into long-term cardiovascular problems. There is a need to develop models to study the cardiovascular changes that occur during spaceflight and how to prevent detrimental effects.

Microgravity research with 2D models and animal models have revealed changes in cardiomyocyte structure and function. Payloads with hiPSC-CMs have been launched to the ISS for evaluation of cardiomyocyte morphology and function, but this can be expensive and 2D models do not accurately model the 3D cellular microenvironment. Microgravity studies can benefit from the integration of hiPSC-derived CMs into a microfluidic platform with simulated microgravity systems, such as rotary cell culture systems.¹⁰² This opens the door for researchers to conduct simulated microgravity experiments on Earth.

To address these gaps, this chapter will focus on two technology applications (TA): TA-1) 3D cardiovascular and breast cancer tissue model to study the effects of Herceptin and TA-2) 3D cardiovascular tissue model to study the effects of microgravity on CM structure and morphology **(Diagram 5.1)**.

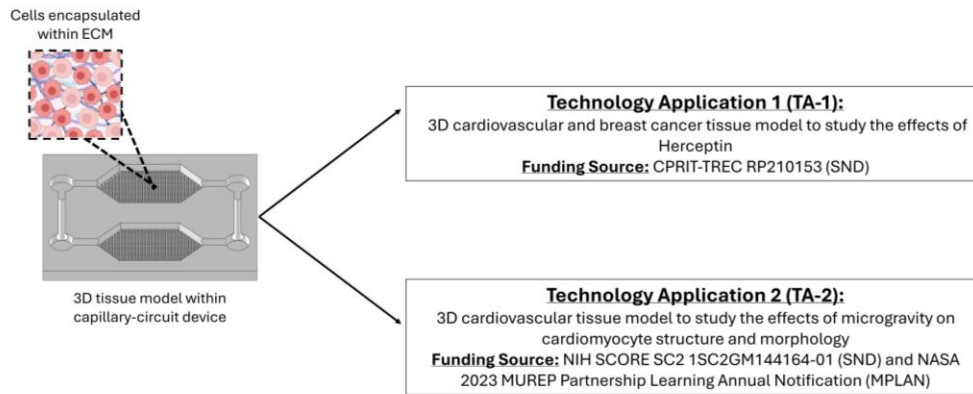


Diagram 5.1: Technology applications 1 and 2 of the microphysiological system.

5.4 MATERIALS AND METHODS

5.4.1 Human induced pluripotent stem cell (hiPSC) culture and maintenance

Human induced pluripotent stem cell (hiPSC) line GM25267 (Coriell Institute) were grown on plates coated with growth factor-reduced Matrigel (Corning) at 250,000 cells/well and were fed with Essential 8 medium (Gibco). hiPSCs were passaged every 3 days using Accutase (STEMCELL Technologies) and rho-associated protein kinase (ROCK) inhibitor (10 μ M, Y-27632, STEMCELL Technologies) was added to the medium the first 24 hours after passaging. The cells were fed with Essential 8 medium until the day of passaging.

5.4.2 hiPSC-cardiomyocyte (CM) differentiation protocol

The modified protocol for cardiomyocyte cell differentiation presented here was adapted from previous hiPSC-CM differentiation protocols and is summarized in **Figure 5.2**.^{103,104} First, the hiPSCs were passaged onto plates coated with growth factor-reduced Matrigel (Corning) at 250,000 cells/well and fed Essential 8 media with 10 μ M ROCK inhibitor (day -3). The medium was replaced the next day (day -2) with Essential 8 without ROCK inhibitor. The cells were fed with Essential 8 medium and grown until day 0 (~70-80% confluency) with the initial seeding density of 250,000 cells/well. The differentiation started on day 0, by feeding the hiPSCs Roswell

Park Memorial Institute Medium (RPMI) B27 – Insulin (Gibco) with 5 uM CHIR 99021 (STEMCELL Technologies). On day 3, the medium was replaced with RPMI B27 – Insulin (Gibco) with 10 uM IWP4 (STEMCELL Technologies). On day 5, the medium was replaced with RPMI B27 – Insulin (Gibco). On day 7, the medium was replaced with RPMI B27 complete. On day 7, spontaneous beating was observed and the cells were fed with RPMI B27 complete every other day. Between day 12-16, hiPSC-CMs were used for flow cytometry analysis, cell encapsulation, or beat rate studies.

5.4.3 Flow cytometry (FC) analysis

Cells were dissociated using Accutase (STEMCELL Technologies) with three 10-minute incubation periods standard conditions at 37°C and 5% CO₂. Every 10 minutes, the cells were checked for detachment and gently mechanically dissociated using a 10 mL serological pipette and placed back into incubation. This process was repeated two more times until the 30 minutes, or all cells were detached. The cells were quenched with RPMI B27 complete (1:2 Accutase to RPMI B27 complete). The cell mixture was collected, centrifuged at 1200 RPM for 5 minutes and the supernatant was removed. The cells were washed with 1x PBS and fixed with 4% paraformaldehyde for 10 minutes. After 10 minutes, 4 mL of PBS was added and the sample was centrifuged and the supernatant was removed. The sample was permeabilized in 0.1% Triton for 5 minutes. Next, 4 mL of PBS was added, the sample was centrifuged, and the supernatant was removed. The sample resuspended in FACSB10 buffer and stained with the fluorescent antibodies listed in **Table 5.1**. The sample and primary antibodies were incubated for 1-2 hours at room temperature, subsequently washed with PBS, and resuspended in FACSB10. The secondary antibody was then added to the samples and incubated in the dark for 1-2 hours at room temperature. If the antibodies were conjugated, the incubation time was 1 hour. Samples were

analyzed with a Beckman Coulter Gallios flow cytometer. The FL1, FL2, and FL6 lasers were used to obtain the data. The data was analyzed with Kaluza analysis software (Beckman Coulter) and gating was based on corresponding isotype controls or secondary antibodies.

Table 5.1: List of fluorescent antibodies used for flow cytometry analysis.

| Cell Type | Antibodies | Purpose |
|------------------|--|-----------------|
| hiPSCs | SOX2-PE Mouse IgG2A, Oct-3/4-APC Rat IgG2B, SSEA-4-CFS Mouse IgG3, SSEA-1-PerCP Mouse IgM Isotype Controls, Mouse IgG3-CFS Isotype Control, Mouse IgG2A-PE Isotype Control (R&D Systems) | Pluripotency |
| hiPSC-CMs | Cardiac Troponin T Monoclonal Antibody (13-11), Invitrogen, Alexa Fluor 488 goat anti-mouse secondary antibody | cTnT expression |
| hiPSC-CMs | APC Mouse IgG1 isotype control (Biolegend), APC anti-human CD340 HER2 (Biolegend) | HER2 expression |

5.4.4 Immunofluorescence staining

hiPSC-CM samples were rinsed with 1x PBS (Gibco) and fixed with 4% paraformaldehyde (PFA, ThermoFisher) for 10 min. PFA was removed and samples were rinsed with PBS twice. Samples were permeabilized with 0.1% Triton for 5 minutes and then rinsed two times with 1x PBS. Samples were then blocked with 2% Bovine Serum Albumin (BSA, Fisher Bioreagents) for 10 minutes. The 2% BSA solution was removed, and samples were stained with 1:200 primary antibodies in 2% BSA overnight at 4°C. **Table 5.2** outlines the cell type, primary antibodies, and secondary antibodies used for immunostaining. The following day, samples were rinsed twice with 1x PBS and stained with fluorescent secondary antibodies at a 1:200 ratio in 2% BSA at room temperature for 1 hour. Samples were rinsed twice with PBS and subsequently stained with Actin-

stain 555 phalloidin (ActinRed 555 ReadyProbes Invitrogen) and nuclei were stained with DAPI (NucBlue Fixed Cell Stain ReadyProbes, Invitrogen) for 10 min at RT. Samples were washed with PBS once and fluorescence images were captured with a Leica Thunder Imager Live Cell and 3D Assay fluorescent microscope with a 10x or 40x objective lens (Leica Microsystems, Buffalo Grove, IL).

Table 5.2: Primary and secondary antibodies for immunostaining.

| Cell Type | Primary Antibody | Secondary Antibody |
|------------------|--|--|
| hiPSC-CMs | Cardiac Troponin T Monoclonal Antibody (13-11), Invitrogen | Alexa Fluor 488 goat anti-mouse secondary antibody |
| hiPSC-CMs | Primary anti-human HER2, Biologend | Alexa Fluor 488 goat anti-mouse secondary antibody |

5.4.5 Image analysis using AIAPS

Fluorescence images were acquired for each sample and experiment, where at least n=3 for each condition. F-actin and DAPI (red and blue merged images, respectively) were saved as .JPEG files and uploaded into the AIAPS Script to obtain cell count and diameter size as previously described in Chapter 4. The .CSV files with respective values for each image set were saved and used for statistical analysis in GraphPad Prism.

5.4.6 Beat rate time lapse videos and calculation

Videos of spontaneously beating hiPSC-CMs were acquired using a Leica Thunder 3D Imager microscope with a DLS 9000GT camera. The beat rate of hiPSC-CMs in plate and encapsulated within a 3D collagen hydrogel were calculated using the average displacement over time formula. The average displacement values were acquired using the MTrackJ plugin from ImageJ/Fiji (NIH).¹⁰⁵ The average displacement was calculated and the beats per minute were calculated based on this information.

5.4.7 Technology Application 1 (TA-1) - 3D cardiovascular and breast cancer tissue model

TA-1 is focused on developing a 3D cardiovascular and breast cancer tissue model to study the effects of Herceptin on cardiomyocyte function.

I. hiPSC-CM culture and dissociation

hiPSC-CMs were maintained in RPMI B27 complete medium for 14-16 days post-differentiation. The cells were dissociated using Accutase (STEMCELL Technologies) with an incubation of 30 minutes with occasional mechanical dissociating every 10 minutes. The cells were quenched with RPMI B27 complete medium and centrifuged to obtain the cell pellet. The cells were counted and collected at 1×10^6 cells/mL.

II. SKBR3 cell culture and dissociation

SKBR3 breast cancer cells were maintained in RPMI B27 complete media with 10% FBS. At 80% confluency, the cells were dissociated using Trypsin (0.25% Corning) with an incubation of 5 minutes and quenched with RPMI B27 complete with 10% FBS in preparation of coculture studies with hiPSC-CMs.

III. Development of 3D cardiovascular and breast cancer tissue models

hiPSC-CMs and SKBR3 cells were encapsulated into a 0.2wt% collagen hydrogel, prepared as described in Chapter 4 and at a seeding density of 1×10^6 cells/mL (hiPSC-CMs) and 500,000 cells/mL (SKBR3). There were 4 different culture conditions. In the first two conditions, hiPSC-CMs encapsulated within a collagen hydrogel were either loaded into a Transwell insert (12 mm) or the device with posts for a 5 day culture. hiPSC-CMs in Transwell inserts and devices were maintained in control conditions for 5 days without Herceptin exposure and hiPSC-CMs in Transwell inserts and devices were cultured for 3 days followed with 2 day Herceptin exposure. The other two conditions consisted of hiPSC-CMs cocultured with SKBR3 cells in Transwell

inserts (12 mm) in one well of a 6-well multiwell plate or in their own respective chambers in the device with posts with the common cell medium of RPMI B27 complete with 10% FBS. Similarly, the coculture of hiPSC-CMs and SKBR3s were either cultured in control conditions without Herceptin exposure or cultured with 3 days followed with 2 day Herceptin exposure. The purpose of this study was to evaluate the effects of Herceptin on hiPSC-CMs in 3D culture and the effects of SKBR3 and Herceptin exposure on hiPSC-CM morphology.

All cell-hydrogels in either the capillary-circuit microfluidic device or Transwell inserts were placed into the incubator to allow the hydrogel to crosslink. Medium was added to each hydrogel; RPMI B27 complete for hiPSC-CM samples and RPMI B27 complete + 10% FBS for hiPSC-CM and SKBR3 coculture samples.

IV. Herceptin exposure studies

Herceptin (Trastuzumab anti-HER2, Selleckchem) was reconstituted in PBS and then directly added into cell medium for a final concentration of 10 uM. Control studies, where no Herceptin was added, were cultured for 5 days with medium changes every other day. For Herceptin studies, the samples were cultured for 3 days, and Herceptin was added for 48 hours (2 days). Every condition was conducted in triplicate, including controls and Herceptin exposed samples. On day 5, all samples were observed for hiPSC-CM spontaneous beating and then fixed for immunofluorescence imaging.

5.4.8 Technology Application 2 (TA-2) - 3D cardiovascular tissue model for microgravity

TA-2 is focused on developing a 3D cardiovascular tissue model to study the effects of simulated microgravity on cardiomyocyte structure and morphology.

I. Microgravity Finite Element Analysis (FEA) simulation

Solidworks Fluid Flow Simulation was used to simulate the fluid flow within the rotating bioreactor vessel. First, a simplified bioreactor vessel was designed in Solidworks and multiple Nanoscribe device models were added to the CAD model of the vessel. For study parameters, the same rotational settings applied on the bioreactor rotational base, 2.8 rpm, was added to the simulation. Additionally, an inlet volume of 3 mL was added to the simulation, as this was the total volume of cell medium added to the vessel after addition of the Nanoscribe device with the cell-hydrogel. The liquid chosen for the simulation was room temperature water and the simulation was based on laminar flow, due to the very low RPM settings.

To calculate the fluid velocity in the bioreactor, the following equation was used:

$$v = w \times r$$

Where v is the fluid velocity in the bioreactor vessel, w is the angular velocity or rpm, and r is the radius of the bioreactor vessel. The operational rotations of the bioreactor vessel were 2.8 rpm, the lowest the Synthecon Inc. rotary cell culture system used for this study allows. The radius of the bioreactor vessel is 25.4 mm. After incorporating these values into the main equation, the fluid velocity within the bioreactor vessel is 71.12 mm/min, converting to mm/s, results in a fluid velocity of 1.18 mm/s.

The G-force of the bioreactor vessel during rotation can be calculated using this equation:

$$G \text{ force} = 11.2 \times \text{radius} \times \left(\frac{\text{RPM}}{1000}\right)^2$$

Where the radius is 25.4 mm, and the RPM is 2.8. The calculated G-force value for the bioreactor vessel during this rotation is 0.00223 mm/s².

The flow rate can be calculated using the fluid velocity in the bioreactor vessel by using the following equation:

$$Q = A \times v$$

Where Q is the flow rate within the bioreactor vessel, A is the cross-sectional area of either the bioreactor or the Nanoscribe devices, and v is the fluid velocity within the bioreactor. The cross-sectional area of the bioreactor is 2026.83 mm² and the cross-sectional area of the Nanoscribe device is 63 mm². The flow rate of the bioreactor vessel is 2391.65 mm³/sec and the flow rate of the Nanoscribe device is 74.34 mm³/sec. The flow rates can be converted to mL/sec, where the flow rate of the bioreactor is 2.391 mL/sec and the flow rate of the Nanoscribe device is 0.074 mL/sec. The flow rate of the bioreactor vessel is close to the 3 mL of fluid added during experiments. The flow rate of the Nanoscribe device is small due to its overall dimensions.

Solidworks Fluid Flow Simulation was used to simulate the fluid flow within the rotating bioreactor vessel. First, a simplified bioreactor vessel was designed in Solidworks and multiple Nanoscribe device models were added to the CAD model of the vessel. For study parameters, the same rotational settings applied on the bioreactor rotational base, 2.8 rpm, was added to the simulation. Additionally, an inlet volume of 3 mL was added to the simulation, as this was the total volume of cell medium added to the vessel after addition of the Nanoscribe device with the cell-hydrogel. The liquid chosen for the simulation was room temperature water and the simulation was based on laminar flow, due to the very low RPM settings.

II. Bioreactor rotating vessel preparation

A Sythecon Inc. Rotary Cell Culture System was used and is referred to as the Bioreactor system. All components of the vessel were rinsed with water, lightly scrubbed with soft detergent and rinsed. The components were then placed into a 4L beaker with molecular grade water and

soaked overnight. The following day, the components were air dried and assembled. Using a serological pipette, 5 mL of 70% ethanol was added into the vessel for sterilization and soaked overnight. The following day, the ethanol was removed. The ports were removed, and the peripheral screws were loosened by two turns. The ports and the vessel were autoclaved for 20 minutes at 121°C. Once autoclaved, the vessel was conditioned with cell medium (RPMI B27 complete) over night to check for contamination and to adjust to the standard incubation conditions.

III. hiPSC-CM culture and dissociation

hiPSC-CMs were dissociated using Accutase (STEMCELL Technologies) with an incubation of 30 minutes with occasional mechanical dissociating every 10 minutes. The cells were quenched with RPMI B27 complete medium and centrifuged to obtain the cell pellet. The cells were counted and collected at 1×10^6 cells/mL.

IV. Development of 3D cardiovascular tissue models in simulated microgravity

hiPSC-CMs were encapsulated into a 0.2wt% collagen hydrogel, prepared as described in Chapter 4 and at a seeding density of 100,000 cells/mL. hiPSC-CMs were prepared for two different culture conditions. The first culture condition is the standard incubation of hiPSC-CMs encapsulated within a collagen hydrogel and loaded into a Nanoscribe device and cultured for 3 days. The second condition is the simulated microgravity condition using the rotating bioreactor system, where hiPSC-CMs encapsulated into a collagen hydrogel and loaded into a Nanoscribe device are placed inside of the bioreactor chamber. Both conditions were placed into the incubator to maintain the samples. A total of 6 devices were prepared for each condition.

5.4.9 Statistical Analysis

All quantitative measurements were performed in triplicate samples, unless otherwise stated. All values are expressed as mean \pm Standard Deviation (SD). A Oneway ANOVA with a post-hoc Tukey test, and a 2way ANOVA were used to compare treatment groups; and $p < 0.05$ was used to assess statistical significance using GraphPad Prism.

5.5 RESULTS AND DISCUSSION

5.5.1 hiPSCs characterization

Prior to CM differentiation, hiPSCs (GM25267) were analyzed for pluripotency using flow cytometry. **Figure 5.1** shows the forward scatter and side scatter plot of the hiPSCs. All pluripotency markers, including SOX2 and OCT4, were $>95\%$, indicating the hiPSCs were pluripotent prior to differentiation.

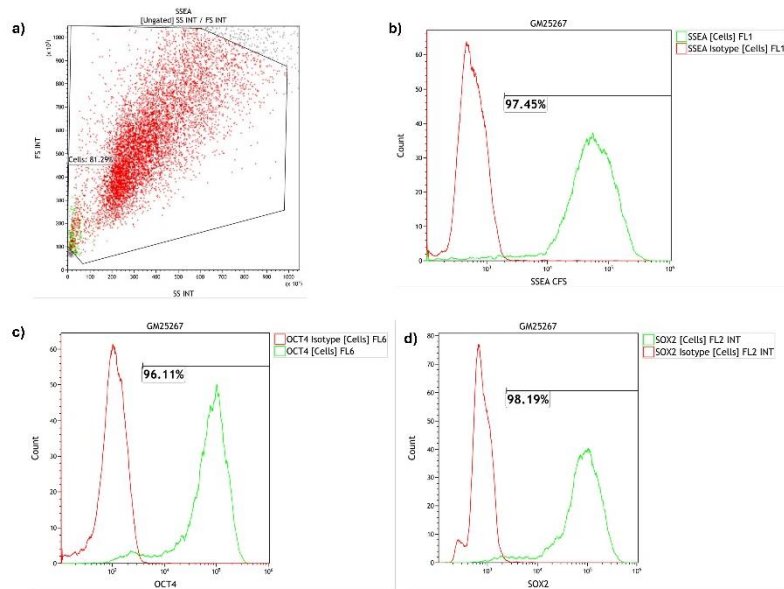


Figure 5.1: Flow cytometry analysis of hiPSCs (GM25267).

5.5.2 hiPSC-CM differentiation and characterization

After CM differentiation, hiPSC-CMs were fixed, stained, and analyzed for cTnT expression using flow cytometry. The range of cTnT was dependent on the post-differentiation

day the cells were used for flow cytometry or for experiments. **Figure 5.2** shows the CM differentiation protocol and the forward scatter and side scatter plot of the hiPSC-CM sample, as well as the expression percentage of cTnT+ cells. The hiPSC-CMs used for this flow cytometry analysis were post-differentiation day 16 cells. **Table 5.3** lists three replicates (n=3) of hiPSC-CMs for cTnT+ expression, with an average cTnT+ expression.

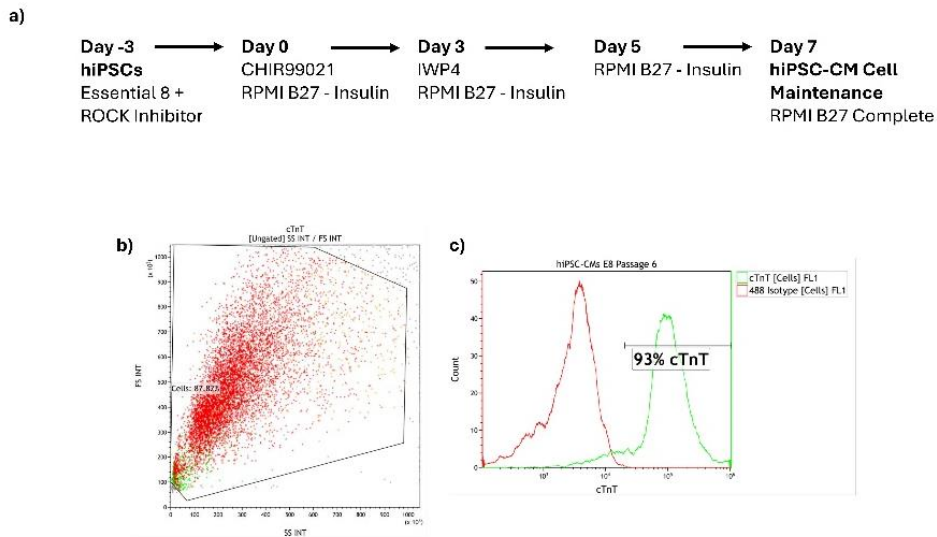


Figure 5.2: CM differentiation protocol and flow cytometry analysis of post-differentiation day 16 hiPSC-CMs for cTnT expression.

Table 5.3: Flow cytometry replicates for cTnT+ expression.

| Replicate | cTnT+ Expression |
|---------------------------|------------------|
| 1 | 82.81% |
| 2 | 75.78% |
| 3 | 93% |
| Average | 83.36% |
| Standard Deviation | ±8.73 |

Likewise, hiPSC-CMs were stained for immunofluorescence and imaged using the Leica 3D Thunder Assay microscope. **Figure 5.3** shows the 2D monolayer staining for cTnT, F-actin, and DAPI using 10x and 40x objectives.

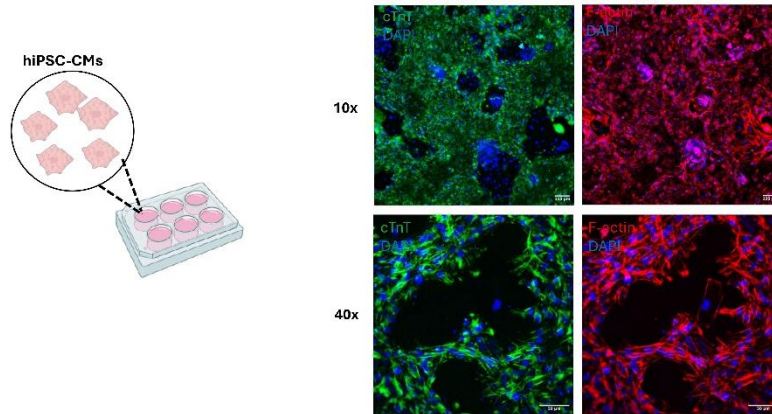


Figure 5.3: Fluorescence images of 2D monolayer culture hiPSC-CMs.

The flow cytometry analysis for cTnT and fluorescence images confirm that the CM differentiation was successful. Additionally, the modified protocol did not require a CM purification step, as most CM differentiations resulted in a cTnT+ population of >80% or higher.

5.5.3 Beat rate analysis

The Leica 3D Thunder Assay Microscope with the humidity chamber was used to obtain time lapse videos of spontaneously beating hiPSC-CMs in 2D monolayer culture and in 3D culture within Transwell inserts. The videos were analyzed using the MTrackJ ImageJ/Fiji plugin and beats per minute were calculated using average displacement values.^{106,107} **Table 5.4** lists the average displacement and beats per minute (BPM) for each condition. Each condition had 3 replicates and has its representative standard deviation. The calculated beats per minute are similar to other research publications.^{106,107}

Table 5.4: Average displacement and hiPSC-CM beats per minute.

| Condition | Average Displacement | Beats Per Minute |
|-----------------------|-----------------------------|-------------------------|
| In Plate (2D) | 2.587(\pm 0.524) | 80 |
| Transwell insert (3D) | 3.783(\pm 0.72) | 32 |

5.5.4 TA-1 3D cardiovascular and breast cancer tissue model

I. hiPSC-CM HER2 characterization

Post-differentiation day 16 hiPSC-CMs were fixed, stained, and analyzed for cTnT and HER2 expression using flow cytometry. **Figure 5.4** shows the forward scatter and side scatter plot of the hiPSC-CM sample, as well as the expression percentage of cTnT+ and HER2+ cells. Figure #d shows the quadrant plot, demonstrating simultaneous expression of cTnT and HER2. This may imply hiPSC-CMs inherently express some level of HER2 and this expression is affected by the presence of cancer cells or chemotherapeutics.

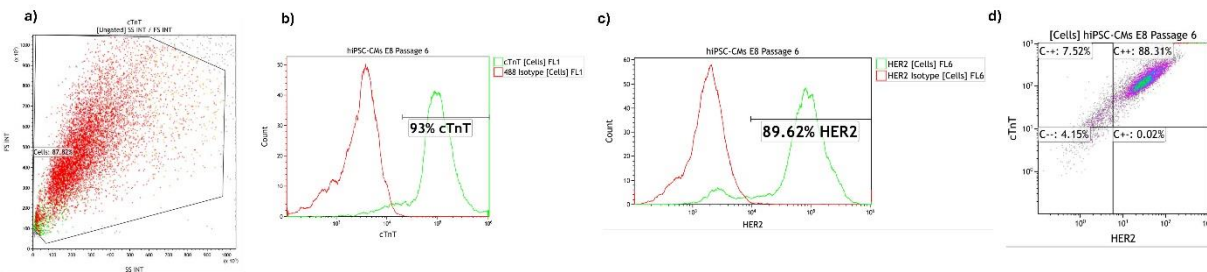


Figure 5.4: Flow cytometry analysis of post-differentiation day 16 hiPSC-CMs for cTnT and HER2 expression.

Additionally, hiPSC-CMs were immunostained with HER2 to visualize HER2 expression.

Figure 5.5 shows fluorescence images of hiPSC-CMs that express HER2.

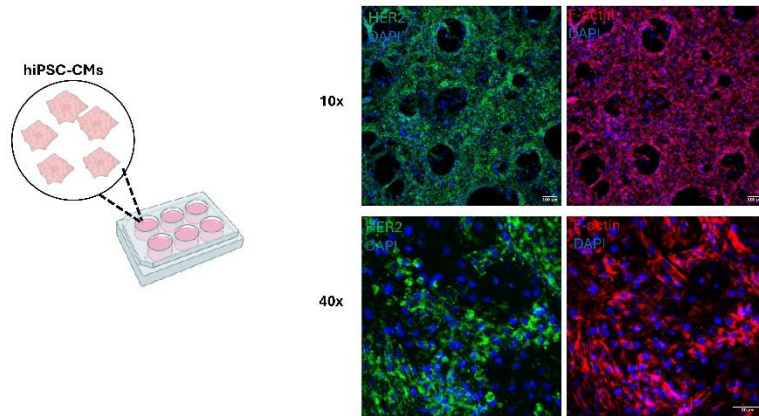


Figure 5.5: Fluorescence images of 2D monolayer culture hiPSC-CMs with HER2, F-actin and DAPI.

II. Herceptin studies

A preliminary exposure study with Herceptin was conducted to assess the hiPSC-CM response to biochemical and/or physical stimuli in devices with posts. Control and Herceptin studies were conducted for a total of 5 days, where samples treated with Herceptin were maintained for 3 days followed by 2 days of Herceptin exposure. On day 5, all samples (control and Herceptin samples) were placed in the humidified chamber for identification of hiPSC-CM spontaneous beating. Control samples, in both Transwell inserts (12 mm) and devices, showed small clusters of hiPSC-CMs that were beating. However, in hiPSC-CM only and hiPSC-CM – SKBR3 coculture control and Herceptin exposed devices, there was little to no hiPSC-CMs beating. Additionally, most hiPSC-CMs in Transwell inserts and devices were rounded, despite hiPSC-CM spontaneously beating in some areas. **Figures 5.6-5.8** shows fluorescence images of each culture condition in hiPSC-CM only studies and hiPSC-CMs cocultured with SKBR3 cells. Both hiPSC-CMs and SKBR3s are affected when treated with Herceptin.

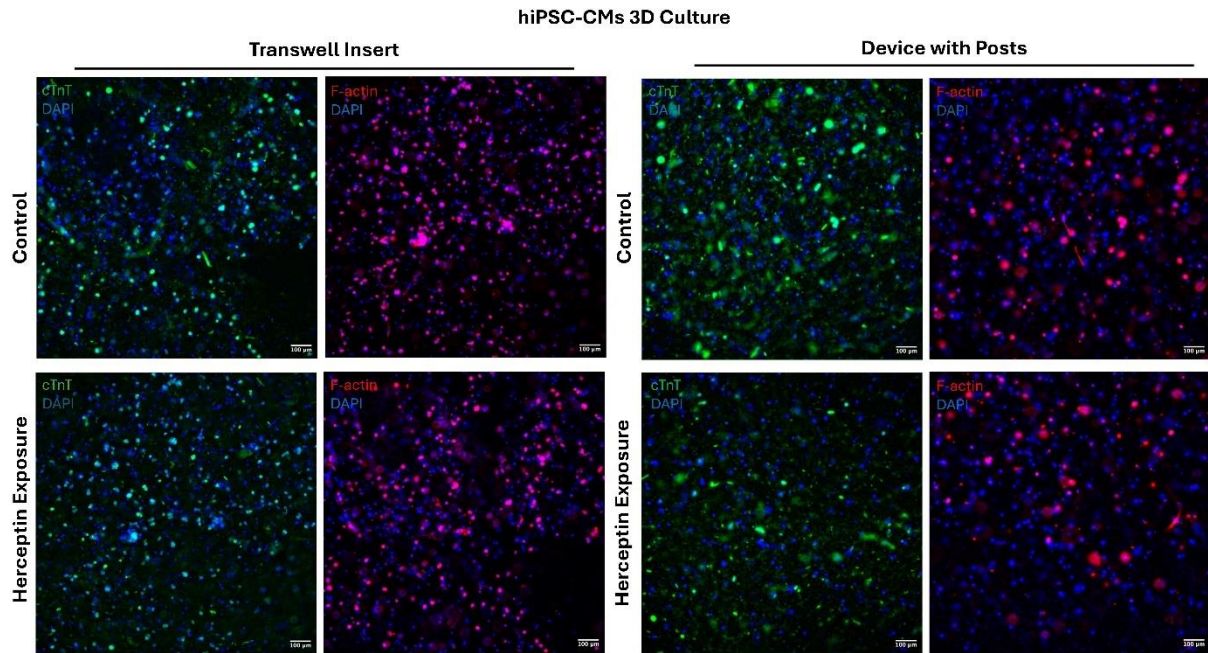


Figure 5.6: Fluorescence images of hiPSC-CMs only in Transwell inserts and devices.

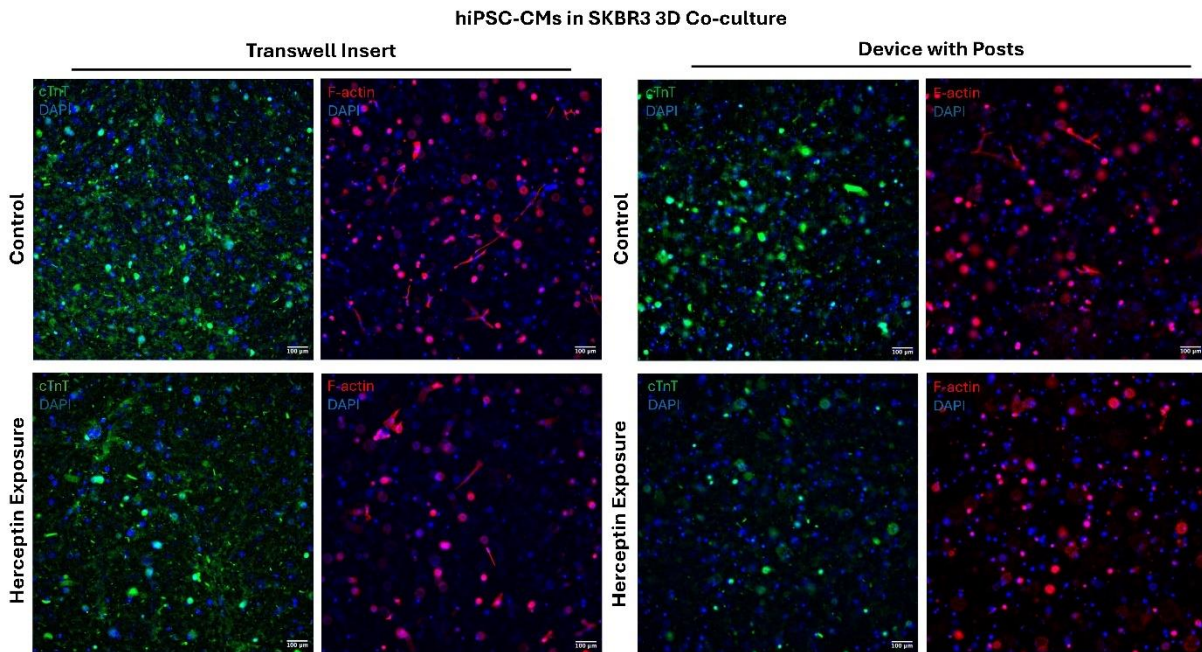


Figure 5.7: Fluorescence images of hiPSC-CM cocultured with SKBR3 in Transwell inserts and devices.

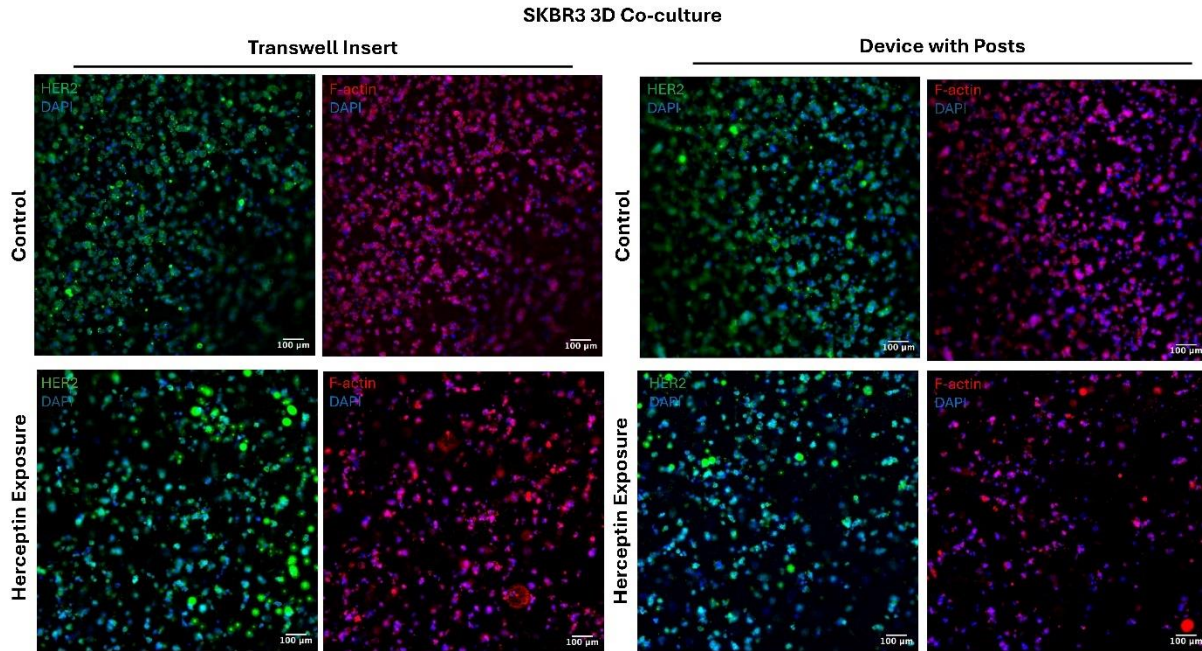


Figure 5.8: Fluorescence images of SKBR3s cocultured with hiPSC-CMs in Transwell inserts and devices.

Figure 5.9 shows the quantification of the fluorescence images for control and Herceptin exposure studies. There was no significant increase or decrease in cell count or diameter. This may be attributed to the cell roundness observation in all conditions in live imaging and in fluorescence images. Additionally, changes in cell morphology were observed in collagen hydrogel encapsulations prior to the Herceptin studies from other experiments within our lab. The hydrogel used in this study must be optimized to provide a microenvironment that is not harmful to the hiPSC-CMs in the study to be able to gather more informative data.

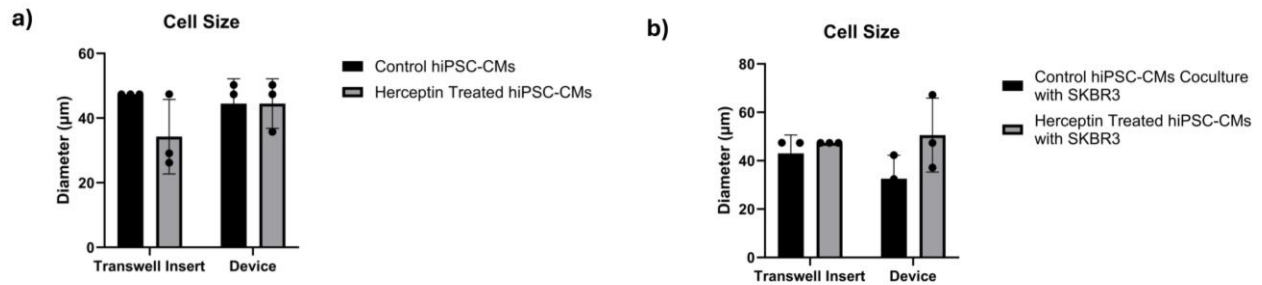


Figure 5.9: Quantification of cell diameter for a) hiPSC-CM 3D culture in Transwell insert and devices and b) hiPSC-CM coculture with SKBR3 in Transwell insert and devices.

5.5.5 TA-2 3D cardiovascular tissue model for simulated microgravity

I. Rotational fluid flow simulation

The incorporation of a microfluidic device within the bioreactor vessel may affect the fluid flow within the bioreactor vessel. To simulate the fluid flow within the bioreactor vessel with microfluidic devices, an FEA simulation was conducted. **Figure 5.10d** shows the fluid flow simulation with the bioreactor vessel rotating at the same rpm as the experimental study was conducted. The highest fluid flow velocity (~8 mm/s) is observed approaching the outermost edges of the bioreactor vessel, while the closer to the center of the vessel, there are lower velocities. This is beneficial as the outermost edges of the devices do not have any samples that are constantly exposed to this high fluid velocity. This also confirms the forces the 3D hiPSC-CMs samples in microgravity experience are minimal.

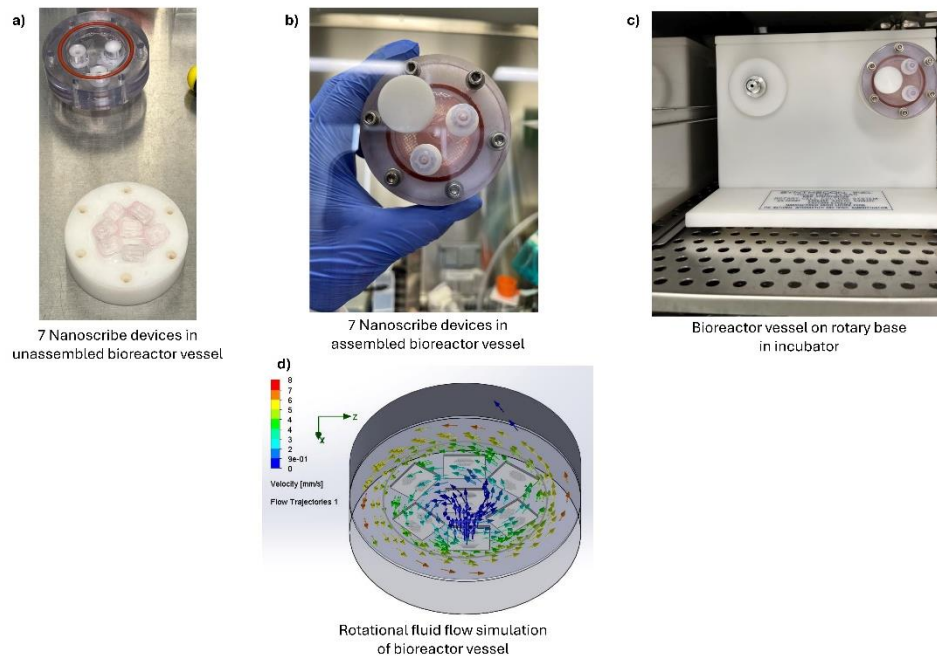


Figure 5.10: Nanoscribe device loading into bioreactor vessel (a), final assembly of bioreactor vessel (b), bioreactor vessel placement onto rotary base for simulated microgravity experiments (c), and rotational fluid flow simulation of simulated microgravity experiments (d).

II. Control and simulated microgravity studies

A 3-day study was conducted with control and microgravity samples. The Nanoscribe device was chosen for microgravity experiments due to its small dimensions and the ability to fit multiple devices in the bioreactor vessel (~6-7 devices) as seen in **Figure 5.10**. After three days, the microgravity 3D hiPSC-CM hydrogels were still intact and may have the potential for longer studies, such as 5-7 days.

Figure 5.11 shows fluorescence images for control and microgravity 3D hiPSC-CM samples. The representative fluorescence images do not show a major difference in F-actin and DAPI, but there does seem to be a difference in the cTnT expression in control compared to simulated microgravity. To quantify this potential change, the fluorescence images were analyzed using the AIAPS Script for cell diameter (**Figure 5.11b**). There was not a significant difference in the cell count in either condition, however there was a higher standard deviation in the

microgravity samples. On the other hand, the cell diameter significantly increased from the control samples to the microgravity samples. Further studies can be used to investigate the cellular processes that may cause the change in nuclei size, as well as the changes in gene expression in control and microgravity studies.

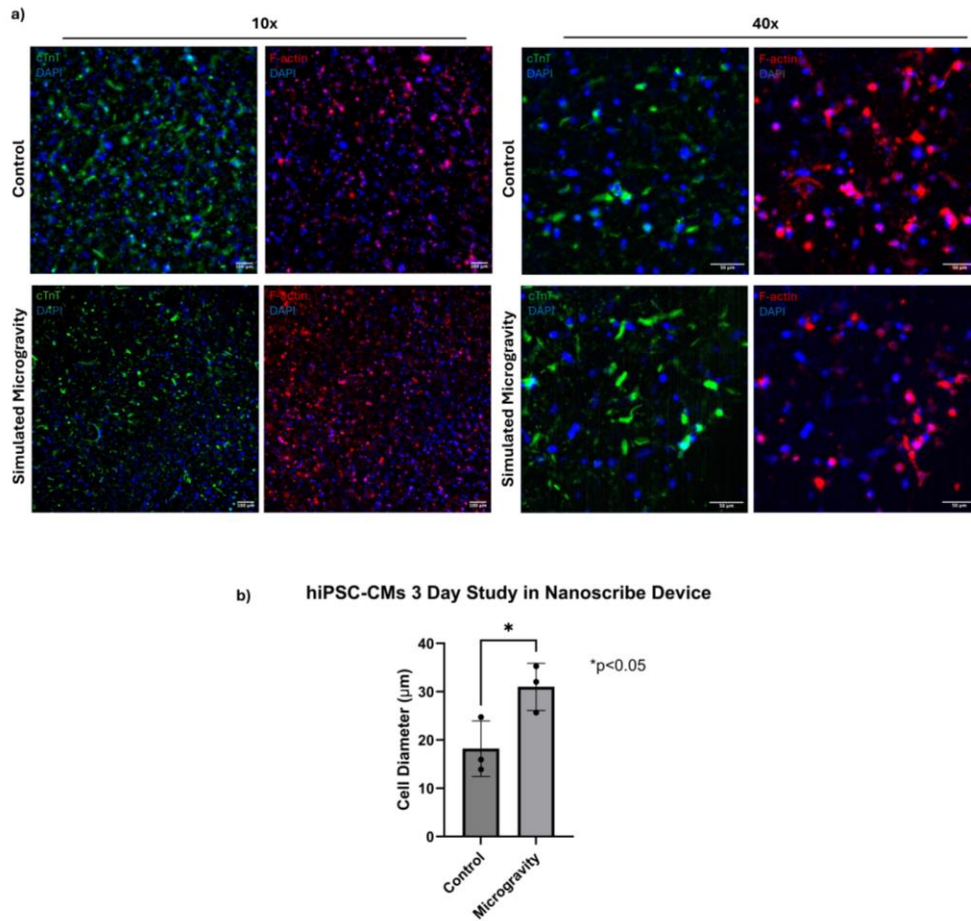


Figure 5.11: Representative fluorescence images of control Nanoscribe hiPSC-CM samples subjected to standard incubation and simulated microgravity Nanoscribe hiPSC-CM samples (a) and image analysis of cell diameter (b) using AIAPS Script.

Additionally, beating of hiPSC-CMs in control conditions on day 5 was observed and the beat rate is outlined in **Table 5.5**. Simulated microgravity samples were evaluated for any beating after removal from the bioreactor. hiPSC-CMs exposed to simulated microgravity did not beat

after immediate removal from the bioreactor. It should be noted that previous studies with hiPSC-CMs and microgravity studies allowed a recovery period for the hiPSC-CMs after microgravity.

Table 5.5: Average displacement and hiPSC-CM beats per minute.

| Condition | Average Displacement | Beats Per Minute |
|------------------|---|-------------------------|
| Nanoscribe | 2.423 μm (± 0.85 , n=3) | 30 |

5.6 DISCUSSION AND CONCLUSIONS

The capillary-circuit device developed in Aim 1 was used to study two Technology Applications (TA). Technology Application (TA-1) was centered on developing a 3D cardiovascular and breast cancer tissue model to study Herceptin effects. In this study, hiPSC-CMs were cultured in Transwell inserts and capillary-circuit devices, with some control (no exposure) and Herceptin exposed samples. Through live imaging for hiPSC-CM beat rate analysis, it was observed that not many CMs were beating in control or Herceptin samples. Additionally, fluorescence images and image analysis revealed there were no significant changes in cell diameter in Transwell insert or devices, as well as in control or Herceptin exposure. Limitations of this study included the extracellular matrix (collagen) and the cell behavior in this hydrogel. This study would need to be repeated to better understand how Herceptin is affecting the hiPSC-CMs and how the SKBR3 cells are interacting with the hiPSC-CMs in coculture studies. In Technology Application (TA-2), the goal was to develop a method of studying 3D cardiovascular tissues in microgravity. In this study, hiPSC-CMs were encapsulated into a collagen hydrogel and placed into Nanoscribe devices for cultures in either standard incubation conditions or simulated microgravity within a bioreactor (rotary cell culture system). At the end of the 3-day study, the microgravity 3D samples were intact, showing promise for longer microgravity studies. Fluorescence images demonstrated a difference in cTnT expression in control samples compared to microgravity samples. With further analysis of cell diameter using the AIAPS Script, there was

a significant increase in the cell diameter in microgravity samples. Further studies to investigate the cellular changes of hiPSC-CMs in microgravity would be useful. In conclusion, this work demonstrated that the capillary-circuit device can be used to develop microphysiological systems for specific studies and applications.

Chapter 6

Conclusions and future directions

6.1 CONCLUSIONS

Chapter 3 discusses the design and development of a capillary-driven microfluidic device that uses multiple fabrication techniques. In the pursuit of developing a microfluidic device for the advancement of physiologically relevant 3D *in vitro* models, the device design was optimized to include two tissue chambers for coculture studies and the streamlined fabrication technique to allow long-term culture and in-house imaging. The material, either 3D printed or Ostemer322, demonstrated capillary-driven flow. However, the 3D SLA resin was not optically clear and resulted in the material change to Ostemer322 for future applications.

Shifting focus to the implementation of cardiovascular tissue models within the capillary-circuit devices, the studies in Chapter 4 aimed to address the optimization and development of this system. The refined fabrication methods of capillary-circuit devices allowed for studies of commercially available cell lines such as HUVECs, AC16 cardiomyocytes, SKBR3 cells, and even the implementation of patient derived xenograft (PDX) cells into the devices. Both cardiovascular and cancer cell types maintained their morphology in 3D within the capillary-circuit devices and the downscaled devices (Nanoscribe). The fabrication methods of the Nanoscribe device using Ostemer322 shows a breakthrough in device fabrication and microstructure integrity at this scale. These studies show promise for the continuation of developing a physiologically relevant *in vitro* model.

Expanding the capillary-circuit device into a microphysiological system, Chapter 5 showed the Technology Applications of studying cardiovascular and breast tissue models (TA-1) and cardiovascular tissue models in simulated microgravity (TA-2). TA-1 showed the integration of

hiPSC-CMs and SKBR3 cells into the microphysiological system and the addition of Herceptin. TA-2 demonstrated downscaled devices (Nanoscribe) with 3D hiPSC-CMs in collagen hydrogels can be used in bioreactor studies for microgravity studies and the samples can endure the fluid flow stresses within the bioreactor vessel. These studies contribute to the development of 3D *in vitro* models to closely study cellular processes and mechanisms of cardiovascular diseases.

6.2 FUTURE DIRECTIONS

This project can be continued in several avenues, each to advance the field of cardiovascular tissue engineering and preclinical drug screening. These directions will not only highlight the application of microfluidic devices in molecular and cellular studies but set the foundation for translational medicine and drug screening.

The first route explores the implementation of hiPSC-CMs and patient-derived xenograft (PDX) cells within the capillary-circuit device. Building upon previous studies, it is important to use patient-derived cells to more accurately study cell behavior and its translation into *in vivo* and clinical trials.¹⁰⁸ Specifically, cardiovascular and cancer tissue models can be developed to study cardiotoxicity of several cancer treatment drugs, including Doxorubicin and Herceptin. Drug studies can be conducted with the capillary-circuit device and functional outputs can include IC₅₀ values, gene expression studies, and functional studies of hiPSC-CMs including beat rate and calcium handling.

An additional avenue includes studying the combination of radiation and microgravity on hiPSC-CMs. It is not well known how both radiation and microgravity during spaceflight and time on the International Space Station (ISS) affects hiPSC-CMs. Combining the bioreactor simulated microgravity and radiation exposure, could serve as a foundational system to study the effects closely and identify potential preventative methods, including nanoparticle treatment.

In conclusion, these approaches not only demonstrate the potential uses of the capillary-circuit device, but also highlight its potential to build platforms to study specific cardiovascular diseases. From the design and development of the capillary-circuit device to multiple 3D cell experiments, this project has the potential to propel tissue engineering and preclinical drug screening forward.

References

1. Cardiovascular diseases (CVDs). Accessed April 26, 2024. [https://www.who.int/news-room/fact-sheets/detail/cardiovascular-diseases-\(cvds\)](https://www.who.int/news-room/fact-sheets/detail/cardiovascular-diseases-(cvds))
2. Flora GD, Nayak MK. A Brief Review of Cardiovascular Diseases, Associated Risk Factors and Current Treatment Regimes. *Curr Pharm Des.* 2019;25(38):4063-4084. doi:10.2174/1381612825666190925163827
3. Bhutani P, Joshi G, Raja N, et al. U.S. FDA Approved Drugs from 2015-June 2020: A Perspective. *J Med Chem.* 2021;64(5):2339-2381. doi:10.1021/ACS.JMEDCHEM.0C01786/SUPPL_FILE/JM0C01786_SI_001.PDF
4. Investigational New Drugs: FDA Has Taken Steps to Improve the Expanded Access Program but Should Further Clarify How Adverse Events Data Are Used | U.S. GAO. Accessed April 26, 2024. <https://www.gao.gov/products/gao-17-564>
5. Step 1: Discovery and Development | FDA. Accessed April 26, 2024. <https://www.fda.gov/patients/drug-development-process/step-1-discovery-and-development>
6. Step 2: Preclinical Research | FDA. Accessed April 26, 2024. <https://www.fda.gov/patients/drug-development-process/step-2-preclinical-research>
7. Step 3: Clinical Research | FDA. Accessed April 26, 2024. <https://www.fda.gov/patients/drug-development-process/step-3-clinical-research>
8. Sun D, Gao W, Hu H, Zhou S. Why 90% of clinical drug development fails and how to improve it? *Acta Pharm Sin B.* 2022;12(7):3049-3062. doi:10.1016/J.APSB.2022.02.002
9. Parasrampur DA, Benet LZ, Sharma A. Why Drugs Fail in Late Stages of Development: Case Study Analyses from the Last Decade and Recommendations. *AAPS Journal.* 2018;20(3):1-16. doi:10.1208/S12248-018-0204-Y/TABLES/1
10. Ribas J, Sadeghi H, Manbachi A, et al. Cardiovascular Organ-on-a-Chip Platforms for Drug Discovery and Development. *Appl In Vitro Toxicol.* 2016;2(2):82. doi:10.1089/AIVT.2016.0002
11. Janssen PML, Lehnart SE, Prestle J Jürgen, Hasenfuss G. Preservation of contractile characteristics of human myocardium in multi-day cell culture. *J Mol Cell Cardiol.* 1999;31(8):1419-1427. doi:10.1006/jmcc.1999.0978
12. Ronaldson-Bouchard K, Vunjak-Novakovic G. Organs-on-a-Chip: A Fast Track for Engineered Human Tissues in Drug Development. *Cell Stem Cell.* 2018;22(3):310-324. doi:10.1016/J.STEM.2018.02.011
13. Gimbrone MA, García-Cardeña G. Endothelial Cell Dysfunction and the Pathobiology of Atherosclerosis. *Circ Res.* 2016;118(4):620-636. doi:10.1161/CIRCRESAHA.115.306301
14. Chunduri V, Maddi S. Role of in vitro two-dimensional (2D) and three-dimensional (3D) cell culture systems for ADME-Tox screening in drug discovery and development: a comprehensive review. *ADMET DMPK.* 2023;11(1):1. doi:10.5599/ADMET.1513
15. Loewa A, Feng JJ, Hedtrich S. Human disease models in drug development. *Nature Reviews Bioengineering 2023 1:8.* 2023;1(8):545-559. doi:10.1038/s44222-023-00063-3
16. Lalit PA, Hei DJ, Raval AN, Kamp TJ. iPS Cells for Post-myocardial Infarction Repair: Remarkable Opportunities and Challenges. *Circ Res.* 2014;114(8):1328. doi:10.1161/CIRCRESAHA.114.300556
17. Sanz-Nogués C, O'Brien T. In vitro models for assessing therapeutic angiogenesis. *Drug Discov Today.* 2016;21(9):1495-1503. doi:10.1016/J.DRUDIS.2016.05.016
18. Mak IWY, Evaniew N, Ghert M. Lost in translation: animal models and clinical trials in cancer treatment. *Am J Transl Res.* 2014;6(2):114. Accessed April 26, 2024. [/pmc/articles/PMC3902221/](https://pubmed.ncbi.nlm.nih.gov/articles/PMC3902221/)

19. Sacchetto C, Vitiello L, de Windt LJ, Rampazzo A, Calore M. Modeling Cardiovascular Diseases with hiPSC-Derived Cardiomyocytes in 2D and 3D Cultures. *International Journal of Molecular Sciences* 2020, Vol 21, Page 3404. 2020;21(9):3404. doi:10.3390/IJMS21093404
20. Zhu K, Bao X, Wang Y, Lu T, Zhang L. Human induced pluripotent stem cell (hiPSC)-derived cardiomyocyte modelling of cardiovascular diseases for natural compound discovery. *Biomedicine & Pharmacotherapy*. 2023;157:113970. doi:10.1016/J.BIOPHA.2022.113970
21. Esparza A, Jimenez N, Borrego EA, Browne S, Natividad-Diaz SL. Review: Human stem cell-based 3D in vitro angiogenesis models for preclinical drug screening applications. *Mol Biol Rep*. 2024;51(1):1-19. doi:10.1007/S11033-023-09048-2/METRICS
22. Niculescu AG, Chircov C, Bîrcă AC, Grumezescu AM. Fabrication and Applications of Microfluidic Devices: A Review. *International Journal of Molecular Sciences* 2021, Vol 22, Page 2011. 2021;22(4):2011. doi:10.3390/IJMS22042011
23. Olanrewaju AO, Robillard A, Dagher M, Juncker D. Autonomous microfluidic capillarie circuits replicated from 3D-printed molds. *Lab Chip*. 2016;16(19):3804-3814. doi:10.1039/C6LC00764C
24. Sun J, Warden AR, Ding X. Recent advances in microfluidics for drug screening. *Biomicrofluidics*. 2019;13(6):61503. doi:10.1063/1.5121200
25. Veldhuizen J, Cutts J, Brafman DA, Migrino RQ, Nikkhah M. Engineering anisotropic human stem cell-derived three-dimensional cardiac tissue on-a-chip. *Biomaterials*. 2020;256. doi:10.1016/J.BIOMATERIALS.2020.120195
26. Nsair A, MacLellan WR. Induced pluripotent stem cells for regenerative cardiovascular therapies and biomedical discovery. *Adv Drug Deliv Rev*. 2011;63(4-5):324-330. doi:10.1016/J.ADDR.2011.01.013
27. Morin KT, Tranquillo RT. In Vitro Models of Angiogenesis and Vasculogenesis in Fibrin Gel. *Exp Cell Res*. 2013;319(16):2409. doi:10.1016/J.YEXCR.2013.06.006
28. Prestwich GD, Healy KE. Why regenerative medicine needs an extracellular matrix. *Expert Opin Biol Ther*. 2015;15(1):3-7. doi:10.1517/14712598.2015.975200
29. Briquez PS, Clegg LE, Martino MM, Gabhann F Mac, Hubbell JA. Design principles for therapeutic angiogenic materials. *Nature Reviews Materials* 2016 1:1. 2016;1(1):1-15. doi:10.1038/natrevmats.2015.6
30. Wang C, Koo S, Park M, et al. Maladaptive Contractility of 3D Human Cardiac Microtissues to Mechanical Nonuniformity. *Adv Healthc Mater*. 2020;9(8). doi:10.1002/ADHM.201901373
31. Olanrewaju A, Beaugrand M, Yafia M, Juncker D. Capillary microfluidics in microchannels: from microfluidic networks to capillarie circuits. *Lab Chip*. 2018;18(16):2323-2347. doi:10.1039/C8LC00458G
32. Kitani T, Ong SG, Lam CK, et al. Human-Induced Pluripotent Stem Cell Model of Trastuzumab-Induced Cardiac Dysfunction in Patients with Breast Cancer. *Circulation*. 2019;139(21):2451-2465. doi:10.1161/CIRCULATIONAHA.118.037357/SUPPL_FILE/COTR139_21.PDF
33. Wnorowski A, Sharma A, Chen H, et al. Effects of Spaceflight on Human Induced Pluripotent Stem Cell-Derived Cardiomyocyte Structure and Function. *Stem Cell Reports*. 2019;13(6):960-969. doi:10.1016/j.stemcr.2019.10.006
34. FastStats - Leading Causes of Death. Accessed May 8, 2024. <https://www.cdc.gov/nchs/fastats/leading-causes-of-death.htm>
35. Treatment for Cancer - NCI. Accessed May 8, 2024. <https://www.cancer.gov/about-cancer/treatment>

36. Chemotherapy Side Effects | American Cancer Society. Accessed May 8, 2024. <https://www.cancer.org/cancer/managing-cancer/treatment-types/chemotherapy/chemotherapy-side-effects.html>
37. Choksey A, Timm KN. Cancer Therapy-Induced Cardiotoxicity—A Metabolic Perspective on Pathogenesis, Diagnosis and Therapy. *Int J Mol Sci.* 2022;23(1):441. doi:10.3390/IJMS23010441
38. Echocardiogram (Echo) | American Heart Association. Accessed May 8, 2024. <https://www.heart.org/en/health-topics/heart-attack/diagnosing-a-heart-attack/echocardiogram-echo>
39. The Human Body in Space - NASA. Accessed June 29, 2024. <https://www.nasa.gov/humans-in-space/the-human-body-in-space/>
40. Connor MK, Hood DA. Effect of microgravity on the expression of mitochondrial enzymes in rat cardiac and skeletal muscles. *J Appl Physiol (1985).* 1998;84(2):593-598. doi:10.1152/JAPPL.1998.84.2.593
41. Vashi A, Sreejith KR, Nguyen NT. Lab-on-a-Chip Technologies for Microgravity Simulation and Space Applications. *Micromachines 2023, Vol 14, Page 116.* 2022;14(1):116. doi:10.3390/MI14010116
42. Mozneb M, Jenkins A, Sances S, et al. Multi-lineage heart-chip models drug cardiotoxicity and enhances maturation of human stem cell-derived cardiovascular cells. *Lab Chip.* 2024;24(4):869-881. doi:10.1039/D3LC00745F
43. Esparza A, Jimenez N, Joddar B, Natividad-Diaz S. Development of in vitro cardiovascular tissue models within capillary circuit microfluidic devices fabricated with 3D stereolithography printing. *SN Appl Sci.* 2023;5(9):1-15. doi:10.1007/S42452-023-05459-9/FIGURES/7
44. Wang C, Koo S, Park M, et al. Maladaptive Contractility of 3D Human Cardiac Microtissues to Mechanical Nonuniformity. *Adv Healthc Mater.* 2020;9(8):e1901373. doi:10.1002/ADHM.201901373
45. Ronaldson-Bouchard K, Vunjak-Novakovic G. Organs-on-a-Chip: A Fast Track for Engineered Human Tissues in Drug Development. *Cell Stem Cell.* 2018;22(3):310-324. doi:10.1016/J.STEM.2018.02.011
46. Walsh CL, Babin BM, Kasinskas RW, Foster JA, McGarry MJ, Forbes NS. A multipurpose microfluidic device designed to mimic microenvironment gradients and develop targeted cancer therapeutics. *Lab Chip.* 2009;9(4):545-554. doi:10.1039/B810571E
47. Sebastian B, Dittrich PS. Microfluidics to Mimic Blood Flow in Health and Disease. *Annu Rev Fluid Mech.* 2018;50(Volume 50, 2018):483-504. doi:10.1146/ANNUREV-FLUID-010816-060246/CITE/REFWORKS
48. Mehta V, Rath SN. 3D printed microfluidic devices: a review focused on four fundamental manufacturing approaches and implications on the field of healthcare. *Bio-Design and Manufacturing 2021 4:2.* 2021;4(2):311-343. doi:10.1007/S42242-020-00112-5
49. Scott SM, Ali Z. Fabrication Methods for Microfluidic Devices: An Overview. *Micromachines (Basel).* 2021;12(3). doi:10.3390/MI12030319
50. Stereolithography: SLA 3D Printing Simply Explained | All3DP. Accessed May 8, 2024. <https://all3dp.com/2/stereolithography-3d-printing-simply-explained/>
51. Carnero B, Bao-Varela C, Gómez-Varela AI, Álvarez E, Flores-Arias MT. Microfluidic devices manufacturing with a stereolithographic printer for biological applications. *Materials Science and Engineering: C.* 2021;129:112388. doi:10.1016/J.MSEC.2021.112388

52. SLA Printing | Why SLA Is the Popular Choice for Business | Blog. Accessed May 8, 2024. <https://www.3dmitech.co.uk/post/sla-printing>
53. Photonic Professional GT2: Scientific microfabrication 3D printer. Accessed June 29, 2024. <https://www.nanoscribe.com/en/products/photonic-professional-gt2/>
54. Nanoscribe Photonic Professional GT+ | Terrapin Works. Accessed June 29, 2024. <https://terrapinworks.umd.edu/equipment/nanoscribe-photonic-professional-gt>
55. Carlborg CF, Moraga F, Saharil F, Van Der Wijngaart W, Haraldsson T. RAPID PERMANENT HYDROPHILIC AND HYDROPHOBIC PATTERNING OF POLYMER SURFACES VIA OFF-STOICHIOMETRY THIOL-ENE (OSTE) PHOTOGRAFTING.
56. Setting up and using the Finish Kit (Form 2). Accessed May 8, 2024. https://support.formlabs.com/s/article/Form-2-Finish-Kit-Setup?language=en_US
57. Photoresins specifically for Two-Photon Polymerization. Accessed May 9, 2024. <https://www.nanoscribe.com/en/products/ip-photoresins/>
58. Operational Workflow – NanoGuide. Accessed May 9, 2024. <https://support.nanoscribe.com/hc/en-gb/articles/360002722273-Operational-Workflow>
59. BIG > OrientationJ. Accessed December 5, 2022. <http://bigwww.epfl.ch/demo/orientation/>
60. Photoresins specifically for Two-Photon Polymerization. Accessed June 2, 2024. <https://www.nanoscribe.com/en/products/ip-photoresins/>
61. Norman M, Herin P, Fagrell B, Zetterström R. Capillary Blood Cell Velocity in Full-Term Infants as Determined in Skin by Videophotometric Microscopy. *Pediatric Research* 1988 23:6. 1988;23(6):585-588. doi:10.1203/00006450-198806000-00011
62. Ansys Fluent – Basics Learning Track | Ansys Innovation Course. Accessed May 12, 2024. <https://courses.ansys.com/index.php/learning-track/getting-started-with-ansys-fluent-basics/>
63. SYLGARD™ 184 Silicone Elastomer Kit | Dow Inc. Accessed May 11, 2024. <https://www.dow.com/en-us/pdp/sylgard-184-silicone-elastomer-kit.01064291z.html#overview>
64. OSTEMER 322 Crystal Clear | OSTEMERS. Accessed May 9, 2024. <https://www.ostemers.com/products/ostemer-crystal-clear/>
65. Stark BL, Gamboa M, Esparza A, et al. Materials Characterization of Stereolithography 3D Printed Polymer to Develop a Self-Driven Microfluidic Device for Bioanalytical Applications. *ACS Appl Bio Mater*. Published online 2024. doi:10.1021/ACSABM.4C00059/ASSET/IMAGES/LARGE/MT4C00059_0008.JPEG
66. Nielsen JB, Hanson RL, Almughamsi HM, Pang C, Fish TR, Woolley AT. Microfluidics: Innovations in Materials and Their Fabrication and Functionalization. *Anal Chem*. 2020;92(1):150. doi:10.1021/ACS.ANALCHEM.9B04986
67. Venzac B, Deng S, Mahmoud Z, et al. PDMS Curing Inhibition on 3D-Printed Molds: Why? Also, How to Avoid It? *Anal Chem*. 2021;93(19):7180-7187. doi:10.1021/ACS.ANALCHEM.0C04944/ASSET/IMAGES/LARGE/AC0C04944_0006.JPEG
68. Friend J, Yeo L. Fabrication of microfluidic devices using polydimethylsiloxane. *Biomicrofluidics*. 2010;4(2). doi:10.1063/1.3259624/385729
69. 5 techniques to make PDMS microfluidics - SimpleMicrofluidics. Accessed June 29, 2024. <https://simplemicrofluidics.com/diy-microfluidics-prototyping/pdms-molded-microfluidics/>
70. FastStats - Leading Causes of Death. Accessed July 2, 2024. <https://www.cdc.gov/nchs/fastats/leading-causes-of-death.htm>
71. Li Z, Zheng W, Wang H, et al. Application of Animal Models in Cancer Research: Recent Progress and Future Prospects. *Cancer Manag Res*. 2021;13:2455. doi:10.2147/CMAR.S302565

72. Mak IWY, Evaniew N, Ghert M. Lost in translation: animal models and clinical trials in cancer treatment. *Am J Transl Res*. 2014;6(2):114. Accessed May 8, 2024. /pmc/articles/PMC3902221/
73. Chung AS, Ferrara N. Developmental and pathological angiogenesis. *Annu Rev Cell Dev Biol*. 2011;27:563-584. doi:10.1146/ANNUREV-CELLBIO-092910-154002
74. Kusuma S, Shen YI, Hanjaya-Putra D, Mali P, Cheng L, Gerecht S. Self-organized vascular networks from human pluripotent stem cells in a synthetic matrix. *Proc Natl Acad Sci U S A*. 2013;110(31):12601-12606. doi:10.1073/PNAS.1306562110
75. Coulombe KLK, Bajpai VK, Andreadis ST, Murry CE. Heart regeneration with engineered myocardial tissue. *Annu Rev Biomed Eng*. 2014;16(Volume 16, 2014):1-28. doi:10.1146/ANNUREV-BIOENG-071812-152344/CITE/REFWORKS
76. Wilson HK, Canfield SG, Shusta E V., Palecek SP. Concise Review: Tissue-Specific Microvascular Endothelial Cells Derived from Human Pluripotent Stem Cells. *Stem Cells*. 2014;32(12):3037. doi:10.1002/STEM.1797
77. Yoder MC. Differentiation of pluripotent stem cells into endothelial cells. *Curr Opin Hematol*. 2015;22(3):252. doi:10.1097/MOH.000000000000140
78. Natividad-Diaz SL, Browne S, Jha AK, et al. A combined hiPSC-derived endothelial cell and in vitro microfluidic platform for assessing biomaterial-based angiogenesis. *Biomaterials*. 2019;194:73. doi:10.1016/J.BIOMATERIALS.2018.11.032
79. Weng KC, Kurokawa YK, Hajek BS, Paladin JA, Shirure VS, George SC. Human Induced Pluripotent Stem-Cardiac-Endothelial-Tumor-on-a-Chip to Assess Anticancer Efficacy and Cardiotoxicity. <https://home.liebertpub.com/tec>. 2020;26(1):44-55. doi:10.1089/TEN.TEC.2019.0248
80. Lee J, Mehrotra S, Zare-Eelanjegh E, et al. A Heart-Breast Cancer-on-a-Chip Platform for Disease Modeling and Monitoring of Cardiotoxicity Induced by Cancer Chemotherapy. *Small*. 2021;17(15):2004258. doi:10.1002/SMLL.202004258
81. Walsh CL, Babin BM, Kasinskas RW, Foster JA, McGarry MJ, Forbes NS. A multipurpose microfluidic device designed to mimic microenvironment gradients and develop targeted cancer therapeutics. *Lab Chip*. 2009;9(4):545. doi:10.1039/B810571E
82. Joddar B, Natividad-Diaz SL, Padilla AE, et al. Engineering approaches for cardiac organoid formation and their characterization. *Transl Res*. 2022;250:46-67. doi:10.1016/J.TRSL.2022.08.009
83. Moreno-Rivas O, Hernández-Velázquez D, Piazza V, Marquez S. Rapid prototyping of microfluidic devices by SL 3D printing and their biocompatibility study for cell culturing. *Mater Today Proc*. 2019;13:436-445. doi:10.1016/J.MATPR.2019.03.189
84. Kurokawa YK, Yin RT, Shang MR, Shirure VS, Moya ML, George SC. Human Induced Pluripotent Stem Cell-Derived Endothelial Cells for Three-Dimensional Microphysiological Systems. <https://home.liebertpub.com/tec>. 2017;23(8):474-484. doi:10.1089/TEN.TEC.2017.0133
85. Luu AZ, Chowdhury B, Al-Omran M, Teoh H, Hess DA, Verma S. Role of Endothelium in Doxorubicin-Induced Cardiomyopathy. *JACC Basic Transl Sci*. 2018;3(6):861. doi:10.1016/J.JACBTS.2018.06.005
86. Chevalier F, Lavergne M, Negroni E, et al. Glycosaminoglycan mimetic improves enrichment and cell functions of human endothelial progenitor cell colonies. *Stem Cell Res*. 2014;12(3):703-715. doi:10.1016/J.SCR.2014.03.001

87. Carpentier G, Berndt S, Ferratge S, et al. Angiogenesis Analyzer for ImageJ — A comparative morphometric analysis of “Endothelial Tube Formation Assay” and “Fibrin Bead Assay.” *Scientific Reports* 2020 10:1. 2020;10(1):1-13. doi:10.1038/s41598-020-67289-8
88. P-Value in Statistical Hypothesis Tests: What is it? - Statistics How To. Accessed July 4, 2024. <https://www.statisticshowto.com/probability-and-statistics/statistics-definitions/p-value/>
89. Auchampach J, Han L, Huang GN, et al. Measuring cardiomyocyte cell-cycle activity and proliferation in the age of heart regeneration. *Am J Physiol Heart Circ Physiol*. 2022;322(4):H579-H596. doi:10.1152/AJPHEART.00666.2021/ASSET/IMAGES/LARGE/AJPHEART.00666.2021_F003.JPG
90. Droste P, Wong DWL, Hohl M, von Stillfried S, Klinkhammer BM, Boor P. Semiautomated pipeline for quantitative analysis of heart histopathology. *J Transl Med*. 2023;21(1):1-13. doi:10.1186/S12967-023-04544-2/FIGURES/6
91. Fluoro-Max Dyed Green Aqueous Fluorescent Particles. Accessed July 4, 2024. <https://www.thermofisher.com/order/catalog/product/G0100>
92. Cao L, Der Meer ADV, Verbeek FJ, Passier R. Automated image analysis system for studying cardiotoxicity in human pluripotent stem cell-Derived cardiomyocytes. *BMC Bioinformatics*. 2020;21(1):1-12. doi:10.1186/S12859-020-3466-1/FIGURES/4
93. How Your Cardiovascular System Works. Accessed July 4, 2024. <https://my.clevelandclinic.org/health/body/21833-cardiovascular-system>
94. Introduction to the Cardiovascular System | SEER Training. Accessed July 6, 2024. <https://training.seer.cancer.gov/anatomy/cardiovascular/>
95. Cancer. Accessed July 6, 2024. <https://www.who.int/news-room/fact-sheets/detail/cancer>
96. Cancer treatment - Mayo Clinic. Accessed July 6, 2024. <https://www.mayoclinic.org/tests-procedures/cancer-treatment/about/pac-20393344>
97. Breast Cancer Statistics | How Common Is Breast Cancer? | American Cancer Society. Accessed July 6, 2024. <https://www.cancer.org/cancer/types/breast-cancer/about/how-common-is-breast-cancer.html>
98. Valiyaveetil D, Joseph D, Malik M. Cardiotoxicity in breast cancer treatment: Causes and mitigation. *Cancer Treat Res Commun*. 2023;37:100760. doi:10.1016/J.CTARC.2023.100760
99. Montisci A, Palmieri V, Liu JE, et al. Severe cardiac toxicity induced by cancer therapies requiring intensive care unit admission. *Front Cardiovasc Med*. 2021;8. doi:10.3389/FCVM.2021.713694/FULL
100. Weng KC, Kurokawa YK, Hajek BS, Paladin JA, Shirure VS, George SC. Human Induced Pluripotent Stem-Cardiac-Endothelial-Tumor-on-a-Chip to Assess Anticancer Efficacy and Cardiotoxicity. <https://home.liebertpub.com/tec>. 2020;26(1):44-55. doi:10.1089/TEN.TEC.2019.0248
101. How the Human Body Changes in Space | BCM. Accessed July 6, 2024. <https://www.bcm.edu/academic-centers/space-medicine/translational-research-institute/space-health-resources/how-the-body-changes-in-space>
102. Kuang S, Singh NM, Wu Y, et al. Role of microfluidics in accelerating new space missions. *Biomicrofluidics*. 2022;16(2):21503. doi:10.1063/5.0079819
103. Lian X, Bao X, Al-Ahmad A, et al. Efficient differentiation of human pluripotent stem cells to endothelial progenitors via small-molecule activation of WNT signaling. *Stem Cell Reports*. 2014;3(5):804-816. doi:10.1016/J.STEMCR.2014.09.005

104. Lian X, Zhang J, Azarin SM, et al. Directed cardiomyocyte differentiation from human pluripotent stem cells by modulating Wnt/ β -catenin signaling under fully defined conditions. *Nature Protocols* 2013 8:1. 2012;8(1):162-175. doi:10.1038/nprot.2012.150
105. MTrackJ. Accessed July 4, 2024. <https://image.science.org/meijering/software/mtrackj/>
106. Jha AK, Tharp KM, Ye J, et al. Enhanced survival and engraftment of transplanted stem cells using growth factor sequestering hydrogels. *Biomaterials*. 2015;47:1-12. doi:10.1016/J.BIOMATERIALS.2014.12.043
107. Huebsch N, Loskill P, Mandegar MA, et al. Automated Video-Based Analysis of Contractility and Calcium Flux in Human-Induced Pluripotent Stem Cell-Derived Cardiomyocytes Cultured over Different Spatial Scales. *Tissue Eng Part C Methods*. 2015;21(5):467-479. doi:10.1089/TEN.TEC.2014.0283
108. Paik DT, Chandy M, Wu JC. Patient and Disease-Specific Induced Pluripotent Stem Cells for Discovery of Personalized Cardiovascular Drugs and Therapeutics. *Pharmacol Rev*. 2020;72(1):320-342. doi:10.1124/PR.116.013003

Vita

Aibhlin A. Esparza (she/her/hers) was born in El Paso, Texas (TX) to Celia Lopez and David Esparza. She completed her high school education at El Dorado High School in El Paso, TX. After high school, she decided to pursue an engineering degree to gain skills that would improve and advance the creation of models to study cardiovascular (i.e: strokes) or neurological diseases (i.e. Cerebral Palsy), both of which affect her family heavily. She finished her Bachelor of Science (BS) degree in Mechanical Engineering with a minor in Biomedical Engineering in May 2020 from the University of Texas at El Paso, where she worked on several projects ranging from prosthetics to fruit fly studies to study neurological diseases.

Following this, she decided to start pursuing her Ph.D. in Biomedical Engineering in August 2020. During this time, she worked as a graduate research assistant, mentored undergraduate and graduate students, and authored several first and second author research manuscripts.

Through her higher education, she found a passion for teaching science, technology, engineering, and mathematics (STEM) to students of all ages and combining science and engineering principles for the betterment of tools that can be used to address biomedical problems in biology and health care applications. She hopes to continue contributing to science and engineering through her dedication and hard work.

Contact Information: aibhlin.esparza@gmail.com